A NUMERICAL STUDY OF THE NONLINEAR EXPANSION OF A MAGNETO-PLASMA SPHERE

by

Norton Rimer

A dissertation submitted to the Graduate Faculty in Engineering in partial fulfillment of the requirements for the degree of Doctor of Philosophy, The City University of New York.

1972

This manuscript has been read and accepted for the Graduate Faculty in Engineering in satisfaction of the dissertation requirement for the degree of Doctor of Philosophy.

April 6, 1972
date

Chairman of Examining Committee

April 6, 1972
date

Jacques E. Bouvaniste
Executive Officer

Prof. S. M. Chen

Prof. R. Dressler

Prof. W. Rand

Prof. N. C. Jen, Chairman
Supervisory Committee

The City University of New York

ABSTRACT

The expansion of a highly heated plasma sphere into an ambient magnetohydrodynamic medium containing a uniform magnetic field is studied. The expanding plasma compresses the medium in front of it, creating a shock wave which is distorted into an elliptic shape by the magnetic field.

A two-dimensional MHD computer code is developed to study this problem. It is assumed that the expansion is governed by the nondissipative MHD equations which are written in Lagrangian coordinates. Since some dissipation is necessary to obtain the correct solution across the shock waves, the artificial viscosity method of von Neumann and Richtmeyer, developed for gasdynamics, is extended to the MHD problem. The computer code provides rezoning to restore the Lagrangian mesh, distorted by the plasma motion, to a regular shape.

Two mathematical models of the plasma expansion are studied, the spherical piston model; an infinitely conducting, rigid spherical piston expanding at a constant speed, and the blast wave model; a sphere of plasma initially at a uniform pressure and internal energy several orders of magnitude higher than that of the ambient medium. A comparison of the results obtained using the two models is made. These results are also compared with solutions to simplified models in planar geometry.

ACKNOWLEDGEMENTS

First and foremost, I would like to thank my mentor, Professor Norman C. Jen, who suggested the area of research and skillfully directed it from its inception. I would also like to thank the members of my Doctoral Committee, Professors S. M. Chen, R. Dressler, and W. Rand for their interest and advice. The constructive suggestions of Professors C. Costantino and F. Cap (University of Innsbruck) are greatly appreciated.

Thanks are also due to the United States Naval Ordnance Laboratory, in particular D. Lehto and M. Lutzky, for their help with the computer programs.

The financial aid and services provided by The City College and the Department of Civil Engineering are gratefully acknowledged. I would also like to thank the United States Air Force Office of Scientific Research and the National Science Foundation for their financial support.

TABLE OF CONTENTS

LIST OF TABLES

LIST OF FIGURES

NOMENCLATURE

A	area of zone in CYCLONE
a	sound speed
a_o	ambient sound speed
$\bar{a}$	coefficient of artificial viscosity
$\vec{B}$	magnetic field
B_o	magnitude of ambient magnetic field
$\vec{b}$	Alfven speed
b_o	magnitude of ambient Alfven speed
c_f	fast wave speed
c_s	slow wave speed
c^*	magnetosonic speed
E	specific internal energy
f	density ratio at shock
f_m	magnetic field ratio at shock
g	magnetic field jump across shock
h	Lagrangian coordinate
J_o	Jacobian of transformation
K	Lagrangian coordinate
L	Lagrangian coordinate
M	mass of zone
$\overline{M}$	mass attached to a mesh point

n	cycle number
PQ	pressure plus viscous stress term
p	pressure
p_m	magnetic pressure
Q	viscous stress term
R	Eulerian cylindrical coordinate
r	Eulerian spherical coordinate
r_L	ion larmor radius
s_o	square of ratio of sound speed to Alfven speed
T	temperature
t	time
U	shock speed
$\vec{u}$	velocity relative to shock
V	specific volume
$\forall$	volume of zone
$\vec{v}$	velocity vector
x	Eulerian cartesian coordinate
y	Eulerian cartesian coordinate
z	Eulerian cylindrical coordinate
γ	ratio of specific heats
ϵ	expansion parameter
θ	spherical coordinate (azimuth)
$\overline{\theta}$	angle between magnetic field and normal to shock

λ	mean free path
λ_D	Debye length
ρ	density
ϕ	spherical coordinate
∇	gradient operator

CHAPTER 1

INTRODUCTION AND REVIEW

Since the governing differential equations are highly nonlinear, a theoretical analysis of nonlinear magnetohydrodynamic waves becomes rather difficult except in certain special cases involving simple geometries or in cases in which mathematical simplifications may be made. In recent years, numerical methods for solving the nondissipative gasdynamic equations in Lagrangian coordinates have been developed for time dependent problems involving one space coordinate[1-5]. These methods are at present being extended to problems involving two space coordinates[6]. The primary aim of this study is the development of a numerical method for all nonlinear nondissipative problems in a compressible magnetohydrodynamic medium governed by one or two space coordinates.

There are fundamental differences between the existing numerical methods for gasdynamics and the method attempted here. First, since more than one wave speed is possible in magnetohydrodynamics[7], and therefore the number and position of discontinuities is not always predictable, the numerical method must allow for the handling of these discontinuities without resorting to special boundary conditions across them. Second, in problems involving two space coordinates, the shapes of the Lagrangian mesh elements can be radically distorted after only a

short time interval of computation. This distortion, much more prevalent in MHD problems, can result in significant errors[8,9] and make it impossible to carry on the calculation to meaningful time intervals. Therefore the numerical method attempted here will go further than the existing methods and include the restoration of the Lagrangian zones so that the calculation can proceed without errors.

This method will be used to solve two mathematical problems involving nonlinear waves in magnetohydrodynamic media, the spherical piston model and the blast wave model. The first model is a rigid spherical piston which expands at a constant speed into the uniform magnetic field of the medium, while the second is the constant energy expansion of an initially high energy spherical plasma bubble at a nonuniform speed into the same medium. In recent years, the spherical piston problem has been extensively investigated[10-12], but due to the difficulty of this mathematical model, solutions have only been obtained for the special cases of very weak or very strong magnetic field. However, the piston problem has been investigated most thoroughly for planar geometry[13-19] where the mathematics is less involved. The constant energy expansion model without a magnetic field has been studied for many years[20-24], but the effect of the magnetic field has not yet been determined.

In the rest of this chapter, the existing solutions pertaining to these mathematical models will be reviewed briefly along with the theory of magnetohydrodynamic shock waves.

1.1 Planar MHD Shocks and Simple Waves

In order to describe these nonlinear solutions, it is necessary first to discuss the three types of small amplitude waves possible in magnetohydrodynamics. In gasdynamics, the only possible wave speed is the sound speed $a = (\gamma p/\rho)^{\frac{1}{2}}$. In MHD, there is a basic wave speed, present even in an incompressible medium[25], known as the Alfven speed, $\vec{b} = (1/4\pi\rho)^{\frac{1}{2}} \vec{B}$. In a compressible medium, the two basic wave speeds known as magnetoacoustic wave speeds are coupled in a manner given by the Friedrichs diagram, Figure 1.1. These two separate diagrams are for the cases of $b < a$, and $b > a$.

The Friedrichs diagram is a polar plot of the characteristic speeds of the possible small amplitude waves propagating in the $\bar{n}$ direction, (in our case, the x direction), at an angle $\bar{\theta}$ from the direction of the magnetic field. Any normal $\bar{n}$ intersects three curves; the inner curve representing the slow wave with speed c_s, the outer the fast wave with speed c_f, and the middle the Alfven wave with speed b_n.

For $\bar{\theta} = 0^\circ$, that is, in the direction of the applied magnetic field, the sound and Alfven speeds are uncoupled. In Figure 1.1a, the fast wave travels at the sound speed and the slow wave travels at the Alfven speed, while in Figure 1.1b, the reverse is true. Since the effects of the passage of sound and Alfven waves are quite different, the Friedrichs diagram implies that there will be significant changes in the properties of the fast and slow waves as the Alfven speed becomes

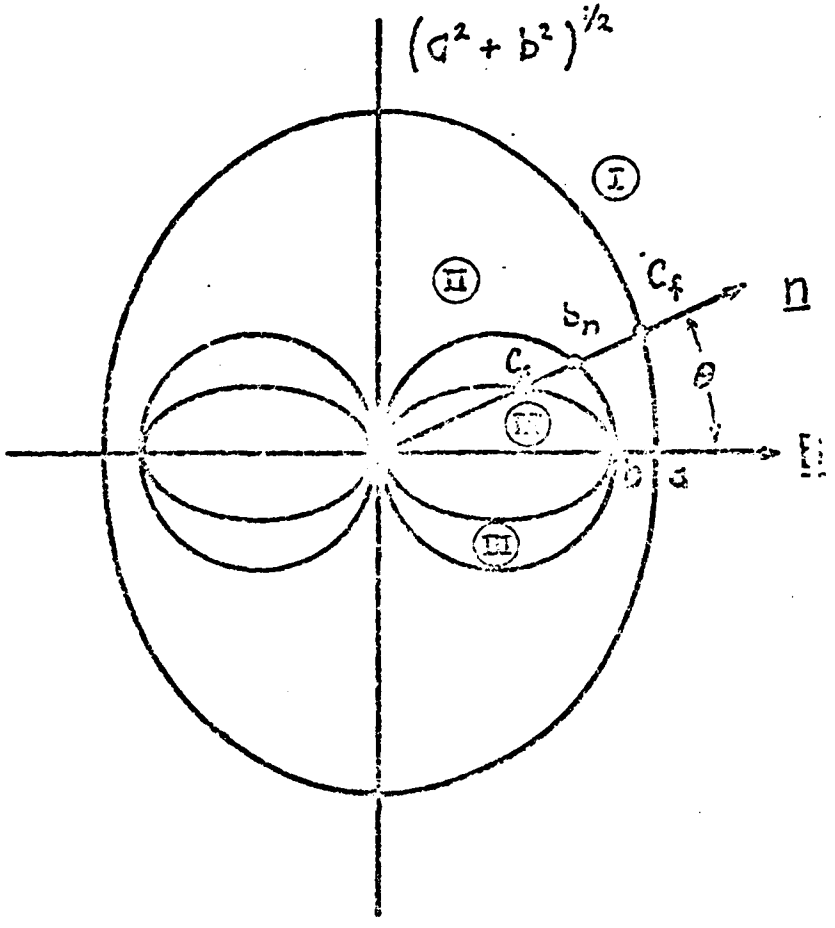

(a) b < a

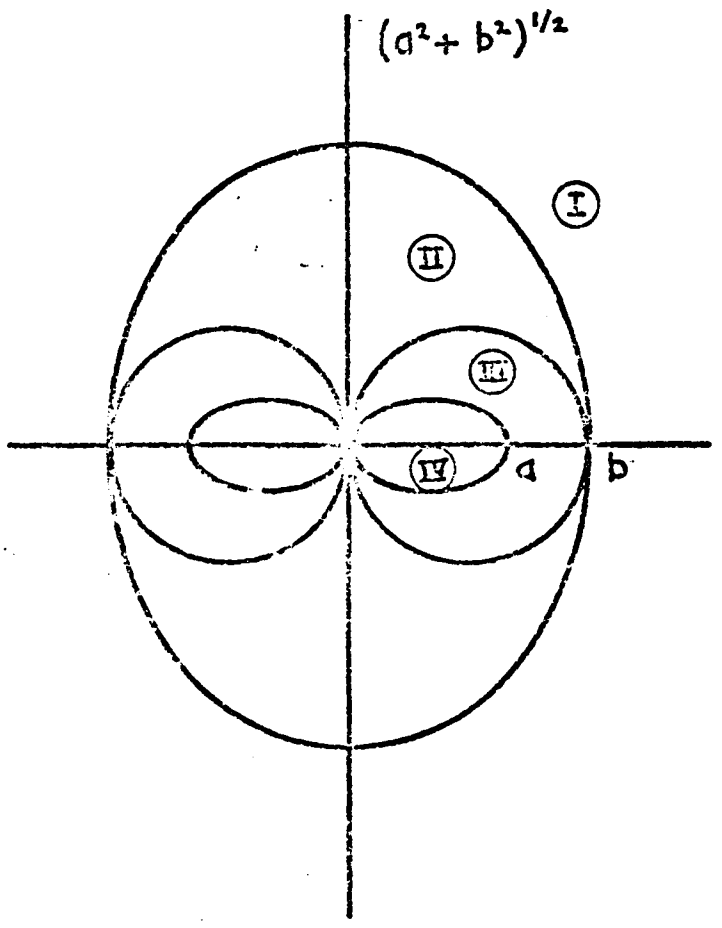

(b) b > a

Fig. 1.1 Friedrichs diagram

greater than the sound speed.

Here the Friedrichs diagram is used to study shock waves. In the diagram each of the numbers I - IV represents a fluid state. The variations in quantities across the discontinuity or shock wave is governed by the generalized Rankine-Hugoniot jump equations[26,27], equations (A1) - (A5) of Appendix A. Solutions to these jump equations were discussed by De Hoffman and Teller[28] and by Friedrichs[7]. The first complete solutions were obtained by Bazer and Ericson[29] who showed that the shock solutions of the generalized Rankine-Hugoniot equations are characterized by transitions from state I ahead of the shock to state II behind the shock, (the fast shock), or from state III to state IV (the slow shock). The fast shock has the similar property to the gasdynamic shock[30] in that the shock velocity is greater than the signal speed ahead of the shock while the velocity is less than the signal speed behind the shock. Also, a simple fast compression wave will steepen into a fast shock[17]. Similar relationships hold for the slow shock.

In addition, another type of solution exists, known as the intermediate or Alfven shock, characterized by a change from state II to state III, without a change of entropy across the shock. However, these intermediate shocks are unstable to small amplitude wave (nonevolutionary) and cannot be formed by the steepening of a compression wave. The intermediate shock should therefore not be considered as a true shock and should not be expected to exist in this calculation.

The fast shock is associated with an increase in the tangential magnetic field in the post shock state and the slow shock with a decrease in the magnetic field. However, the evolutionary condition[17] shows that the tangential magnetic field cannot change sign in the slow shock.

For planar piston problems, the set of hyperbolic partial differential equations becomes reducible since their coefficients are not explicit functions of the independent variable but are only functions of the dependent variables. Certain MHD wave solutions of such a reducible set of equations, known as simple waves, are given by Jeffrey-Taniuti[17]. Simple wave solutions for gasdynamics may be found in Courant-Fredrichs[30].

1.2 The Planar MHD Piston Model

The propagation of shocks due to the motion of a planar piston at a constant speed v_{xp} into an ambient MHD medium containing a magnetic field (B_x, B_y) has been studied in recent years. Solutions have been presented for subsonic piston motions and weak magnetic fields by Akhiezer and Polovin[15] and also by Jeffrey and Taniuti[17]. In addition, Gogosov and Barmin[16] have discussed the solutions for stronger fields and supersonic piston motions.

For the nondissipative one-dimensional problem, the MHD equations can be easily transformed, employing a similarity transformation, into a set of ordinary differential equations in terms of $x' = x/t$. For a constant piston speed, a steady solution is obtained. Therefore all shocks and simple waves travel at constant speeds, and the solutions at any times t_1 and t_2 differ only in a change in position of shock and waves, but not a change in relative position. The waves are centered since the variables involved in the equations are functions of $x' = x/t$ rather than x and t separately.

Other interesting solutions given by Bazer and Ericson[29] are the switch-on shock, the limiting case of a fast shock as the transverse component of the magnetic field ahead of the shock becomes very small, and the switch-off shock, the corresponding limiting case of a slow shock, as B_y vanishes. Later, Chu and Taussig[18] generated these solutions by pushing a piston along the x-axis into an MHD medium

containing a magnetic field with a finite x-component (longitudinal component) and a very small y-component (transverse component). Bazer[13] also has obtained the switch-on shock by pushing the piston at a small angle to the x-axis into a completely longitudinal magnetic field.

1.3 The Spherical Piston Model

The MHD equations in spherical coordinates may be transformed into similarity form by the coordinate transformation $x' = r/t$ thus reducing the number of independent variables to two, x' and θ. As was true for the planar model, this requires that the expansion speed of the spherical piston remain constant and that, initially, the piston be a point in space. A solution has been obtained by Kulsrud et al[11] for small magnetic fields; more exactly, for magnetic fields such that the ambient Alfven speed b_o is much less than the piston speed v_{rp}. In this limit, a numerical solution to the MHD equations in similarity form was obtained by perturbation theory about the Taylor gasdynamic solution[10] using $\epsilon = b_o/v_{rp}$ as the expansion parameter.

Taylor wrote the spherically symmetric gasdynamic equations in similarity form obtaining a set of ordinary differential equations in x'. The boundary conditions at the shock are the Rankine-Hugoniot[26,27] shock equations, while at the piston, the boundary condition is that the fluid velocity is identical to the piston velocity. In slab symmetry the region between the piston and the shock was simply a constant state, but in spherical symmetry, the equations are not reducible[30], so that the variables in this region are not constant. The Taylor solution was therefore a numerical solution.

For the small magnetic field case the boundary conditions at the shock are the MHD shock equations, while at the piston the boundary

conditions specified were that the radial component of fluid velocity was identical to the expansion speed v_{rp} and the magnetic field was tangent to the piston.

The spherical piston problem has also been studied by Bernstein and Kulsrud[12] for very large magnetic fields, that is, for magnetic fields so large that the Alfven speed is much greater than the piston speed ($\epsilon = v_{rp}/b_o << 1$). In this limit, a very weak spherical MHD shock propagates ahead of the piston at approximately the Alfven speed. Over most of this region, the magnetic field is also weakly perturbed from its original uniform value so that the MHD equations in similarity form were linearized by Bernstein and Kulsrud. Near the piston however, the field is perturbed a finite amount and was represented to lowest order by a vacuum field appropriate to a perfectly conducting sphere of radius ϵ given by

$$\vec{B} = B_o \left[e_r \cos\theta \left(1 - \frac{\epsilon^3}{r^3}\right) - e_\theta \sin\theta \left(1 + \frac{\epsilon^3}{2r^3}\right)\right] \qquad (1.1)$$

which satisfies the boundary condition at the piston, $B_{rp} = 0$. An analytical solution to first order for the linearized equations in the region away from the piston was presented and matched to a numerical solution near the piston to give the complete solution.

1.4 The Blast Wave Model

For the case of no magnetic field, this model, involving the constant energy, nonuniform expansion of a plasma sphere, has been extensively studied by Taylor[20] and Sedov[21]. For this case, the expansion is governed by the spherically symmetric gasdynamic equations which cannot be written in similarity form since the expansion speed is not constant. They also assumed that the sphere is a point at which a finite amount of energy is concentrated and suddenly released into the atmosphere. The solutions matched progressing waves numerically to the shock using the strong shock relations, thus limiting the solution to early times when the shock is still very strong.

A numerical solution was obtained by Brode[22] for the blast wave model using the method of artificial viscosity to smooth out the shocks. Brode observed a second shock forming in the tail of a rarefaction wave propagating toward the origin. This secondary shock grew in strength as it also propagated toward the origin. He was able to follow it as it was reflected at the origin and as it overtook the main shock wave.

The numerical method of characteristics was applied to the solution of this problem by Chou and Huang[23] using the shock equations across both the main and secondary shocks. They were not able to follow the second shock after it imploded on the origin; therefore their solution is limited to early times compared to the Brode solution. The flow field

obtained differed greatly from the Sedov solution except in the peak pressure of the blast which is always located at the main shock.

From the analysis of many fireballs having different initial conditions (radius, pressure, etc.), Chou and Huang determined that spherical blasts have the same peak pressure distribution at large values of time if the initial total energy of the high energy sphere is the same. If, in addition, the total mass in the sphere is also kept constant, the positions of the main and secondary shocks are also the same for large times. This implies that the results for one set of initial conditions give significant information over a wide range of initial conditions. Of course, by large values of time, they meant times at which the sphere has expanded significantly while the secondary shock has not reached the origin.

Solutions for this model which include the effects of a magnetic field have not as yet been presented.

1.5 Summary

Significant and extensive investigations into the problem of a piston expanding into the magnetic field of a magnetohydrodynamic medium have been made for the planar case. However, due to the mathematical difficulty involved, solutions to this problem in spherical geometry have only been obtained for the special cases of very weak and very strong magnetic fields. For the more difficult model of a constant energy non-uniform expansion (blast wave), solutions have been attained only in the case of zero magnetic field.

The plan of this work is, in Chapter 2, to give a detailed description of the numerical method and to describe the two separate computer programs, MHD WUNDY, specifically designed to solve one-dimensional problems, and MHD CYCLONE, to solve three-dimensional axisymmetric problems. In Chapter 3, new analytical solutions to planar one-dimensional piston problems will be presented and known solutions compared to numerical solutions obtained from MHD WUNDY and MHD CYCLONE. In Chapter 4, numerical solutions to the spherical piston problem will be given for the first time and the solutions for the asymtotic cases compared with existing solutions. Qualitative comparisons will be made with the solutions of Chapter 3 and the effects of rezoning on the results will be discussed. In Chapter 5, numerical solutions to the MHD blast wave model will be presented for the first time both for the planar and the spherical case. A comparison between the piston and blast wave models will be made in Chapter 6 and the conclusions of this dissertation will be summarized.

CHAPTER 2

EQUATIONS AND NUMERICAL METHODS

Here the plasma is considered to be a fully ionized continuum with all the normal characteristics of a fluid. The electrically charged particles give rise to electric currents which interact with the magnetic field. As a consequence, the electromagnetic field creates body forces which act on the fluid. It is assumed that all dissipative processes within the fluid can be neglected, so that the fundamental equations governing its behavior are the ideal magnetohydrodynamic equations. These equations are written in Lagrangian form with an added artificial viscosity. In this chapter, the fundamental equations are given in Eulerian and Lagrangian form, the numerical method is presented, and the computer programs are discussed.

2.1 Fundamental Equations in Eulerian and Lagrangian Coordinates

The nondissipative magnetohydrodynamic (MHD) equations are written in vector form in Eulerian coordinates as follows[25] (c.g.s. gauss units):

Conservation of mass:

$$\frac{D\rho}{Dt} + \rho \nabla \cdot \vec{v} = 0 \tag{2.1}$$

Equation of motion:

$$\rho \frac{D\vec{v}}{Dt} = - \nabla p + \frac{1}{4\pi} (\nabla \times \vec{B}) \times \vec{B} \tag{2.2}$$

Induction equation:

$$\frac{D\vec{B}}{Dt} = (\vec{B} \cdot \nabla) \vec{v} - \vec{B} (\nabla \cdot \vec{v}) \tag{2.3}$$

Energy equation:

$$\frac{DE}{Dt} = \frac{p}{\rho^2} \frac{D\rho}{Dt} \tag{2.4}$$

Equation of state:

$$E = \frac{p}{\rho(\gamma - 1)} \tag{2.5}$$

where ρ = mass density

$\vec{v}$ = particle velocity

p = pressure

B = magnetic induction

E = internal energy/unit mass

γ = ratio of specific heats

The symbol D/Dt represents the material or Lagrangian derivative and gives the rate of change of a quantity along a particle path. It is given by

$$\frac{D}{Dt} = \frac{\partial}{\partial t} + (\vec{v} \cdot \nabla) \qquad (2.6)$$

The MHD equations as given contain the following simplifications[31,32]:

1. The displacement current in Maxwells equation is neglected.
2. Current flow due to charge transport is small.
3. The electrostatic and gravitational body forces are neglected in the equation of motion.
4. The equation of state given is that of an ideal gas.

The numerical calculations here will be based upon the following parameters which approximate atmospheric conditions at an altitude of 200 km above sea level[33]:

density $\rho = 10^{-13}$ gms/cm^3

pressure $p = 3 \times 10^{-4}$ dynes/cm^2

internal energy $E = 4.5 \times 10^{9}$ ergs/gm

ratio of specific heats $\gamma = 5/3$

temperature $T = 660^{\circ}$ K

magnetic field $B = 0.5$ gauss (2.7)

number density $n = 3 \times 10^{9}$ particles/cm^3

mean free path $\lambda = 0.2$ cm

debye sphere $\lambda_D = 2.4 \times 10^{-3}$ cm

ion larmor radius $r_L = 2.1 \times 10^{3}$ cm

Using this data, it was determined that the number of particles in a debye sphere is much greater than one, that the mean free path is much smaller than any length of interest, and that the ion larmor radius is much greater than the mean free path. Since all the above are true[34], it is valid to use the MHD equations to analyze problems in this media.

Equations (2.1) - (2.5) may be expressed in cylindrical coordinates (R, ϕ, z). For our particular problem, if the coordinate system is oriented so that the z axis lies along the direction of the uniform magnetic field which is an axis of symmetry, there is no dependence of the variables described by (2.1) - (2.5) on the ϕ coordinate. Since, initially, the ϕ

components of the vector variables $\vec{v}$ and $\vec{B}$ are zero, these components will be zero for all later times. Equations (2.1) - (2.3), written in axisymmetric cylindrical coordinates, are as follows:

$$\frac{D\rho}{Dt} = -\rho\left(\frac{v_R}{R} + \frac{\partial v_R}{\partial R} + \frac{\partial v_z}{\partial z}\right) \tag{2.8}$$

$$\rho\frac{Dv_R}{Dt} = -\frac{\partial p}{\partial R} + \frac{B_z}{4\pi}\left(\frac{\partial B_R}{\partial z} - \frac{\partial B_z}{\partial R}\right) \tag{2.9}$$

$$\rho\frac{Dv_z}{Dt} = -\frac{\partial p}{\partial z} - \frac{B_R}{4\pi}\left(\frac{\partial B_R}{\partial z} - \frac{\partial B_z}{\partial R}\right) \tag{2.10}$$

$$\frac{DB_R}{Dt} = -\frac{v_R B_R}{R} + B_z\frac{\partial v_R}{\partial z} - B_R\frac{\partial v_z}{\partial z} \tag{2.11}$$

$$\frac{DB_z}{Dt} = -\frac{v_R B_z}{R} + B_R\frac{\partial v_z}{\partial R} - B_z\frac{\partial v_R}{\partial R} \tag{2.12}$$

Equations (2.4) and (2.5) are unchanged.

For use in the numerical method, the MHD equations are transformed into Lagrangian coordinates. Each bit of fluid is given a label K, its Lagrangian coordinate, corresponding to its position in space, x, its Eulerian coordinate, at time t = 0. At time t, this particle of fluid occupies a different position in space but retains the same Lagrangian label. The Eulerian coordinate of the particle is therefore a function of the independent variables K and t. All physical variables are

associated with a particular particle giving the following functional relationship: $F = F(K,t)$, etc.

The MHD equations rewritten in Lagrangian coordinates, will therefore describe how variables associated with a particular particle change with time. Note that the operator D/Dt given by (2.6) is already in Lagrangian form.

Equations (2.8) - (2.12) are transformed in the following manner. Let K and L represent the Lagrangian coordinates. Using the Jacobian transformation relations, replace derivatives with respect to z and R by derivatives with respect to K and L, for example:

$$\frac{\partial F}{\partial R} = \frac{J\left(\frac{F,z}{K,L}\right)}{J_o} \tag{2.13}$$

$$\frac{\partial F}{\partial z} = \frac{J\left(\frac{R,F}{K,L}\right)}{J_o} \tag{2.14}$$

where

$$J_o = J\left(\frac{R,z}{K,L}\right) = \det \begin{vmatrix} \frac{\partial R}{\partial K} & \frac{\partial R}{\partial L} \\ \frac{\partial z}{\partial K} & \frac{\partial z}{\partial L} \end{vmatrix} \tag{2.15}$$

The resulting MHD equations for axisymmetric cylindrical coordinates in Lagrangian form are:

$$\frac{D}{Dt}(\rho J_o R) = 0 \tag{2.16}$$

$$\frac{Dv_R}{Dt} = \frac{1}{\rho J_o}\left[-J\left(\frac{p,z}{K,L}\right) + \frac{1}{4\pi} B_z \mathfrak{L}\right] \tag{2.17}$$

$$\frac{Dv_z}{Dt} = \frac{1}{\rho J_o}\left[J\left(\frac{p,R}{K,L}\right) - \frac{1}{4\pi} B_R \mathfrak{L}\right] \tag{2.18}$$

$$\frac{DB_R}{Dt} = -\frac{v_R B_R}{R} + \frac{1}{J_o}\left[B_z J\left(\frac{R,v_R}{K,L}\right) - B_R J\left(\frac{R,v_z}{K,L}\right)\right] \tag{2.19}$$

$$\frac{DB_z}{Dt} = -\frac{v_R B_z}{R} + \frac{1}{J_o}\left[B_R J\left(\frac{v_z,z}{K,L}\right) - B_z J\left(\frac{v_R,z}{K,L}\right)\right] \tag{2.20}$$

where

$$\frac{DR}{Dt} = v_R \tag{2.21}$$

$$\frac{Dz}{Dt} = v_z \tag{2.22}$$

are the equations of the particle path and

$$\mathfrak{L} = J\left(\frac{R,B_R}{K,L}\right) + J\left(\frac{z,B_z}{K,L}\right) \tag{2.23}$$

The complete set of equations includes (2.4) and (2.5) which are already in Lagrangian form.

The above set of 9 hyperbolic equations[35] contains 9 variables, E, p, ρ, v_R, v_z, B_R, B_z, R, and z.

2.2 The Numerical Method for One-dimensional Problems

When a discontinuity, such as a shock wave, is present in the flow, numerical methods for solving the nondissipative differential equations cannot be used[3] since the zero width of the discontinuity is much smaller than the assigned dimensions of zones. Another difficulty is that the number and location of these discontinuities, across which internal boundary conditions must be used, are not known before the complete set of equations is solved.

In order to overcome these difficulties, von Neumann and Richtmeyer[1] suggested the use of an artificial viscosity to eliminate the discontinuities in gasdynamic flows. The scalar artificial viscous stress term is proportional to the square of the rate of shear and can be added to the pressure. Ordinary viscosity[36], where the stress is proportional to the rate of shear, affects the flow away from the shocks and gives a shock thickness which varies inversely as shock strength, approaching zero for very strong shocks and infinity for very weak ones. Artificial viscosity, however, gives a shock thickness of a few mesh widths independent of shock strength and negligible viscous stress in the smooth portion of the flow.

Von Neumann and Richtmeyer showed that the flattened out shock propagates at the same speed as the discontinuous shock and that the artificial viscosity method does not permit the nonphysical negative shocks (sudden decompressions) which are mathematical solutions of the

jump equations.

The artificial viscosity method is applied to the MHD equations. Lagrangian coordinates are used to simplify location of free surfaces, moving boundaries, and, in particular, the position at any time of the initial discontinuity for the blast wave model. The governing equations for one-dimensional problems are written as follows in the order in which they will be solved:

$$\frac{Dv_x}{Dt} = -\frac{1}{\rho}\frac{\partial h}{\partial x}\left[\frac{\partial}{\partial h}(p+Q) - \frac{1}{8\pi}\frac{\partial}{\partial h}(B_y^2+B_z^2)\right] \tag{2.24}$$

$$\frac{Dv_y}{Dt} = \frac{1}{\rho}\frac{\partial h}{\partial x}\left[\frac{B_x}{4\pi}\frac{\partial B_y}{\partial h}\right] \tag{2.25}$$

$$\frac{Dv_z}{Dt} = \frac{1}{\rho}\frac{\partial h}{\partial x}\left[\frac{B_x}{4\pi}\frac{\partial B_z}{\partial h}\right] \tag{2.26}$$

$$\frac{Dx}{Dt} = v_x \tag{2.27}$$

$$\frac{1}{\rho}\frac{D\rho}{Dt} = -\frac{\partial v_x}{\partial h}\frac{\partial h}{\partial x} \tag{2.28}$$

$$Q = \begin{cases} \rho \bar{a}^2\left[\left(\frac{\partial v_x}{\partial h}\right)^2 + \left(\frac{\partial v_y}{\partial h}\right)^2\right], & \frac{\partial v_x}{\partial h} < 0 \\ 0, & \frac{\partial v_x}{\partial h} > 0 \end{cases} \tag{2.29}$$

$$\frac{DE}{Dt} = \frac{p+Q}{\rho^2}\frac{D\rho}{Dt} \tag{2.30}$$

$$E = \frac{p}{\rho(\gamma-1)} \tag{2.31}$$

$$\frac{DB_y}{Dt} = \frac{B_y}{\rho}\frac{D\rho}{Dt} + B_x\frac{\partial v_y}{\partial h}\frac{\partial h}{\partial x} \tag{2.32}$$

$$\frac{DB_z}{Dt} = \frac{B_z}{\rho}\frac{D\rho}{Dt} + B_x\frac{\partial v_z}{\partial h}\frac{\partial h}{\partial x} \tag{2.33}$$

where h is the dimensionless Lagrangian coordinate, Q is the stress due to artificial viscosity, and $\bar{a}$ is a coefficient of artificial viscosity. To obtain a more useful form for computations, the induction equation has been combined with the continuity equation (2.28) to give (2.32) and (2.33). In slab symmetry, Maxwell's equation gives B_x = constant.

The artificial viscous stress term, given by (2.29), is set to zero when the fluid is undergoing expansion, while for compression, it consists of the term given by von Neumann and Richtmeyer for gas-dynamic plus an additional term necessary to account for the tangential motion of fluid through the shock for MHD. The amount of visocsity is governed by the constant $\bar{a}$, a small viscosity resulting in a thin shock with some oscillations in variables, and a large viscosity in a thicker and smoother profile.

Difference equations are obtained from the above equations using the mesh shown in Figure 2.1. The mesh point (h,n) is the location x_h at time t_n of the outer boundary of the Lagrangian zone h that was initially located at $x_h = h\Delta x$ for constant Δx. In general, lines h = constant are curves in the (x,t) coordinates tracing the motion of zone h. To center the calculation of x properly, the velocity of the boundary of zone h is considered located at half intervals in time, represented as $v_h^{n+\frac{1}{2}}$, the subscript representing x position and the superscript time. All other variables p, E, B_y, etc. are considered attached to the constant mass of the zone and therefore located at its center. This characteristic of Lagrangian meshes insures a well centered difference scheme.

Using central differences in space and forward in time, the difference equations for the momentum equations, (2.24) - (2.26), are written by replacing the density ρ by the constant mass of the zone M, divided by the Volume of the zone $\forall$. To center these equations properly, the density at the mesh point h is needed; thus the average mass of the two adjacent zones is divided by the average volume which is written as the area of the interface between the two zones, A_h^n, multiplied by the distance between the centers of the two zones, $\frac{\partial x}{\partial h}$, resulting in the following expression:

$$\frac{1}{\rho}\frac{\partial h}{\partial x} = \frac{A_h^n}{\frac{1}{2}(M_{h-\frac{1}{2}} + M_{h+\frac{1}{2}})} \qquad (2.34)$$

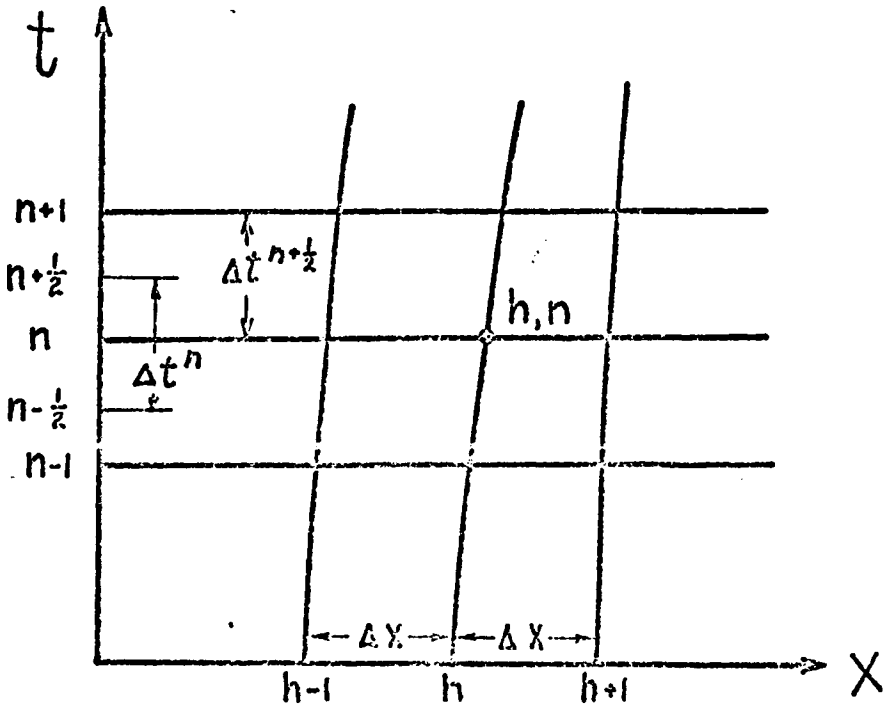

Fig. 2.1 Mesh configuration for WUNDY

Defining PQ = p + Q and noting that B_x constant, the momentum equations in the x and y directions are written as follows, (the equation in the z direction parallels (2.36)):

$$v_{x_h}^{n+\frac{1}{2}} = v_{x_h}^{n-\frac{1}{2}} + \Delta t^n A_h^n \frac{PQ_{h-\frac{1}{2}}^n - PQ_{h+\frac{1}{2}}^n + \frac{1}{8\pi}\left[\left(B_{y_{h-\frac{1}{2}}}^n\right)^2 + \left(B_{z_{h-\frac{1}{2}}}^n\right)^2 - \left(B_{y_{h+\frac{1}{2}}}^n\right)^2 - \left(B_{z_{h+\frac{1}{2}}}^n\right)^2\right]}{\frac{1}{2}\left(M_{h-\frac{1}{2}} + M_{h+\frac{1}{2}}\right)} \tag{2.35}$$

$$v_{y_h}^{n+\frac{1}{2}} = v_{y_h}^{n-\frac{1}{2}} + \Delta t^n A_h^n \frac{\frac{B_x}{4\pi}\left(B_{y_{h+\frac{1}{2}}}^n - B_{y_{h-\frac{1}{2}}}^n\right)}{\frac{1}{2}\left(M_{h-\frac{1}{2}} + M_{h+\frac{1}{2}}\right)} \tag{2.36}$$

The Eulerian coordinate is found from

$$x_h^{n+1} = x_h^n + \Delta t^{n+\frac{1}{2}} v_{x_h}^{n+\frac{1}{2}} \tag{2.37}$$

Specific volume V and density of a zone are computed from the constant mass of the zone as described above giving

$$V_{h-\frac{1}{2}}^{n+1} = \frac{1}{\rho_{h-\frac{1}{2}}^{n+1}} = \frac{V_{h-\frac{1}{2}}^{n+1}}{M_{h-\frac{1}{2}}} \tag{2.38}$$

The remaining difference equations are (an equation for B_z parallels (2.42)):

$$Q^{n+1}_{h-\frac{1}{2}} = \frac{\bar{a}^2 \left(v_{x_h}^{n+\frac{1}{2}} - v_{x_{h-1}}^{n+\frac{1}{2}}\right)^2}{\frac{1}{2}\left(V^{n+1}_{h-\frac{1}{2}} + V^{n}_{h-\frac{1}{2}}\right)} \quad \text{for} \quad \frac{\partial v_x}{\partial x} < 0 \tag{2.39}$$

$$p^{n+1}_{h-\frac{1}{2}} = \frac{2E^{n}_{h-\frac{1}{2}} - \left(p^{n}_{h-\frac{1}{2}} + 2Q^{n+1}_{h-\frac{1}{2}}\right)\left(V^{n+1}_{h-\frac{1}{2}} - V^{n}_{h-\frac{1}{2}}\right)}{\frac{\gamma+1}{\gamma-1} V^{n+1}_{h-\frac{1}{2}} - V^{n}_{h-\frac{1}{2}}} \tag{2.40}$$

$$E^{n+1}_{h-\frac{1}{2}} = \frac{p^{n+1}_{h-\frac{1}{2}} V^{n+1}_{h-\frac{1}{2}}}{\gamma-1} \tag{2.41}$$

$$B_{y}{}^{n+1}_{h-\frac{1}{2}} = \frac{B_{y}{}^{n}_{h-\frac{1}{2}} \left[1 + \frac{\rho^{n+1}_{h-\frac{1}{2}} - \rho^{n}_{h-\frac{1}{2}}}{\rho^{n+1}_{h-\frac{1}{2}} + \rho^{n}_{h-\frac{1}{2}}}\right] + \Delta t^{n+\frac{1}{2}} B_x \frac{v_{y_h}^{n+\frac{1}{2}} - v_{y_{h-1}}^{n+\frac{1}{2}}}{x^{n+1}_h - x^{n+1}_{h-1}}}{1 - \frac{\rho^{n+1}_{h-\frac{1}{2}} - \rho^{n}_{h-\frac{1}{2}}}{\rho^{n+1}_{h-\frac{1}{2}} + \rho^{n}_{h-\frac{1}{2}}}} \tag{2.42}$$

Equation (2.40) was obtained by combining the energy equation (2.30) with the equation of state (2.31) and solving for the pressure which is implicit in the coefficient. Similarly, the induction equation, implicit in B_y, was altered to obtain (2.42).

A one-dimensional computer program, MHD WUNDY, based on a gasdynamic code[4,5], is developed which solves the above equations in

slab, cylindrical, or spherical geometry, in the order presented, with auxiliary equations determining the volume of a zone and the area of its interface.

The time step used to advance the calculation is governed by two very different stability criteria. In the smooth region away from the shock, the differential equations are hyperbolic; therefore stability is governed by the well established Courant-Friedricks-Lewy condition[3] which for MHD is as follows:

$$\Delta t \leq \frac{\Delta x}{c^*} \tag{2.43}$$

where c^* is the magnetosonic wave speed given by

$$c^* = \left(\frac{\gamma p}{\rho} + \frac{B^2}{4\pi\rho}\right)^{\frac{1}{2}} \tag{2.44}$$

In the shock region, the differential equations are parabolic and stability is governed by a criteria developed by von Neumann and Richtmeyer[1] which can be represented as follows:

$$\Delta t \leq \frac{\Delta x}{4\bar{a}^2|\Delta v_x|} \tag{2.45}$$

where Δv_x is the difference in velocity over a mesh width Δx. MHD WUNDY combines both (2.43) and (2.45) into one general criteria for both regions which gives a smaller time step than either separately.

$$\Delta t^{n+\frac{1}{2}} = \frac{f_s \left(x_h^n - x_{h-1}^n\right)}{c^*_{h-\frac{1}{2}}{}^n + 4\bar{a}^2 \left| v_{x_h}^{n-\frac{1}{2}} - v_{x_{h-1}}^{n-\frac{1}{2}} \right|} \tag{2.46}$$

where f_s is a constant factor of safety, usually about 0.8.

The calculation is advanced using the minimum value of Δt over the whole mesh at a given time. Of course, these are only necessary conditions for stability. To be completely sure of stability, numerical solutions were compared with known solutions.

The computer program, MHD WUNDY, contains many subprograms, each of which carries out a separate part of the computation. The basic calculation of variables, equations (2.35) - (2.42), as well as the determination of the time step, equation (2.46), are contained in the main calculation subroutine. The program is set up to solve problems using more complicated equations of state than the ideal gas equation (2.5), if desired. The solution of each equation of state is in a separate subroutine. Those calculations governed by the geometry of the problem (slab symmetry, cylindrical, or spherical), including area and volume of a zone, are placed in another subprogram. Most problems may be initialized, that is, all zones given initial values of density, pressure, etc. through about 15 data cards, which are read into the machine using another subroutine. The primary output, a table of all variables for each zone for given times, is printed out under the control of yet another subprogram. Additional output subroutines print information such as

tables of variables versus time at fixed positions, or tables of shock location, pressure, etc. as functions of time. In addition, there are four rezoning subprograms which repair the distortions of the Lagrangian mesh caused by the fluid motion.

The first rezoning subprogram corrects the problem of a compressed zone out of the region of interest (the main shock wave) which keeps the time step needlessly small. This subprogram seeks out the compressed zone and combines it with its neighbor thus increasing the timestep and therefore the efficiency of the calculation. The second subprogram is useful when the shock has reached the outer boundary of the problem. This subprogram moves the boundary out by a factor of two while combining zones behind the shock to release enough zones to cover the region added, thus allowing the program to run indefinitely.

The third rezoning subprogram keeps the total number of zones calculated small in order to reduce machine time. Since fine zones are only needed for calculations in the shock region, the mesh is formed initially of large zones. When the shock wave approaches one of these large zones, it is subdivided into fine zones. After the shock has passed through these fine zones, they are recombined into one large zone again. The fourth subprogram at later times combines the now low density zones of an initially high density sphere into larger zones to increase the time step.

Of course, MHD WUNDY can be used for problems described by only one space coordinate, but the numerical method outlined here, applied to two-dimensional problems, should result in a successful two-dimensional computer program.

2.3 The Numerical Method for Two-dimensional Problems

The two-dimensional computer code, MHD CYCLONE, is based, in part, on a two-dimensional gasdynamic program[6] and, in part, on the numerical method presented for one-dimensional MHD problems. The axisymmetric, cylindrical MHD equations in Lagrangian coordinates (2.4), (2.5) and (2.16) - (2.23) are written in difference form using the mesh shown in Figure 2.2. Since the geometry of the problem of interest is spherical, it was found convenient to introduce a set of Eulerian axisymmetric spherical coordinates (r,θ) and to obtain the components of the vectors $\vec{v}$ and $\vec{B}$ in spherical coordinates as well as cylindrical. Initially, the Lagrangian coordinates K and L correspond to θ and r respectively.

As in WUNDY, position and velocity are associated with the boundary of the zone (K,L), while pressure, energy, etc., are affixed to the mass at its center $(K - \frac{1}{2},\ L - \frac{1}{2})$ in order to center the calculation properly. The Jacobian of the transformation from the (K,L) plane to the (R,z) plane, J_O, given by (2.15), is equal to the area of the figure in the (R,z) plane corresponding to unit area in the (K,L) plane (in the limit of small areas). Since a zone in the (K,L) plane, by definition, contains unit area, J_O is simply the area of the zone in the (R,z) plane. Expanding J_O and using central differences for all derivatives, the following result is obtained:

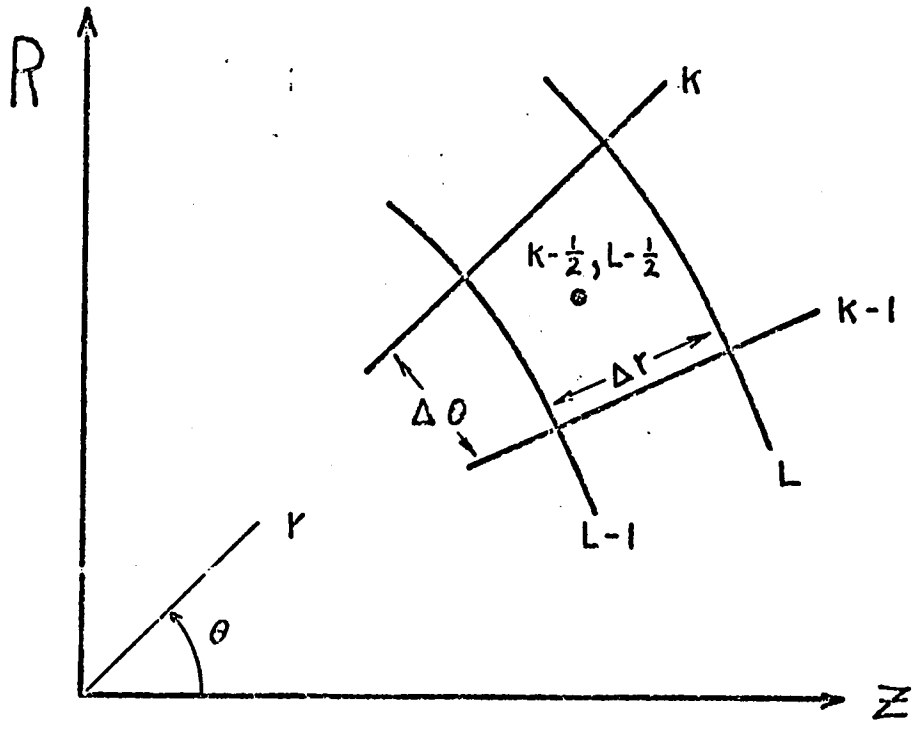

Fig. 2.2 Initial mesh configuration for CYCLONE

$$J_{o_{K-\frac{1}{2},L-\frac{1}{2}}} = J\left(\frac{R,z}{K,L}\right)_{K-\frac{1}{2},L-\frac{1}{2}} = \left(\frac{\partial R}{\partial K}\frac{\partial z}{\partial L}\right)_{K-\frac{1}{2},L-\frac{1}{2}} - \left(\frac{\partial R}{\partial L}\frac{\partial z}{\partial K}\right)_{K-\frac{1}{2},L-\frac{1}{2}} \tag{2.47}$$

where for example

$$\left(\frac{\partial R}{\partial K}\right)_{K-\frac{1}{2},L-\frac{1}{2}} = \tfrac{1}{2}\left[(R_{K,L} - R_{K-1,L}) + (R_{K,L-1} + R_{K-1,L-1})\right] \tag{2.48}$$

and

$$\left(\frac{\partial R}{\partial L}\right)_{K-\frac{1}{2},L-\frac{1}{2}} = \tfrac{1}{2}\left[(R_{K,L} - R_{K,L-1}) + (R_{K-1,L} - R_{K-1,L-1})\right] \tag{2.49}$$

All other Jacobians in the equations may be written in the same manner, for example for a variable attached to the boundary of a zone

$$J\left(\frac{R,v_R}{K,L}\right) = \left(\frac{\partial R}{\partial K}\frac{\partial v_R}{\partial L}\right)_{K-\frac{1}{2},L-\frac{1}{2}} - \left(\frac{\partial R}{\partial L}\frac{\partial v_R}{\partial K}\right)_{K-\frac{1}{2},L-\frac{1}{2}} \tag{2.50}$$

where

$$\left(\frac{\partial v_R}{\partial L}\right)_{K-\frac{1}{2},L-\frac{1}{2}} = \tfrac{1}{2}\left[(v_{R_{K,L}} - v_{R_{K,L-1}}) + (v_{R_{K-1,L}} - v_{R_{K-1,L-1}})\right] \tag{2.51}$$

and for a variable associated with the center of a zone

$$J\left(\frac{p,z}{K,L}\right) = \left(\frac{\partial p}{\partial K}\frac{\partial z}{\partial L}\right)_{K,L} - \left(\frac{\partial p}{\partial L}\frac{\partial z}{\partial K}\right)_{K,L} \tag{2.52}$$

where

$$\left(\frac{\partial p}{\partial K}\right)_{K,L} = \frac{1}{2}\left[(p_{K+\frac{1}{2},L+\frac{1}{2}} - p_{K-\frac{1}{2},L-\frac{1}{2}}) + (p_{K+\frac{1}{2},L-\frac{1}{2}} - p_{K-\frac{1}{2},L-\frac{1}{2}})\right] \tag{2.53}$$

and

$$\left(\frac{\partial z}{\partial L}\right)_{K,L} = \frac{1}{2}(z_{K,L+1} - z_{K,L-1}) \tag{2.54}$$

Using the above definitions, the difference equations are written in the order of solution. The equations of motion are:

$$v_{R_{K,L}}^{n+\frac{1}{2}} = v_{R_{K,L}}^{n-\frac{1}{2}} + \frac{\Delta t^n R_{K,L}^n}{\bar{M}_{K,L}}\left[\frac{1}{4\pi} B_{z_{avg}}^n \mathcal{L}_{K,L}^n - J\left(\frac{PQ,z}{K,L}\right)_{K,L}^n\right] \tag{2.55}$$

and

$$v_{z_{K,L}}^{n+\frac{1}{2}} = v_{z_{K,L}}^{n-\frac{1}{2}} - \Delta t^n \frac{R_{K,L}^n}{\bar{M}_{K,L}}\left[\frac{1}{4\pi} B_{R_{avg}}^n \mathcal{L}_{K,L}^n - J\left(\frac{PQ,z}{K,L}\right)_{K,L}^n\right] \tag{2.56}$$

where $\bar{M}_{K,L}$ is the mass assigned to the mesh point (K,L) and is the average of the masses of the four adjoining zones, $B_{z_{avg}}$ $B_{R_{avg}}$ are the components of magnetic field averaged over the four zones and

$$\mathcal{L}_{K,L}^n = J\left(\frac{R,B_R}{K,L}\right)_{K,L}^n + J\left(\frac{z,B_z}{K,L}\right)_{K,L}^n \tag{2.57}$$

The equations of the particle line are:

$$R_{K,L}^{n+1} = R_{K,L}^n + \Delta t^{n+\frac{1}{2}} v_{R_{K,L}}^{n+\frac{1}{2}} \tag{2.58}$$

and

$$z^{n+1}_{K,L} = z^{n}_{K,L} + \Delta t^{n+\frac{1}{2}} v_{z}{}^{n+\frac{1}{2}}_{K,L} \tag{2.59}$$

The induction equations are:

$$B_{R}{}^{n+1}_{K-\frac{1}{2},L-\frac{1}{2}} = B_{R}{}^{n}_{K-\frac{1}{2},L-\frac{1}{2}} + \Delta t^{n} \left\{ \frac{-v_{R_{avg}}{}^{n+\frac{1}{2}}}{R_{avg}^{n+1}} B_{R}{}^{n}_{K-\frac{1}{2},L-\frac{1}{2}} + \left[\frac{B_{z}^{n} J(\frac{R, v_{R}}{K,L})^{n+1} - B_{R}^{n} J(\frac{R, v_{z}}{K,L})^{n+1}}{J_{o}^{n+1}} \right]_{K-\frac{1}{2},L-\frac{1}{2}} \right\} \tag{2.60}$$

and

$$B_{z}{}^{n+1}_{K-\frac{1}{2},L-\frac{1}{2}} = B_{z}{}^{n}_{K-\frac{1}{2},L-\frac{1}{2}} + \Delta t^{n} \left\{ \frac{v_{R_{avg}}{}^{n+\frac{1}{2}}}{R_{avg}^{n+1}} B_{z}{}^{n}_{K-\frac{1}{2},L-\frac{1}{2}} + \left[B_{R}^{n} J(\frac{v_{z}, z}{K,L})^{n+1} - B_{z} J(\frac{v_{R}, z}{K,L})^{n+1} \right]_{K-\frac{1}{2},L-\frac{1}{2}} \right\} \tag{2.61}$$

where $v_{R_{avg}}$ and R_{avg} are the quantities v_R and R respectively averaged at the four mesh points bounding the zone.

The specific volume and therefore the density is computed from:

$$V^{n+1}_{K-\frac{1}{2},L-\frac{1}{2}} = \frac{R_{avg}^{n+1} J_{o}{}^{n+1}_{K-\frac{1}{2},L-\frac{1}{2}}}{M_{K-\frac{1}{2},L-\frac{1}{2}}} \tag{2.62}$$

The artificial viscous stress term, analogous to that used for MHD WUNDY, consists of velocity derivatives in the radial direction, according to the assumption that the shock waves will be primarily radial. Once again, the viscosity term, given below, will be set to zero when the fluid is expanding.

$$Q^{n+1}_{K-\frac{1}{2},L-\frac{1}{2}} = \frac{\bar{a}^2 \left(\frac{\partial v_r}{\partial L}\right)^{n+\frac{1}{2}\ 2}_{K-\frac{1}{2},L-\frac{1}{2}} + \left(\frac{\partial v_\theta}{\partial L}\right)^{n+\frac{1}{2}\ 2}_{K-\frac{1}{2},L-\frac{1}{2}}}{\frac{1}{2}\left(V^{n+1}_{K-\frac{1}{2},L-\frac{1}{2}} + V^{n}_{K-\frac{1}{2},L-\frac{1}{2}}\right)} \qquad (2.63)$$

In order to center the calculation of pressure and specific internal energy properly, one iteration is performed to obtain a more up to date value of pressure in the coefficient of the energy equation. The difference equations are

$$E^{n+1}_{K-\frac{1}{2},L-\frac{1}{2}} = E^{n}_{K-\frac{1}{2},L-\frac{1}{2}} - PQ^{n+1}_{K-\frac{1}{2},L-\frac{1}{2}}\left(V^{n+1} - V^{n}\right)_{K-\frac{1}{2},L-\frac{1}{2}} \qquad (2.64)$$

$$P^{n+1}_{K-\frac{1}{2},L-\frac{1}{2}} = \frac{E^{n+1}_{K-\frac{1}{2},L-\frac{1}{2}}(\gamma-1)}{V^{n+1}_{K-\frac{1}{2},L-\frac{1}{2}}} \qquad (2.65)$$

The timestep in the smooth flow (hyperbolic) region is found from a generalization of the one-dimensional Courant-Friedricks-Lewy condition[3] and involves two separate criteria in the r and θ directions

which are

$$\Delta t \leq \frac{\Delta r}{c^*} \tag{2.66}$$

$$\Delta t \leq \frac{r\Delta\theta}{c^*} \tag{2.67}$$

The criteria in the shock region, similar to the shock criteria for MHD WUNDY, is

$$\Delta t \leq \frac{\Delta r}{4\bar{a}^2}\Delta v_r \tag{2.68}$$

In the calculation, the timestep is advanced using the smallest of (2.66) - (2.68) over the entire mesh, multiplied by an appropriate factor of safety. Repeated numerical tests have shown this method to be stable. However, errors are introduced into the calculation through the distortion of the Lagrangian mesh due to the motion of the fluid. To avoid these errors, a rezoning scheme is introduced into the code.

The rezoning introduced serves two general purposes; first, to remove large distortions in the mesh, and second, to increase the mesh width Δr away from the shock, thus increasing the time step of the calculation. The first stage in the rezoning scheme is to restore the distorted zone, given by ABCD in Figure 2.3, to its initial constant θ lines, EF and GH, before the distortion becomes large. To accomplish this, mesh point A with a Lagrangian label (K,L) is moved to point E along the curve AD, mesh point B, with label (K,L-1), is moved to

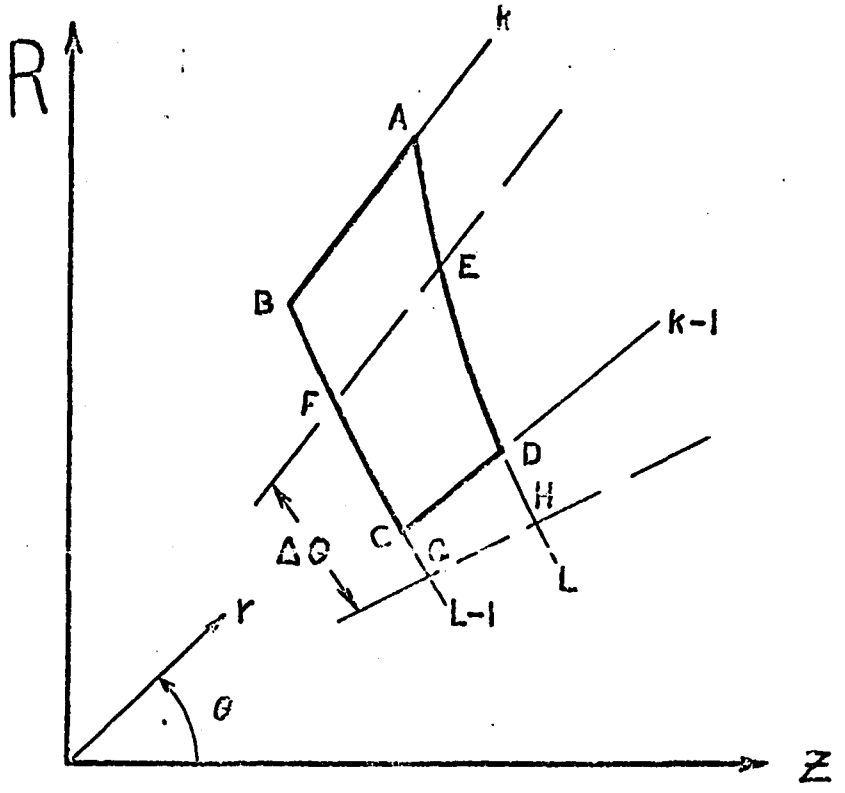

Fig. 2.3 Distorted CYCLONE mesh

point F along curve BC, etc. Curves AD and BC are assumed to be straight lines so that the computation of r_E, r_F, etc. involves linear interpolation in θ, i.e.

$$r_E = r_A - \left(\frac{\theta_A - \theta_E}{\theta_A - \theta_D}\right)(r_A - r_D) \tag{2.69}$$

The new zone EFGH retains its Lagrangian label $(K-\frac{1}{2}, L-\frac{1}{2})$ but contains a different mass, equal to the old mass plus the mass contained in CDHG minus the mass of figure ABFE. All variables in the new zone are found by linear interpolation similar to (2.69). Variables centered at the midpoint of a zone are interpolated using the θ coordinate of the midpoint. Best results using this scheme are obtained when rezoning is applied before any mesh point has displaced in the θ direction one-half of the initial $\Delta\theta$, but the procedure is valid until the mesh point has displaced a full $\Delta\theta$. The scheme conserves the mass and energy of the mesh to within one thousandth of one percent.

To increase the mesh width Δr, and thereby the time step, a radial rezoning scheme now searches out a zone with Δr smaller than a minimum value specified for the problem, and combines it with its neighbor. In order to preserve the correct differencing scheme, if a zone having a Lagrangian label (K_1, L_1) is combined with $(K_1, L_1 + 1)$, all other zones K, having the label L, must be combined with their neighbors as well. The rezoning is accomplished in a way designed to

conserve the mass and energy of the system. These radial rezonings also release zones which may be used to extend the outer boundary of the problem.

The MHD CYCLONE code is under the control of six data cards which give the geometry, program constants, conditions for rezoning, and initial values of variables. All variables except mass are initialized over all mesh points by one subroutine. The mass is initialized in a new subroutine which is also used to recalculate the mass after rezoning. The basic calculation is performed in a main subprogram which calls on separate subprograms containing the equation of motion, equation of state, and the stability criteria. A primary output subroutine prints a table of variables at fixed times for fixed K. In addition, a new subroutine which transforms the vector variables into spherical coordinates has been added. This subroutine is necessary for the rezoning scheme in addition to providing print out of results in a useful form. The rezoning is contained in one main subprogram which performs both types of rezoning. In addition, an auxiliary subroutine can be used to extend the boundary of the problem if necessary. The rezoning is automatically carried out as many times as needed in the calculation.

The MHD CYCLONE code, written in the Fortran-IV-G language applicable to an IBM-360/50 computer, has been converted into double precision mode to eliminate roundoff errors.

2.4 Summary

In this chapter, the nondissipative MHD equations have been written in Lagrangian coordinates giving, at any time, the initial position of an element of mass. The von Neumann-Richtmeyer method of artificial viscosity, developed for gasdynamics, has been extended to MHD flows. Both one-dimensional (MHD WUNDY) and two-dimensional (MHD CYCLONE) computer codes have been written. Rezoning, necessary to remove distortions in the Lagrangian mesh due to the motion of the plasma, has been added. The computer programs will be used to study MHD nonlinear wave problems, in particular, the sudden expansion of plasma into an MHD medium with a uniform magnetic field.

CHAPTER 3

THE PLANAR MHD PISTON PROBLEM

The planar MHD piston model, a piston pushed at a constant speed, $\vec{v}_p = (v_{xp}, v_{yp})$, into an ambient MHD medium with a uniform magnetic field, $\vec{B}_o = (B_{xo}, B_{yo})$, has been extensively studied. Since the MHD equations in slab symmetry are reducible, the solutions are regions of constant state separated by MHD shock waves or simple rarefaction (expansion) waves in the order given by the Friedricks diagram, Figure 1.1, fast, Alfven, and slow.

New planar piston solutions are presented here in order to make qualitative predictions of the spherical piston solutions. In addition, particular emphasis is placed on special solutions such as the mechanism of switch-on shocks. Theoretical solutions to planar piston problems are compared with computer solutions in order to investigate the stability and convergence of the numerical method.

3.1 Comparisons Between Computer Results and Theoretical Solutions

The existing theoretical methods of investigating the stability and convergence of numerical solutions for nonlinear partial differential equations involve linearizing these equations and so give, at most, necessary but not sufficient conditions[2,3]. Therefore in order to conclusively determine stability and convergence, it is necessary to compare planar piston solutions obtained using the computer with known theoretical solutions, such as the Bazer and Ericson shock solutions of Appendix A, the gasdynamic piston solution of Appendix B, and a new theoretical solution for planar MHD piston problems, presented in Appendix C.

The one-dimensional computer program, MHD WUNDY, was used to solve piston problems for different magnitudes and orientations of uniform magnetic fields for an atmosphere at an altitude of 200 km. given by (2.7) and for a constant piston speed, $v_{xp} = 10^6$ cm/sec. A magnetic field in the x direction is decoupled from the fluid motion giving the gasdynamic solution. This solution, a gasdynamic shock followed by a constant state with velocity v_{xp} extending up to the piston, is compared in Table 3.1 with the computer solution and with the solution in the limiting case of a very strong shock ($v_{xp} >> a_o$), given by equations (B8) - (B10) of Appendix B. The computer results are in excellent agreement with the theoretical solution and both are closely

approximated by the strong shock solution since, for the given data, $v_{xp}/a_o = 14.14$.

TABLE 3.1 Gasdynamic Piston Results

Quantity	Computer Value	Theoretical Value	Strong Shock Value
ρ_1/ρ_o	3.955	3.96	4
U/v_{xp}	1.340	1.338	1.333
p_1/p_o	447	447	∞

The Bazer and Ericson MHD shock solutions, equations (A7) - (A13), are necessarily in terms of an arbitrary paramter g since there is one more unknown than shock equation. For the gasdynamic piston problem, the introduction of the known piston velocity created a self-consistent set of equations to which there is a unique solution. A new MHD piston solution is derived in Appendix C assuming a constant state extending from the shock back to the piston, analogous to gas-dynamics. This solution, given by (C6) - (C10), is always valid when the uniform magnetic field is transverse to the piston motion ($B_x = 0$), but in practical calculations, it is also valid for arbitrary orientations of the magnetic field as long as $s_o = a_o^2/b_o^2$ is sufficiently large that the velocity behind the shock is the piston velocity.

Table 3.2 presents the solutions for a magnetic field $B_o = 0.1$ gauss oriented at angles $\bar{\theta}$ to the x axis of 0^o (the solution of Table 3.1), 30^o and 90^o. For $\bar{\theta} = 30^o$, a very weak slow wave is present near the piston but, in the constant state ahead of it, the velocity is v_{xp}. In all cases, the relative error of the computer solution is always far less than one percent. The two values of the pressure ratio in columns 4 and 6 are the separate solutions obtained from equations (C9) and (C10) of Appendix C which should be identical for an exact solution. It was found simpler to use this solution, where applicable, since for most problems, the Bazer and Ericson solutions must be solved by calculating machine to obtain the same precision which can be obtained from (C6) - (C10) by slide rule.

TABLE 3.2 MHD Piston Problems for $B_o = 0.1$ gauss

Quantity	$\bar{\theta} = 0^o$	$\theta = 30^o$		$\theta = 90^o$	
		Computer	Theoretical	Computer	Theoretical
$f = \rho_1/\rho_o$	3.955	3.93	3.93	3.88	3.88
U/v_{xp}	1.340	1.345	1.343	1.348	1.348
p_1/p_o	447	442	443 442	431	432 431
B_{y_1}/B_{y_o}	--	3.97	3.96	3.88	3.88
u_{y_1}/v_{xp}	0	-.00765	-.00764	0	0

Problems were also solved numerically for the same ambient data and larger magnetic fields. These results, which will be presented later, were again checked with the solutions of Appendix C, and also with the results of Bazer and Ericson, (A6) - (A12), giving the same excellent agreement. In addition, numerical solutions obtained for totally different ambient data also checked out. The results showed the solutions to be basically independent of mesh width Δx and coefficient of artificial viscosity $\bar{a}$ chosen. Of course, larger Δx and smaller $\bar{a}$ result in small oscillations about the basic solution. A mesh width of 100 cm. and a coefficient $\bar{a} = 2$ were chosen to damp the oscillations and still leave the time step sufficiently large for practical calculations.

The two-dimensional computer program, MHD CYCLONE, was used to solve the same problems, giving solutions identical to the above. Further comparisons of CYCLONE results for two-dimensional problems establish that this program also gives correct solutions. Therefore, both programs are considered to be stable and to give results which converge to the true solutions.

3.2 Switch-on MHD Shocks Generated by Piston Motions

A piston pushing at speed $\vec{v}_p = (v_{xp}, 0)$ into an axial magnetic field $\vec{B}_o = (B_{xo}, 0)$ generates a gasdynamic shock (the magnetic field is uncoupled from the flow). However, the Bazer and Ericson shock solutions[29], in this limit ($\bar{\theta}$ approaches zero), give a switch-on shock, that is, a fast MHD shock with zero transverse component of magnetic field ahead of it (the transverse component of magnetic field behind it has been switched on by the shock). Since it is anticipated that the spherical piston solution, as $\bar{\theta}$ approaches zero, will not correspond to the gasdynamic solution, switch-on shocks are studied here for the simpler geometry.

Switch-on shocks are generated by the computer by a piston motion, $\vec{v} = (v_{xp}, v_{yp})$, including both longitudinal and transverse velocity components, into an ambient medium with a longitudinal magnetic field B_x. Through a Galilean transformation which eliminates the longitudinal velocity component v_{xp}, the transverse velocity component, v_{yp}, is seen to pull upward the longitudinal magnetic lines of force in a thin layer adjacent to the piston (frozen in fields), thus creating a transverse component of magnetic field, B_y, in this layer. The resulting magnetic field gradient, $\partial B_y/\partial x$, produces a magnetic force in the x direction which is the gradient of the magnetic pressure, $p_m = B_y^2/8\pi$, causing a motion of the fluid in the layer. The waves produced propagate out from the piston, adjusting the motion of

the fluid to the piston.

Using MHD WUNDY, solutions were obtained for different magnetic fields, B_x, for a piston motion, $v_p = (1,1) \times 10^8$ cm/sec. for the ambient data given by (2.7). These results are presented in Figures 3.1 and 3.2 for seven values of B_x, at a time $t = 1.450 \times 10^{-3}$ sec. Figure 3.1 shows the switched-on transverse magnetic fields while Figure 3.2 gives the pressure variations. Since the solution is a function of the ratio x/t, the results at any other time differ only by a change in position.

Curve 1, Figure 3.2, shows the solution for $B_x = 0.5$ gauss which is a gasdynamic shock rather than a switch-on shock, followed by a region of constant state, a slow centered switch-on rarefaction wave, and another region of constant state at the piston. Note that B_y is zero in Figure 3.1 in the constant state behind the gasdynamic shock. The results can be explained by use of the Friedrichs diagram, Figure 1.1. For this data, the fast and slow wave speeds behind the shock are as given in Figure 1.1a, (a > b), for $\overline{\theta} = 0$. The fast wave, with speed $c_f = a$, is uncoupled from the magnetic field, resulting in the gasdynamic shock. The slow wave, with speed $c_s = b_x$, carries the magnetic effects. A particle traveling through this slow wave suffers a decrease in p, ρ, and v_x, while v_y and B_y increase in magnitude[17].

Increasing B_x to 0.8 gauss, curve 2, and to 0.9 gauss, curve 3, results in larger values of b_x so that the magnetic effects are over-

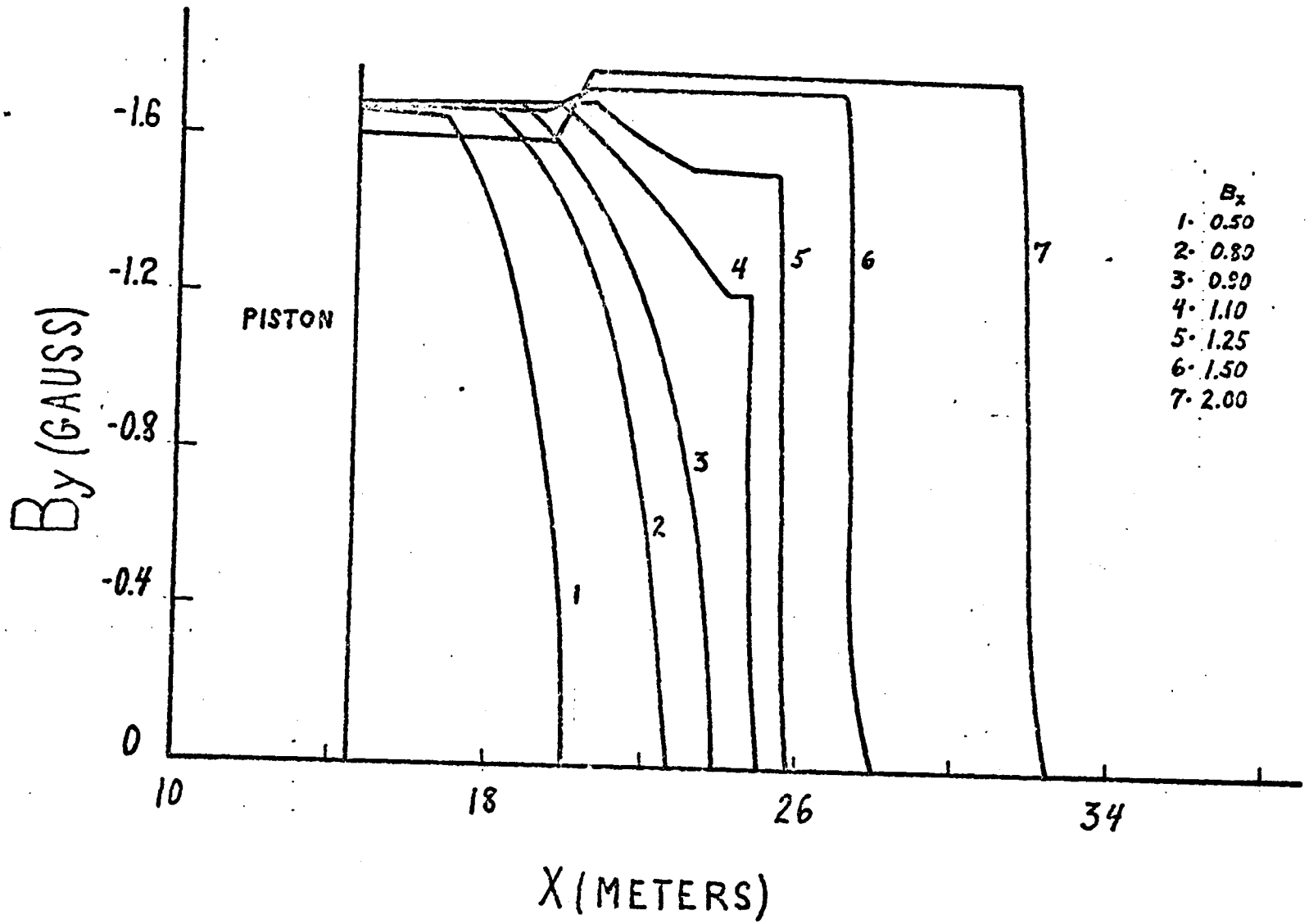

Fig. 3.1 Tangential magnetic field vs. position ($t = 1.450 \times 10^{-3}$ sec) for axial uniform magnetic fields B_x

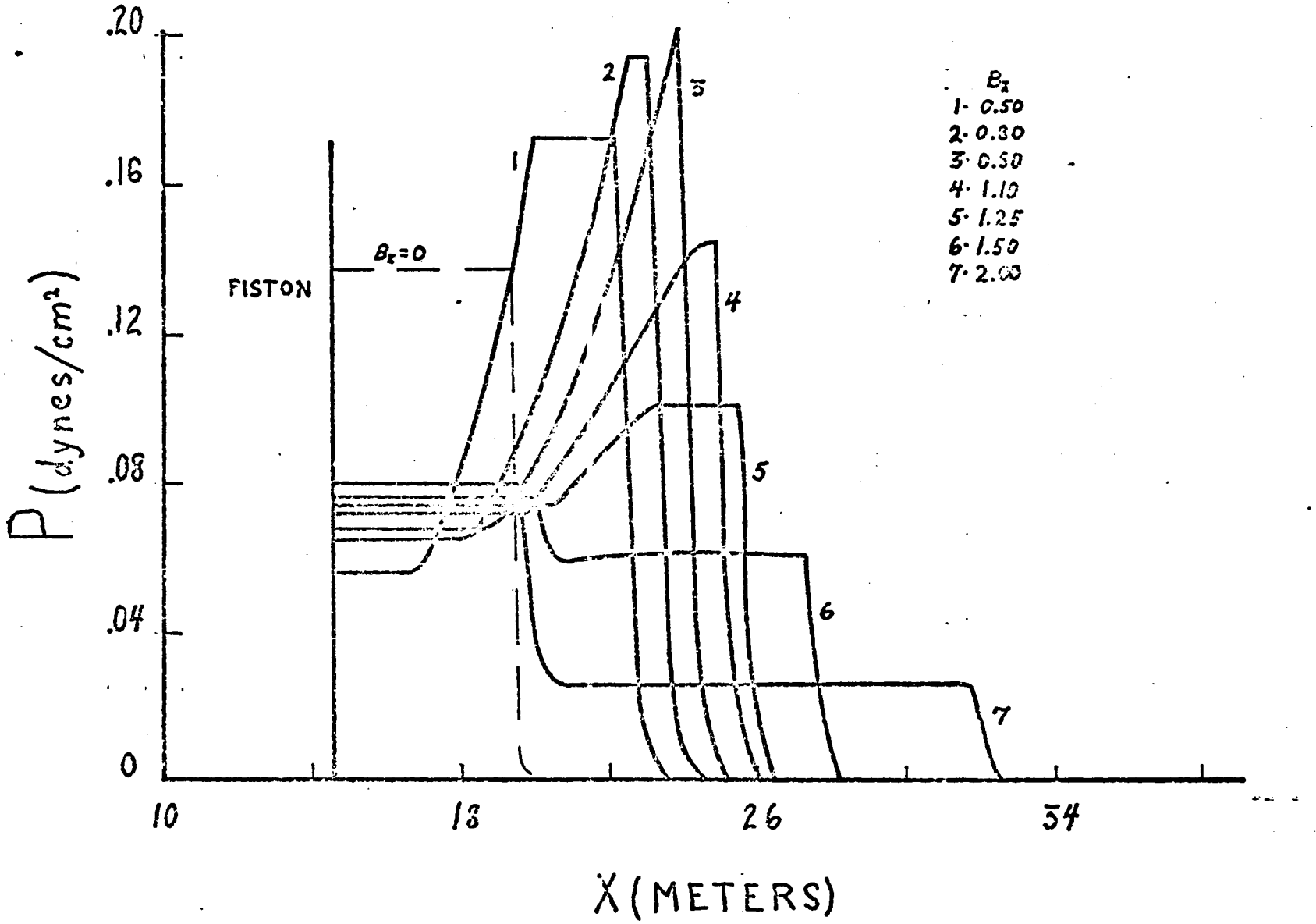

Fig. 3.2 Pressure vs. position (t = 1.450 x 10^{-3} sec) for axial uniform magnetic fields B_x

taking the gasdynamic effects carried by the fast shock. At $B_x = 1.10$ gauss, curve 4, the magnetic field is interacting with the fast gas shock, producing a switch-on shock which is followed by a slow rarefaction wave. At $B_x = 1.25$ gauss, curve 5, the Alfven speed is greater than the sound speed, so that Figure 1.1b applies behind the shock. The fast wave now carries the bulk of the magnetic effects, but since B_y is not zero behind the shock, $\overline{\theta}$ is not zero in the Friedrichs diagram, and both fast and slow waves are coupled to the magnetic field.

As B_x is increased, $|B_y|$ and v_y increase behind the shock which propagates faster, while p, ρ, and v_x decrease. The slow rarefaction wave needed to adjust the fluid motion to the piston motion v_{yp} becomes weaker as v_y increases behind the shock. As B_x is increased further, the magnitude of v_y eventually becomes larger than v_{yp}. Therefore, the boundary condition can no longer be satisfied by this slow rarefaction wave which increases v_y. A slow compression wave, which reduces v_y and $|B_y|$ while increasing p, ρ, and v_x, is necessary to satisfy this boundary condition. This wave immediately steepens into a slow shock[17]. The solution, a fast shock followed by a slow shock, is given by curves 6 and 7 in Figures 3.1 and 3.2. As B_x increases, the slow shock falls further behind the fast shock and has larger pressure and density jumps, corresponding more closely to the gasdynamic shock present for $B_x = 0$, shown using dashed lines in Figure 3.2.

It is noted that the solution changes from a gasdynamic shock followed by a switch-on wave to a switch-on shock as the strength of the magnetic field is increased. The change occurs at the magnetic field at which the Alfven speed $b_{x_o} = (B_x^2/4\pi\rho)^{\frac{1}{2}}$ becomes greater than the piston speed, v_{xp}, (the piston becomes subalfvenic): At this field, the Alfven speed behind the shock becomes greater than the sound speed, i.e., the magnetic effects overtake the gasdynamic shock. These results make us suspect that the solutions for arbitrary angles of magnetic field, $\overline{\theta}$, will be radically different for superalfvenic and subalfvenic piston motions.

3.3 Numerical Solutions to Planar Piston Problems

The major problem of interest is a spherical gas bubble or piston propagating at a constant speed into a uniform magnetic field. This two-dimensional problem is investigated qualitatively by treating a solid angle of the sphere as a planar piston pushing into an MHD medium with a magnetic field oriented at an angle $\bar{\theta}$ to the direction of propagation (the x-direction).

Computer results were given in Table 3.2 for the ambient data given by (2.7) and for a small magnetic field, $B_o = 0.1$ gauss, at angles $\bar{\theta} = 0^o$, 30^o, and 90^o to the x axis. These results show that, as the transverse component of magnetic field becomes larger, the shock wave propagates faster and its gasdynamic strength (density and pressure) is diminished. For the special case of $B_x = 0$ and $\gamma = 2$, this may be shown theoretically by using the method of Appendix C to obtain the following solution:

$$U/v_{xp} = \frac{\gamma+1}{4} + \left[\left(\frac{\gamma+1}{4}\right)^2 + \frac{c_o^{*2}}{v_{xp}^2}\right]^{\frac{1}{2}} \tag{3.1}$$

$$\rho_1/\rho_o = \frac{U}{U - v_{xp}} = B_{y_1}/B_{y_o} \tag{3.2}$$

$$p_1/p_o = 1 + \frac{\gamma U}{a_o}\frac{v_{xp}}{a_o} - \frac{\gamma}{2}\frac{b_o^2}{a_o^2}\left[(\rho_1/\rho_o)^2 - 1\right] \tag{3.3}$$

where c_o^* is the magnetosonic speed given by

$$c_o^* = (a_o^2 + b_o^2)^{\frac{1}{2}} \tag{3.4}$$

Comparison with the gasdynamic solution, equations (B5) - (B-7) of Appendix B, reinforces the above hypothesis. The mechanism for these variations is the magnetic pressure, $p_m = B_y^2/8\pi$, which pushes the shock out faster. This naturally results in less compression and a weaker shock.

For $0 < \bar{\theta} < 90^o$, the longitudinal component of magnetic field, B_x, introduces a transverse component of velocity, v_{y_1}, behind the shock. As B_o is increased, v_{y_1} increases in magnitude. The boundary condition at the piston, $v_{yp} = 0$, according to the discussion given for switch-on shocks, can only be satisfied by a slow simple MHD compression wave which steepens into a slow MHD shock. The complete solution is the ambient region, given by subscript 0, a fast MHD shock, followed by a region of constant state, subscript 1, a slow shock, and another region of constant state, given by subscript 2, extending to the piston.

Solutions are obtained, using MHD WUNDY, for two magnetic fields, $B_o = 0.5$ gauss (a superalfvenic piston), and $B_o = 2.0$ gauss (a subalfvenic piston) for different orientations of magnetic field. The results are presented in Figures 3.3 - 3.6 as functions of the magnetic

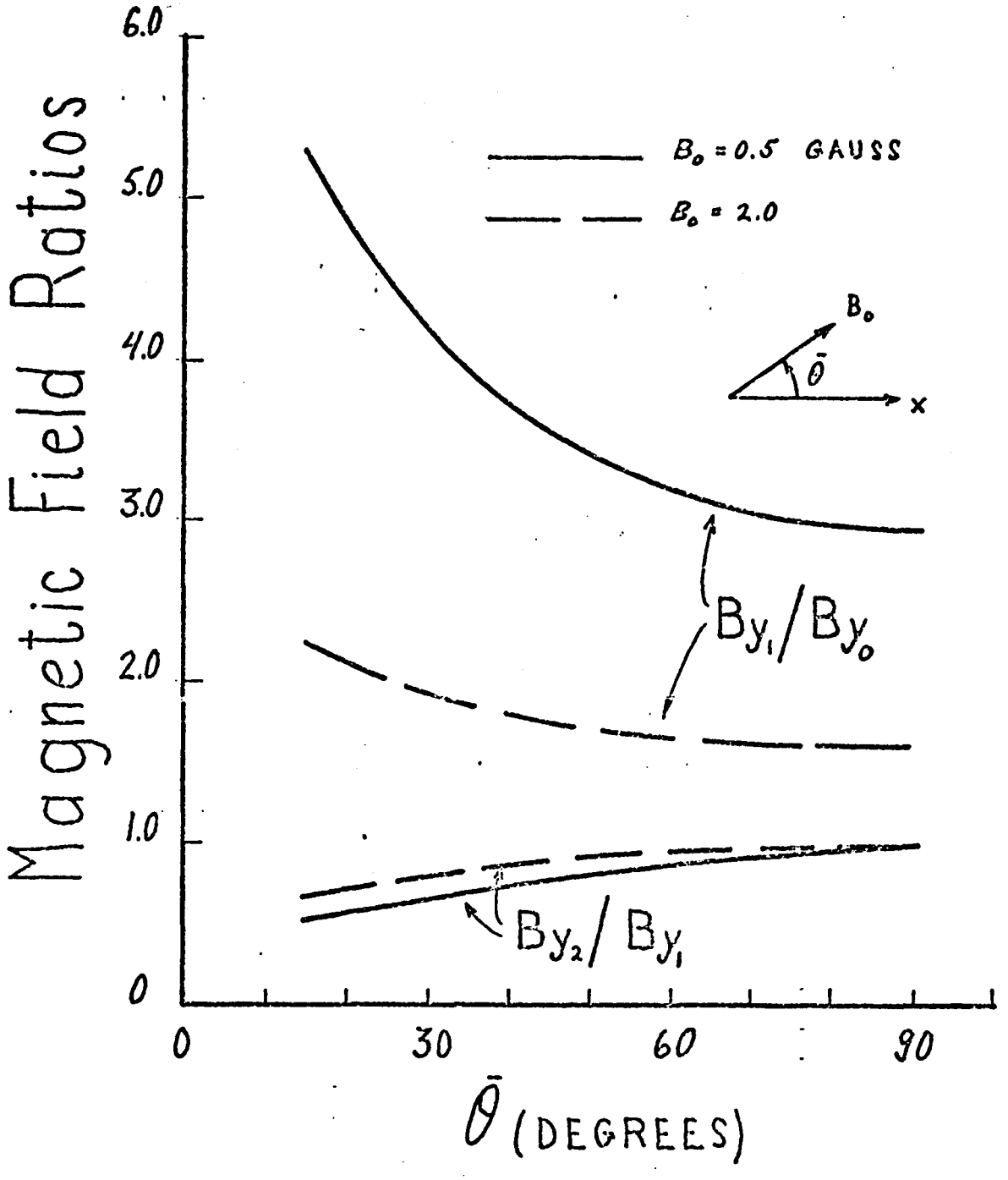

Fig. 3.3 Tangential magnetic field jumps across shocks vs. angle of magnetic field for planar piston problem

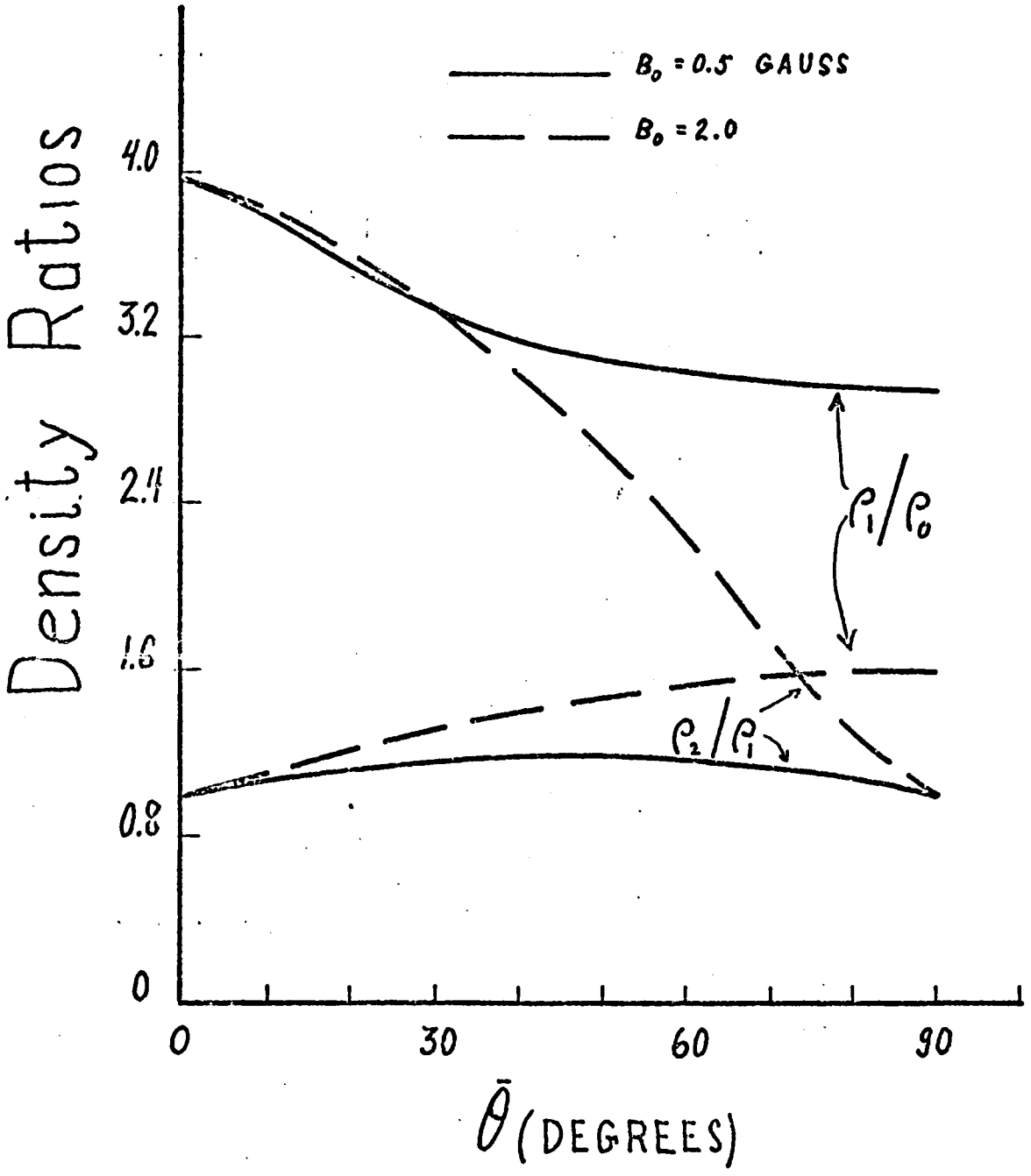

Fig. 3.4 Density jumps across shocks vs. angle of magnetic field for planar piston problem

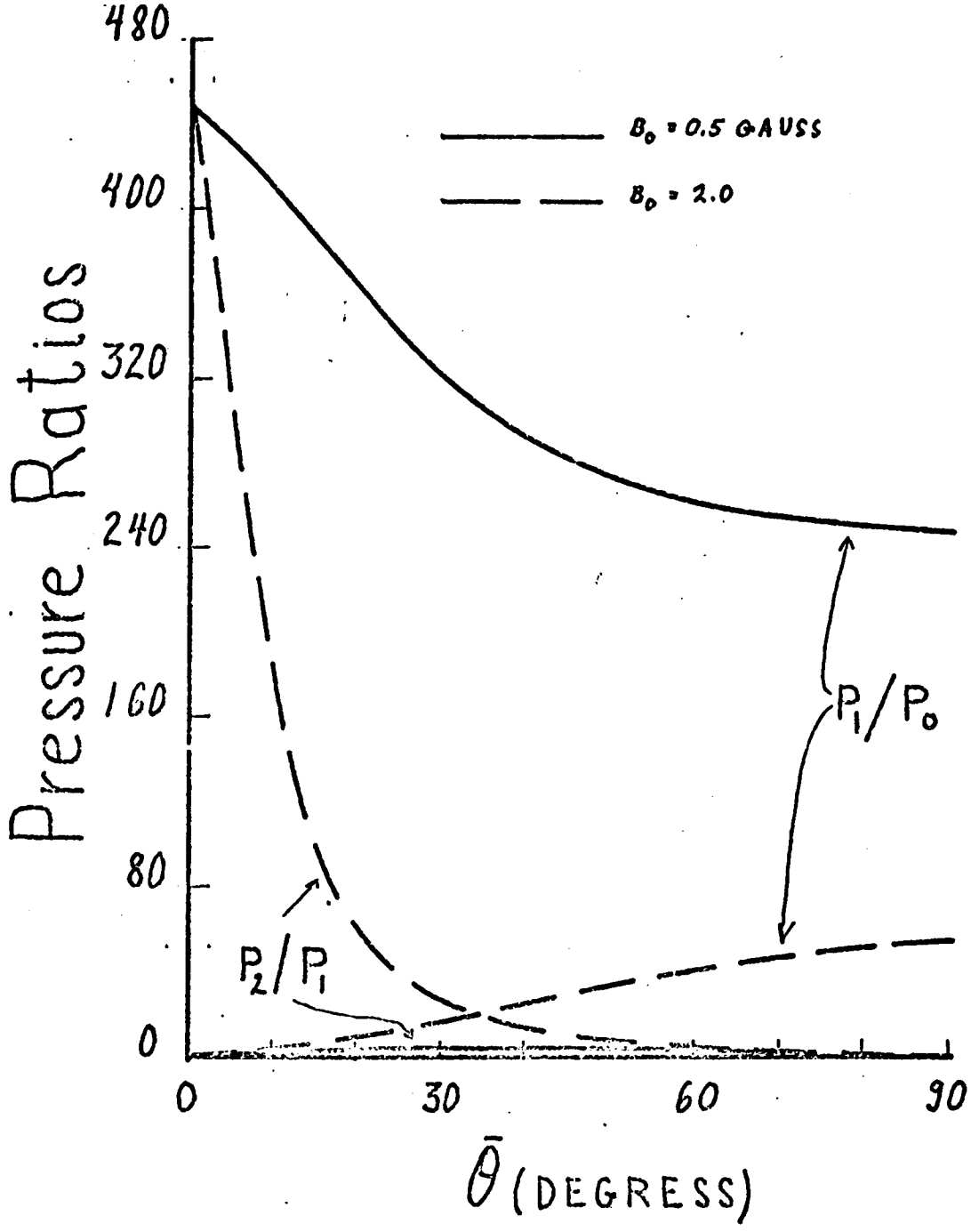

Fig. 3.5 Pressure jumps across shocks vs. angle of magnetic field for planar piston problem

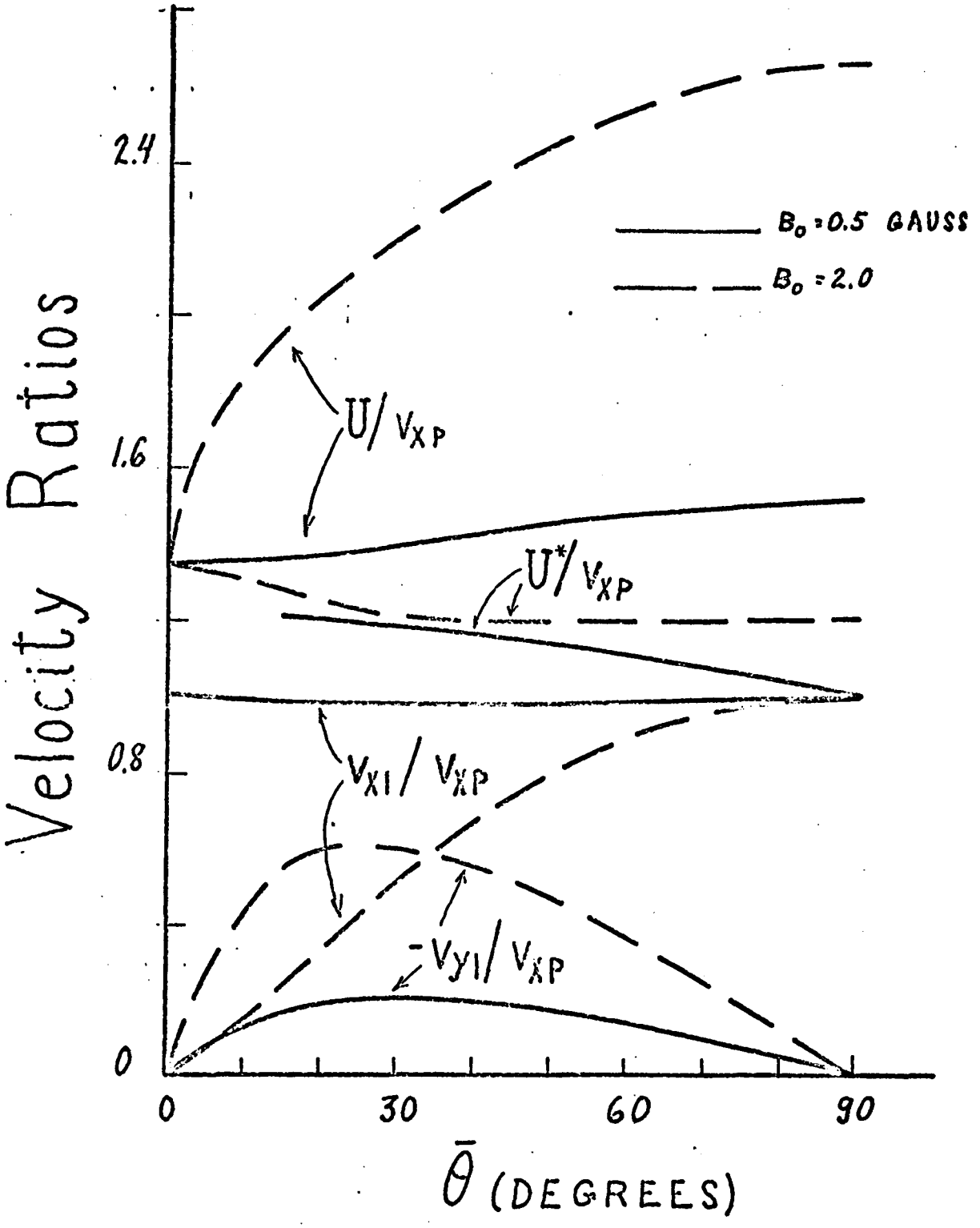

Fig. 3.6 Shock and particle velocities vs. angle of magnetic field for planar piston problem

field angle $\bar{\theta}$. Figure 3.3 gives the ratio of the transverse field in the post shock state to that in the preshock state for both fast and slow shocks, Figure 3.4 gives the density ratios, Figure 3.5, the pressure ratios, and Figure 3.6, the shock speeds and velocity components as ratios to the piston speed.

The more important results pertain to the fast shock. For a given $\bar{\theta}$, as B_o is increased, B_{y_1}/B_{y_o}, by definition greater than one for a fast shock, decreases, as do ρ_1/ρ_o and p_1/p_o. The fast shock speed, U, of course increases. For a given B_o, as $\bar{\theta}$ is increased, the shock speed increases as B_{y_1}/B_{y_o} decreases, but the ratios p_1/p_o, ρ_1/ρ_o, the so called gasdynamic strength, decrease only for superalfvenic piston speeds; for subalfvenic speeds (B_o = 2.0 gauss) they increase. Define $f_{m_1} = B_{y_1}/B_{y_o}$ as the shock strength of the fast MHD shock as distinguished from the gasdynamic strength. Then, as f_{m_1} decreases, either as B_o or $\bar{\theta}$ increases, the shock speed increases. This agrees well with the hypothesis given previously, that a strong shock travels slower than a weak one.

The change in variation of the gasdynamic strength with $\bar{\theta}$ as the piston becomes subalfvenic can be explained with the use of the Friedrichs diagram. For superalfvenic pistons (B_o = 0.5 gauss), the shock may be labeled type A, corresponding to Figure 1.1a. For type A shocks, for $\bar{\theta}$ = 0, the fast shock is gasdynamic and uncoupled from the magnetic effects. As $\bar{\theta}$ increases, the magnetic effects become more and

more coupled to the fast shock, thus reducing the gasdynamic strength. For subalfvenic pistons (B_o = 2.0 gauss), the shock is labeled type B, corresponding to Figure 1.1b. For small $\bar{\theta}$, the type B fast shock is almost wholly magnetic and the gasdynamic strength is negligible. As $\bar{\theta}$ increases, the gasdynamic effects become coupled to the type B shock, and therefore the gasdynamic strength increases slightly with $\bar{\theta}$. This significant difference between type A and type B shocks can be seen in Figures 3.4 and 3.5. As $\bar{\theta}$ approaches zero, p_1/p_o and ρ_1/ρ_o approach the gasdynamic values for type A shocks, but approach a continuous transition for type B shocks. In addition, type B shocks are characterized by large transverse velocities, especially for small $\bar{\theta}$, as seen in Figure 3.6. Only for type A shocks, where the gasdynamic strength is dominant, does the gasdynamic strength vary as the fast shock strength f_{m_1}.

Since the state in front of the slow shock is the fast shock post-shock state, and therefore not constant, it is difficult to make an analysis similar to the above. It can be seen from the results that the slow shock strength, $f_{m_2} = B_{y_2}/B_{y_1}$, by definition less than one, and the slow shock speed, U*, change very little with B_o. For type A fast shocks, (B_o = 0.5 gauss) the corresponding slow shock has extremely weak density and pressure jumps, but for the basically magnetic type B fast shocks (B_o = 2.0 gauss) for low $\bar{\theta}$, the slow shock necessarily has large gasdynamic strength.

Extending these results to the spherical problem, the fast shock should be elliptic with major axis corresponding to $\bar{\theta} = 90^{o}$. Shock density and pressure should decrease as magnetic field is increased while shock speed should increase. A change in the variations of pressure and density with $\bar{\theta}$ may be expected to occur as magnetic field is increased. Predictions regarding the slow shock may not be made. For the planar problem, the slow shock is necessary to satisfy the boundary condition at the piston since simple compressive waves cannot exist[17]. For the spherical model, the discussion of simple waves and constant states simply does not apply since the governing equations are not reducible.

3.4 Summary

The problem of a planar piston pushing into an ambient MHD medium with a uniform magnetic field has been investigated in this chapter. A new theoretical piston solution has been presented. This solution was compared to numerical solutions obtained using the two computer programs, resulting in agreement to better than one percent for all problems studied. It was established that the computer solutions are stable and convergent.

MHD WUNDY was used to study the development of a switch-on shock due to a transverse motion of the piston. It was found that the fast shock is a gasdynamic shock for superalfvenic piston motions and a switch-on shock for subalfvenic motions. Planar piston solutions were presented for different orientations and magnitudes of magnetic fields to qualitatively predict the results of the spherical piston problem. The resulting fast shocks were classified as type A, strongly gasdynamic, and type B, primarily magnetic, and the properties of each were examined.

CHAPTER 4

THE SPHERICAL MHD PISTON PROBLEM

The expansion of a rigid, infinitely conducting, spherical piston into an ambient, infinitely conducting, nondissipative MHD medium with a uniform magnetic field is studied here for constant piston speed, $v_{rp} = 10^8$ cm/sec. and for ambient data corresponding to an altitude of 200 km, given by (2.7). The new solution, obtained using MHD CYCLONE, is the first solution which is valid for all magnitudes of magnetic field. This solution is compared with the existing numerical solutions, valid for very small or very large magnetic field, reviewed in Chapter 1. Numerical results, obtained using the rezoning scheme described in Chapter 2 to remove distortions in the Lagrangian mesh due to the motion of the fluid, are compared to results without rezoning to show the value of this rezoning scheme.

4.1 Comparisons with Existing Solutions

Numerical solutions to the spherical piston problem are compared with the gasdynamic solution due to Taylor[10], the solution for very small magnetic fields ($b_o \ll v_{rp}$) due to Kulsrud et al[11], and the solution for very large magnetic fields ($b_o \gg v_{rp}$) due to Bernstein and Kulsrud[12].

(a) The Spherical Gasdynamic Piston Problem:

A solution may be obtained directly using either MHD WUNDY or CYCLONE. MHD CYCLONE requires that the piston be given an initial radius, chosen as $r_o = 500$ cm, rather than starting its motion from a point in space. The solution obtained from CYCLONE, (WUNDY gives excellent agreement), is shown in Figure 4.1 for $t = 2.0 \times 10^{-3}$ sec. At this time, the piston has increased its radius five times so that the solution should approximate the similarity solution that would have been obtained if the piston initially had zero radius. In fact, a ten percent increase in time results in a less than one percent change in shock and piston pressures, giving about a similarity solution.

Magnitudes of shock density, pressure, and radial velocity are taken from Figure 4.1 at the points where the slopes of curves change radically. This is the best estimate possible as there is no region of constant state behind the shock and the shock has been flattened out by the artificial viscosity. The shock speed is determined as the rate of change with time of the position of the maximum value of artificial viscosity in the shock and was found to be constant with time. The

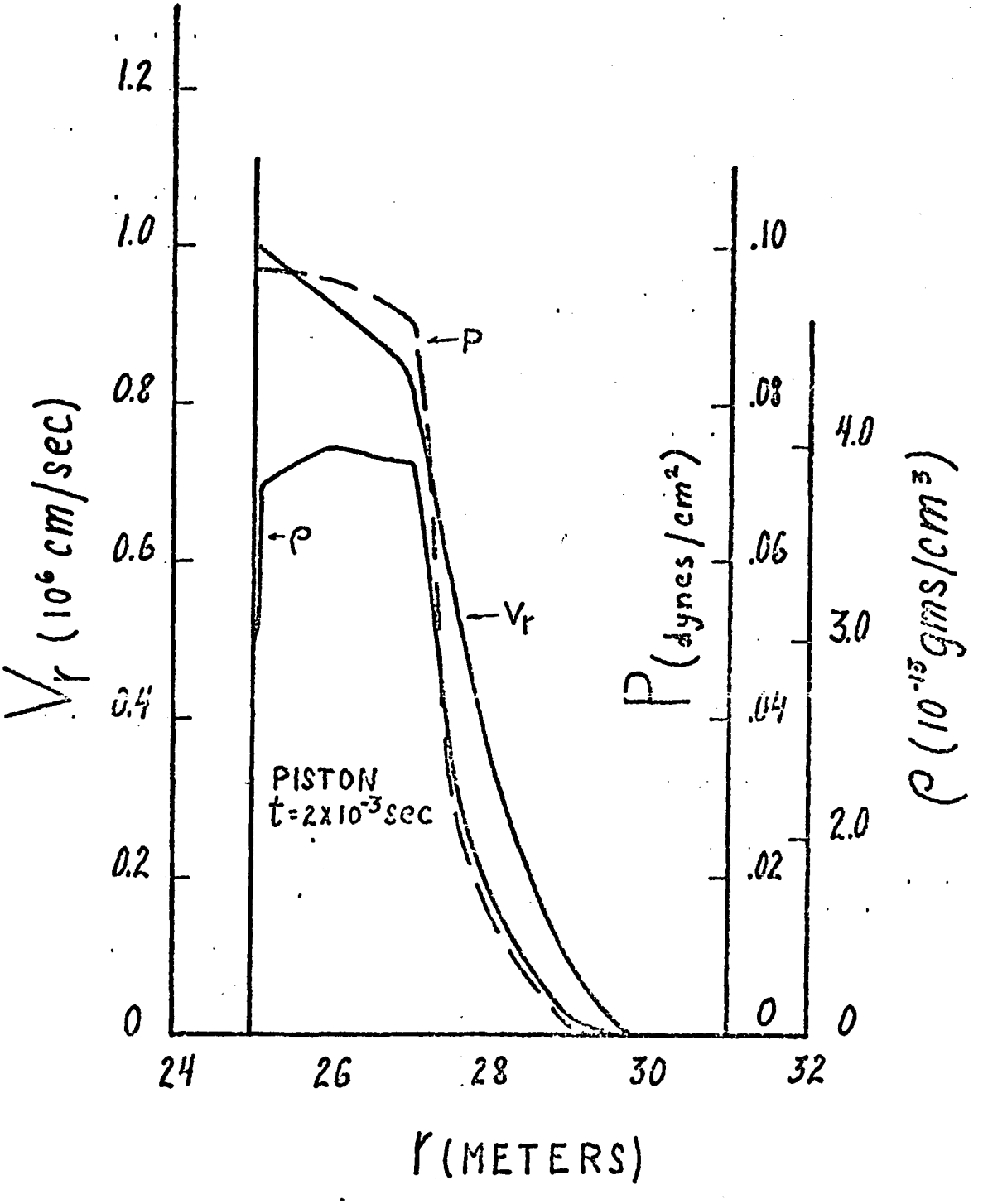

Fig. 4.1 Radial velocity, pressure, and density vs. radius ($t = 2.0 \times 10^{-3}$ sec) for spherical gasdynamic piston problem

spherical shock results, written as dimensionless ratios are:

shock speed U/v_{rp}	= 1.095
density ρ_1/ρ_o	= 3.90
pressure p_1/p_o	= 300
particle velocity v_{r_1}/v_{rp}	= 0.86

These results show a weaker shock than the planar piston results of Table 3.1 for the same ambient data. This is in general true for spherical problems. The computer solution was checked with the Rankine-Hugoniot shock solutions, equations (B1) - (B3) of Appendix B.

Since the computer results satisfy both the shock conditions and the boundary conditions at the piston, give similarity solutions, and the curves of Figure 4.1 have similar shapes to the numerical solution of Taylor, it can be stated that the MHD CYCLONE solution for the gas-dynamic problem is correct.

The gasdynamic solution was used to empirically determine the minimum value of the coefficient of artificial viscosity, $\bar{a}$, which would successfully damp out oscillations at the shock wave. Since the artificial viscosity, given by equation (2.29), is proportional to the square of the velocity gradient, and significant velocity gradients may be present in the region behind the shock, (velocity gradients are zero in this region for slab symmetry), it is important that $\bar{a}$ be minimized so that the fluid corresponds as closely as possible to the nondissipative

model[3]. It was found that this minimum value of $\bar{a}$ depended upon the mesh width Δr, a smaller Δr requiring a larger $\bar{a}$. To reduce machine time, it was decided to use $\Delta r = 100$ cm with a corresponding value $\bar{a} = 2.0$; along with the mesh widths $\Delta\theta = 6^{o}$, in obtaining all the solutions in this chapter. Cutting the mesh widths in half causes no significant changes in the results.

(b) The Solution for Small Magnetic Fields:

A solution is obtained using MHD CYCLONE for a uniform magnetic field, $B_o = 0.25$ gauss, corresponding to an expansion parameter, $\epsilon = b_o/v_{rp} = 0.22$. Figure 4.2 is a sketch of the results showing the curvature of the initially uniform magnetic field lines behind the shock. At the equator ($\theta = 90^{o}$), the compression of magnetic field lines behind the shock increases the magnetic pressure so that the total pressure, $p + p_m$ is greater than in the gasdynamic case, resulting here in a 6 percent greater shock speed. At the pole, however, the curvature of the field lines results in an inward magnetic force which slows down the shock slightly (0.5 percent). This can be thought of as the shock giving up energy to the magnetic field in order to push aside the field lines near the pole. The tangential magnetic field B_θ, increases in magnitude behind this elliptic shock, so that, by definition, it is a fast shock.

Since the computer calculation cannot be initialized with a piston of zero radius, the boundary condition specified by Kulsrud et al[11], that the radial component of magnetic field at the piston, B_{rp}, is zero, is

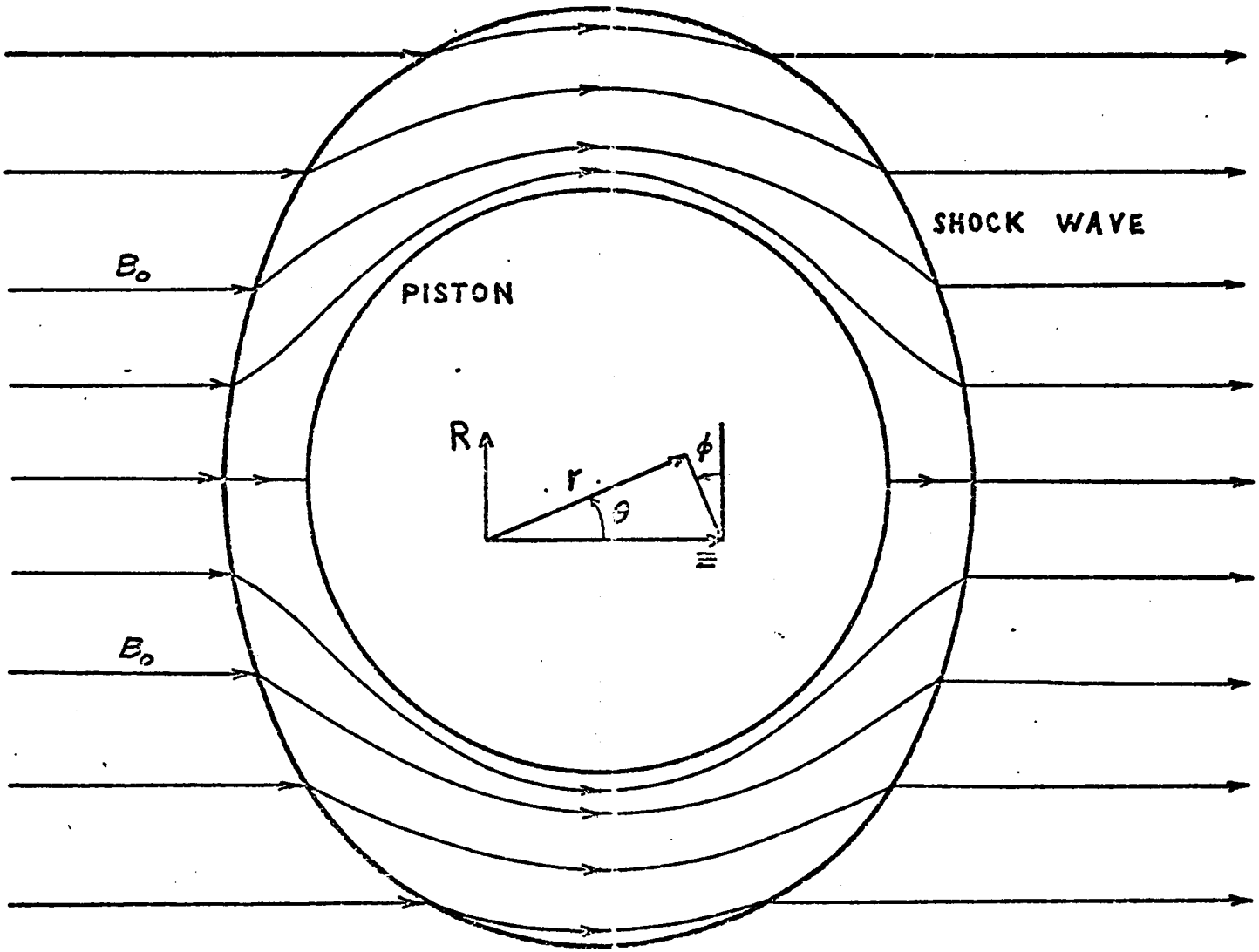

Fig. 4.2 Shock wave and magnetic field configuration for spherical piston problem

not satisfied initially by the uniform magnetic field. However, the results show this boundary condition to be satisfied at later times within a mesh width of the piston.

Kulsrud et al were unable to obtain a solution in the magnetic boundry layer surrounding the piston. The computer solution presented here included this boundary layer. Figure 4.3 gives the pressure profiles at angles of 30^{o} and 90^{o} to the pole for different times. Outside of the boundary layer, the solution is basically a similarity solution. Once the shock forms completely, the disturbed region simply widens with very little change in shock pressure. Shock pressure decreases as θ increases and the curves are similar in shape to the results of Kulsrud. Note that while the gasdynamic results, Figure 4.1, show a continual increase in pressure behind the shock, Figure 4.3 shows a decrease in pressure. However, if the total pressure, material plus magnetic, is considered, the curves have shapes similar to Figure 4.1. In the boundary layer, the pressure decreases with time. This is balanced by the increase in magnetic pressure due to the increase in flux with time near the piston.

Density curves are very similar to the pressure curves and in good agreement with Kulsrud results showing a decrease in density as θ is increased. The curve for $\theta = 0^{o}$ is almost identical with the gas-dynamic result, Figure 4.1. Variations in magnetic field with position are shown in Figure 4.4 while velocity components are given in Figure 4.5 both for a time $t = 2.0 \times 10^{-3}$ sec. Magnitudes at the shock are constant

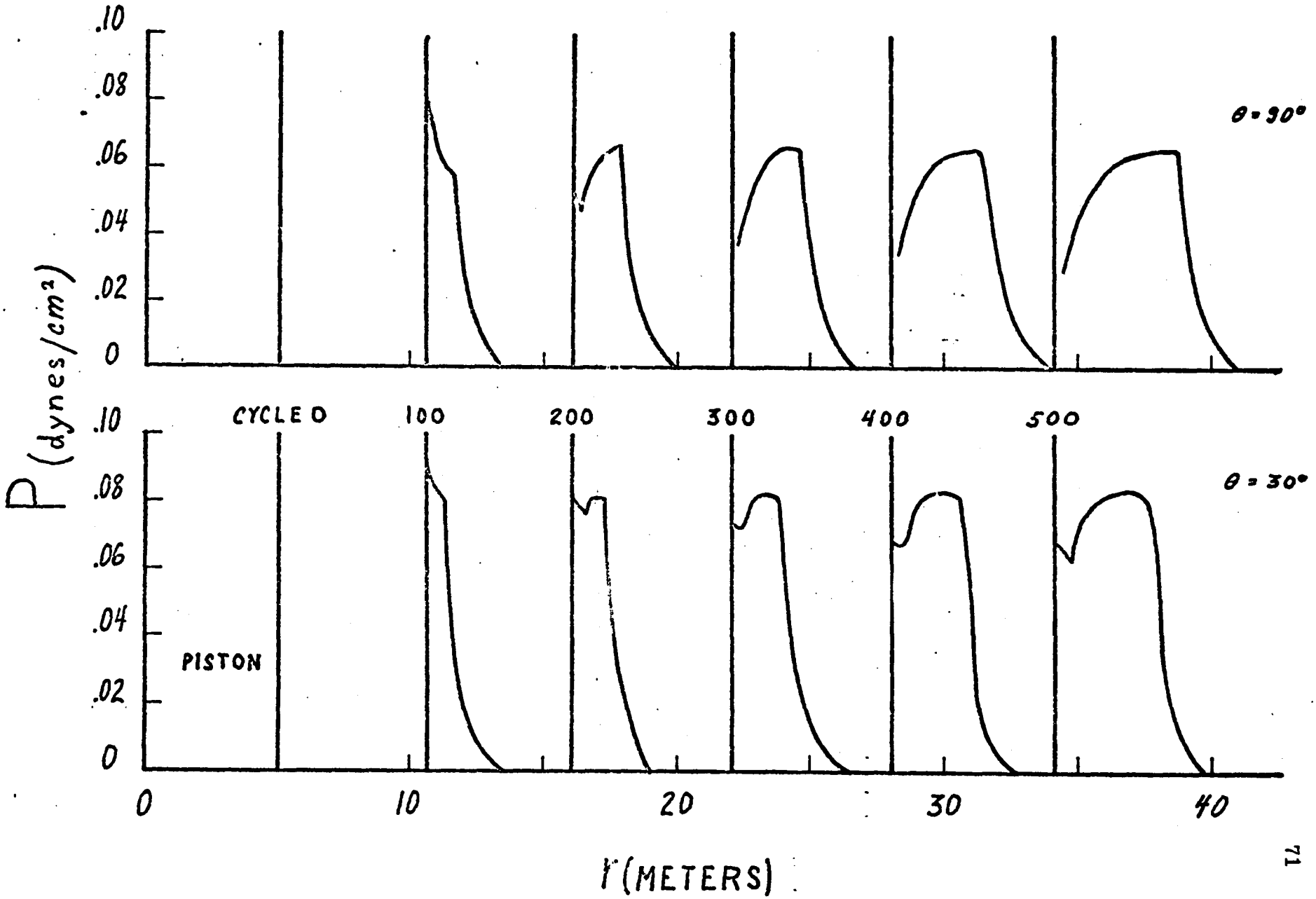

Fig. 4.3 Pressure vs. radius (B_o = 0.25 gauss) at different times for spherical piston problem

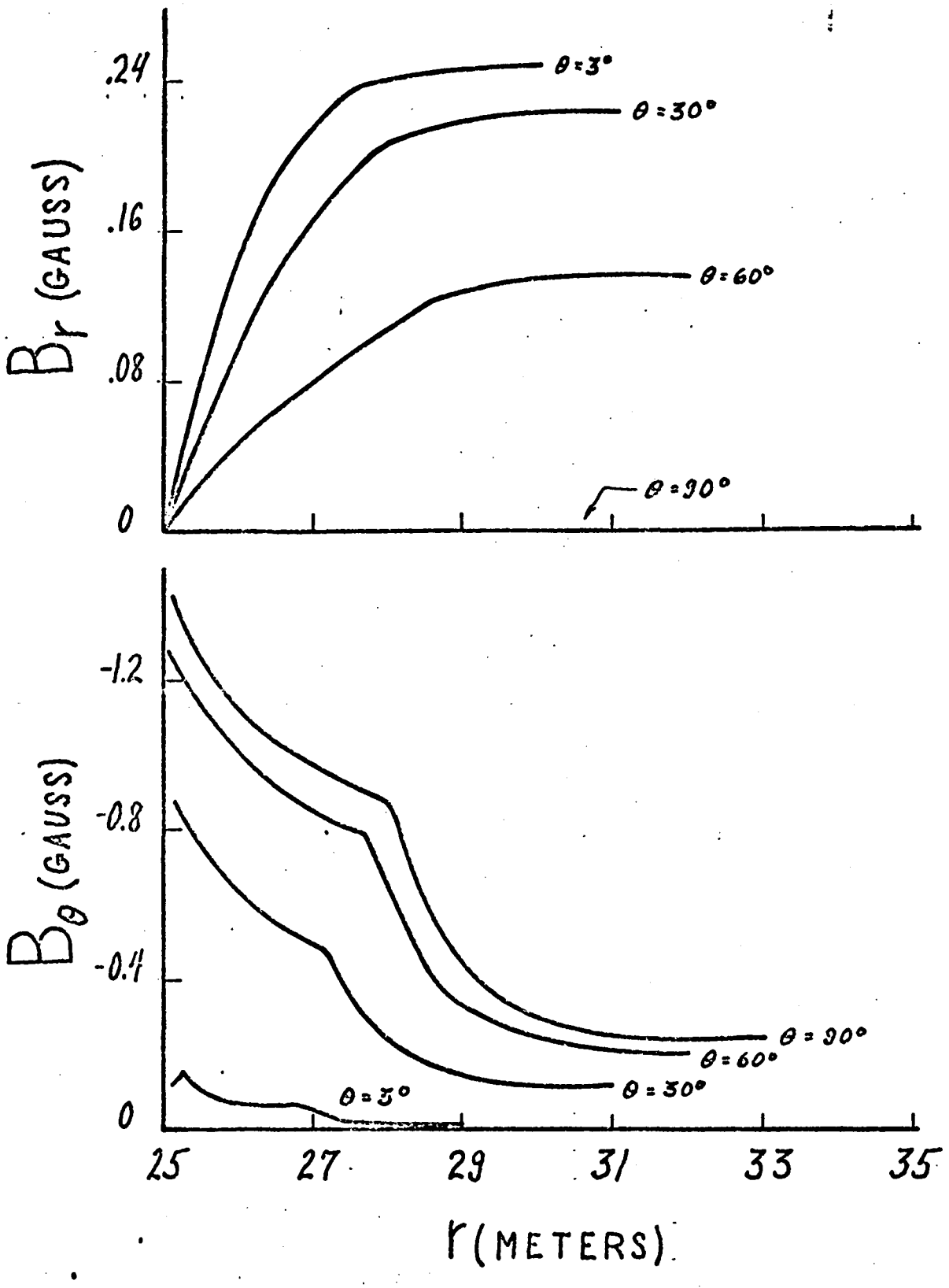

Fig. 4.4 Magnetic field components vs. radius (B_o = 0.25 gauss, $t = 2.0 \times 10^{-3}$ sec) for spherical piston problem

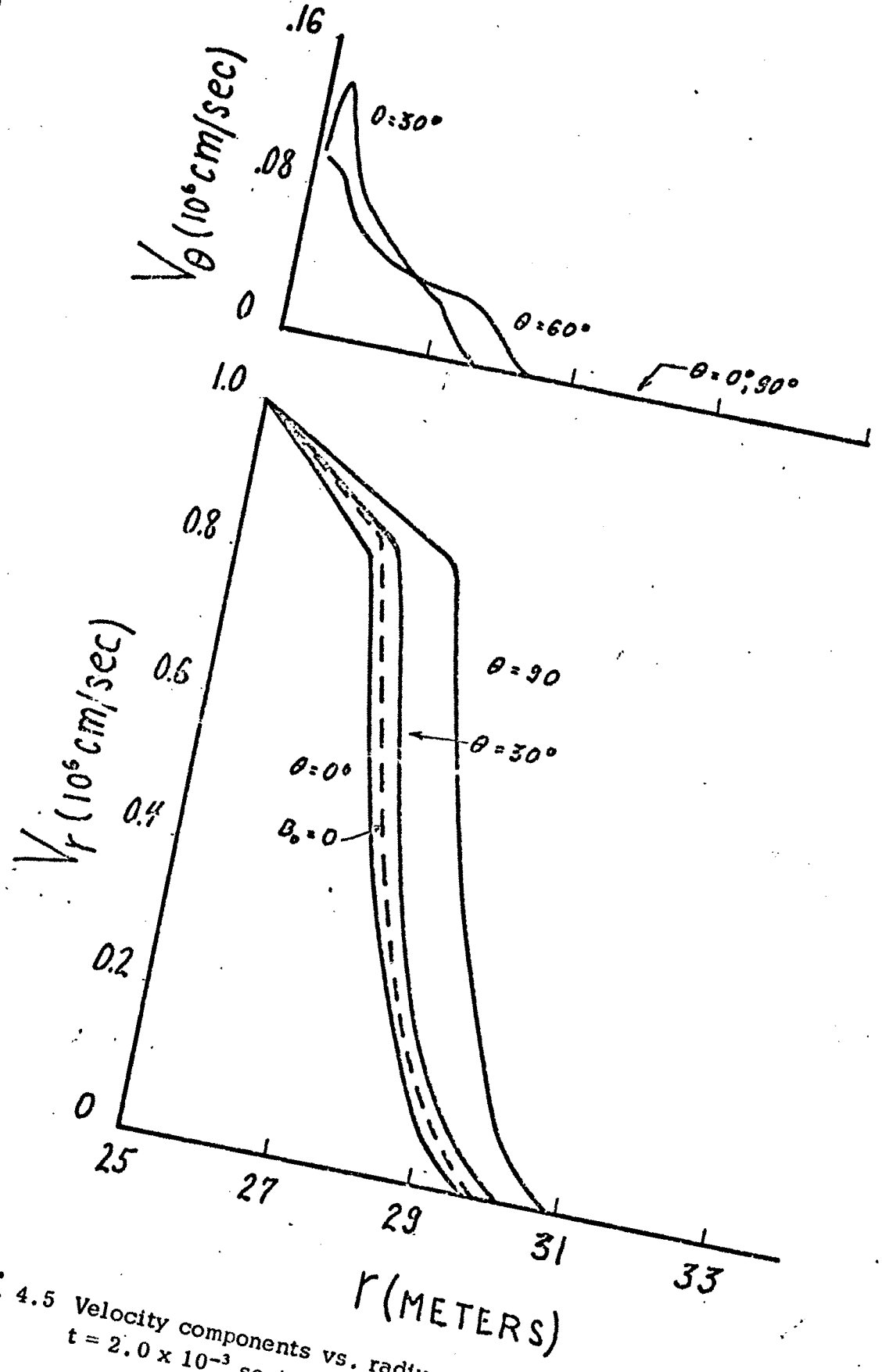

Fig. 4.5 Velocity components vs. radius (B_o = 0.25 gauss, $t = 2.0 \times 10^{-3}$ sec) for spherical piston problem

with time but the value of B_θ in the boundary layer increases with time, especially at higher θ. The gasdynamic result is superimposed on Figure 4.5 to show that radial velocity is increased by the magnetic field for θ greater than about 20^o and decreased for smaller θ.

Away from the piston, the numerical solution is in good agreement with the Kulsrud solution. However, close to the piston, a significant difference in velocity profiles is noticed. The Kulsrud solution for θ greater than 60^o shows a maximum value of radial velocity greater than v_{rp}, the expansion speed of the piston, and also claims that the tangential velocity v_θ is symmetric about $\theta = 45^o$. The computer results show that tangential velocity profiles near the piston are skewed toward the pole with a maximum at $\theta = 35^o$. This seems reasonable since, for infinite electric conductivity, the fluid moves with the magnetic field lines which, initially straight, have a larger curvature near the pole. The discrepancy in the results may be due to his lack of a boundary layer solution.

(c) <u>The Solution for Large Magnetic Fields</u>:

A solution is obtained using MHD CYCLONE for a uniform magnetic field, $B_o = 4.0$ gauss, corresponding to an expansion parameter $\epsilon' = v_{rp}/b_o = 0.28$. Figure 4.6 gives the density between the shock and the piston and Figure 4.7 shows the velocity components, both for a time $t = 1.0 \times 10^{-3}$ sec. The shock itself is extremely weak and almost spherical, and propagates at approximately b_o, the Alfven speed of the

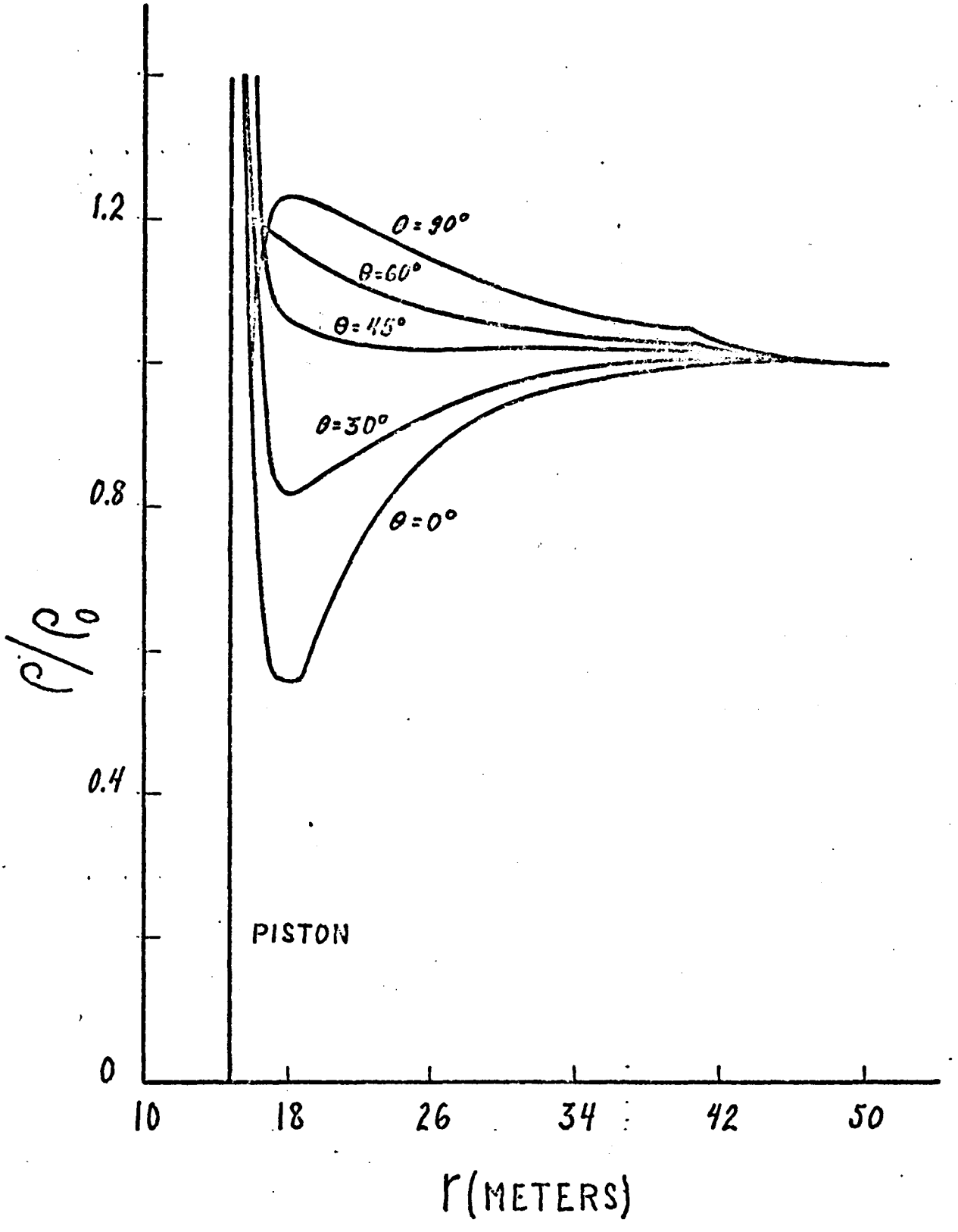

Fig. 4.6 Density vs. radius (B_o = 4.0 gauss, t = 1.0 x 10^{-3} sec) for spherical piston problem

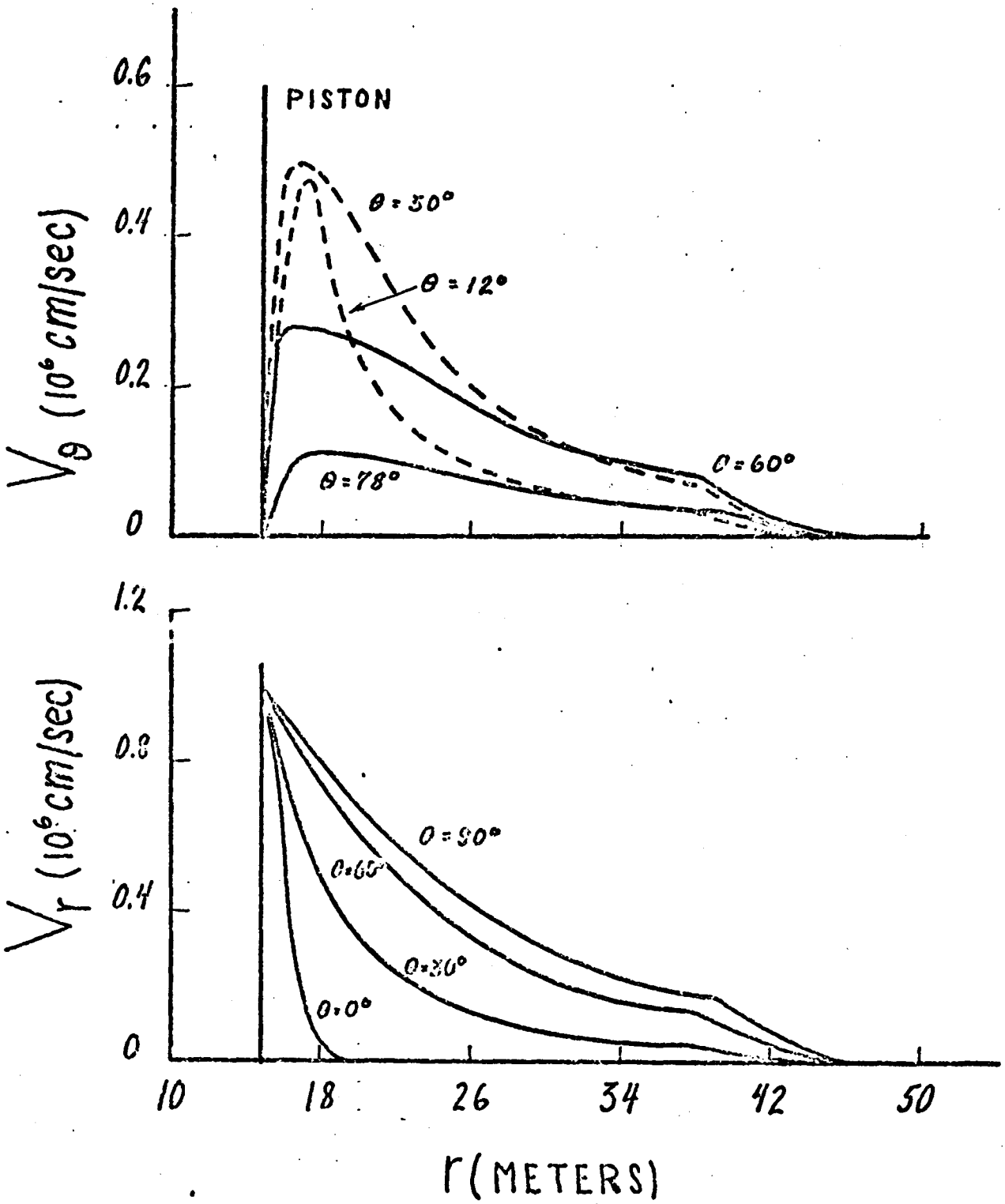

Fig. 4.7 Velocity components vs. radius (B_o = 4.0 gauss, t = 1.0 x 10^{-3} sec) for spherical piston problem

undisturbed medium.

At the equator, particles are compressed slightly as they travel from shock to piston. However, for θ less than 40^{o}, the plasma undergoes an expansion behind the shock. These results are in good agreement with the Bernstein-Kulsrud linearized solutions in the far region (the region away from the piston). In the near region, the plasma is highly compressed near the pole.

Radial velocity is zero at the pole in the far region and increases with θ. In the near region, v_r must increase to satisfy the boundary conditions at the piston. Tangential velocity is symmetric about $\theta = 45^{o}$ in the far region (r greater than 30 meters in Figure 4.7) and skewed toward the pole in the near region, the maximum occurring at $\theta = 24^{o}$. Material pressure is much less than magnetic pressure and varies in a manner similar to density. No significant differences exist between this solution and the solution of Bernstein and Kulsrud.

4.2 Rezoning

The spherical piston results described in the previous section, for the limits of very small and very large magnetic fields, were obtained from CYCLONE using the rezoning scheme outlined in Section 2.3 to eliminate errors due to distortions in the Lagrangian mesh caused by the motion of the fluid[2]. To show the necessity of rezoning, computer runs were made both with and without rezoning for a uniform magnetic field of 0.5 gauss. The solid curves in Figure 4.8 show the distorted positions of mesh points between the piston and the shock at times, $t = 1.2 \times 10^{-3}$ sec and $t = 1.9 \times 10^{-3}$ sec, for no rezoning. Initially, mesh points lie on constant θ lines, K = constant, $\Delta\theta = 6$ degrees apart. Distortion is zero at the equator (K = 17) and the pole (K = 2) and is a maximum near the piston at about $\theta = 30^{\circ}$ (K = 7). Since the equations give a similarity solution, the tangential velocity is basically constant with time, so that the distortion of a mesh point in the θ direction, $v_{\theta}t$, increases linearly with time.

Radial particle velocity curves are qualitatively similar to Figure 4.5. Since the particle velocity is less than the piston speed, the initial Lagrangian zones, $\Delta r = 100$ cm, are compressed and tend to pile up at the piston. This is especially true near the pole, where the magnitudes of radial velocity gradients are larger. At cycle 200, $t = 1.2 \times 10^{-3}$ sec., zones near the piston are compressed to about 3 cm. at the pole and 15 cm. at the equator; by cycle 650, $t = 1.9 \times 10^{-3}$ sec.,

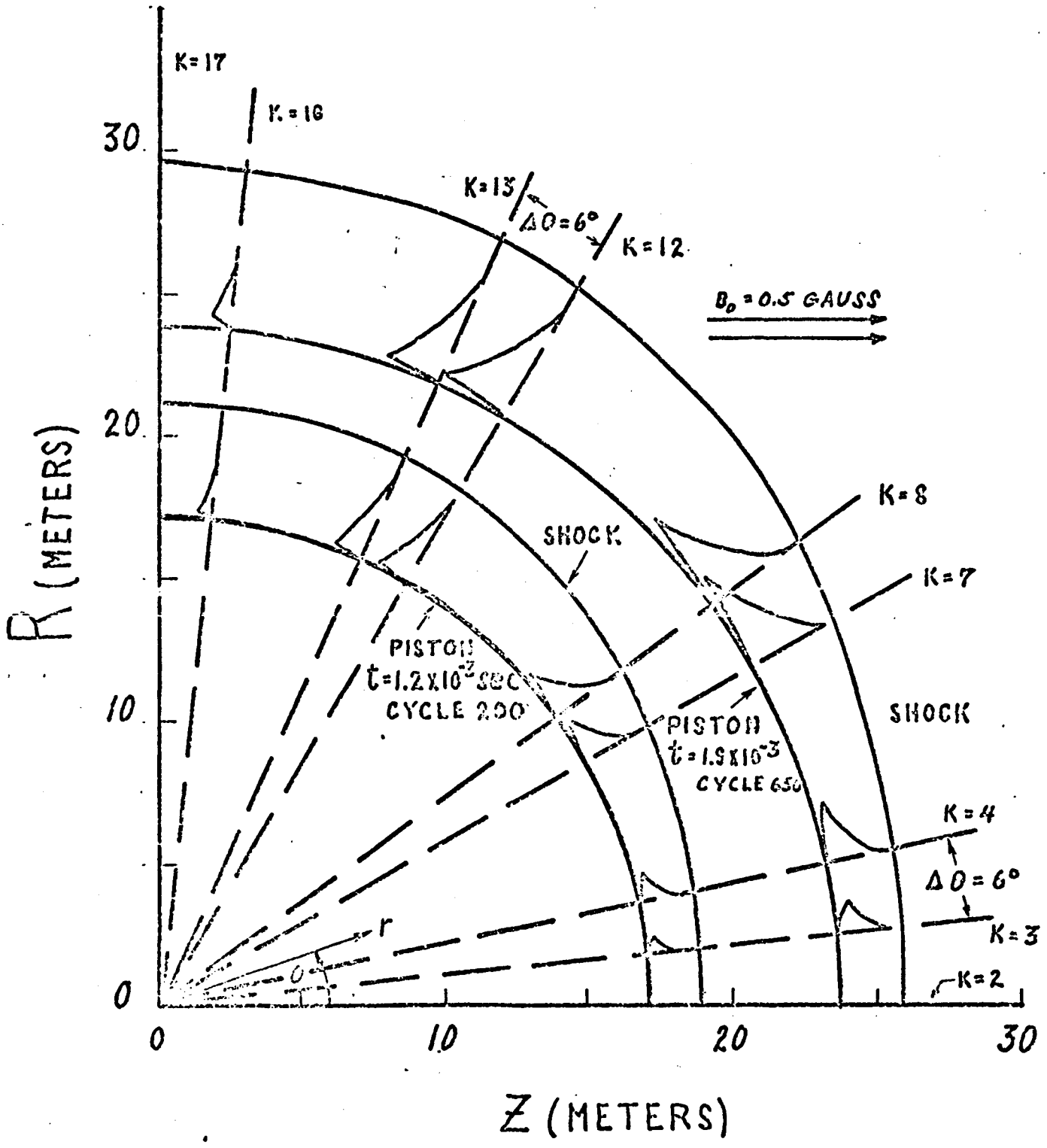

Fig. 4.8 Distortion of Lagrangian mesh between piston and shock

zones are as small as 1 cm. at the pole and 10 cm. at the equator.

Figure 4.9 shows the variation in pressure with radius along different mesh lines, K = constant, for the magnetic field of 0.5 gauss and no rezoning at cycles 200 and 650. At K = 4, an oscillation in pressure near the piston, not present at larger angles, is clearly visible in Figure 4.9 at the earlier time, $t = 1.2 \times 10^{-3}$ sec., and is seen to grow with time. This oscillation is not the classic instability due to too large a time step and was present even when the time step was cut in two. Decreasing $\Delta\theta$ from 6 to 3 degrees did not eliminate the oscillation.

The oscillation occurs in the region of largest radial compression of zones as well as significant tangential distortions. In this region, zones are compressed to less than 1/30 their original size which necessarily causes errors in the differencing of radial derivatives. A rezoning scheme, described in Section 2.3, was developed to eliminate these errors. The first stage of this scheme is to restore all mesh points to their initial constant θ lines using linear interpolation. This has the advantage of allowing the results to be easily presented for constant θ as well as eliminating the tangential distortions. The radial rezoning scheme now combines a crushed zone with its radial neighbor conserving the mass and total energy of the pair of zones. As explained, the whole row of zones, K = 2 to K = 17, having initially the same radial coordinate, must be combined with their radial neighbors as well, in order to maintain the differencing scheme.

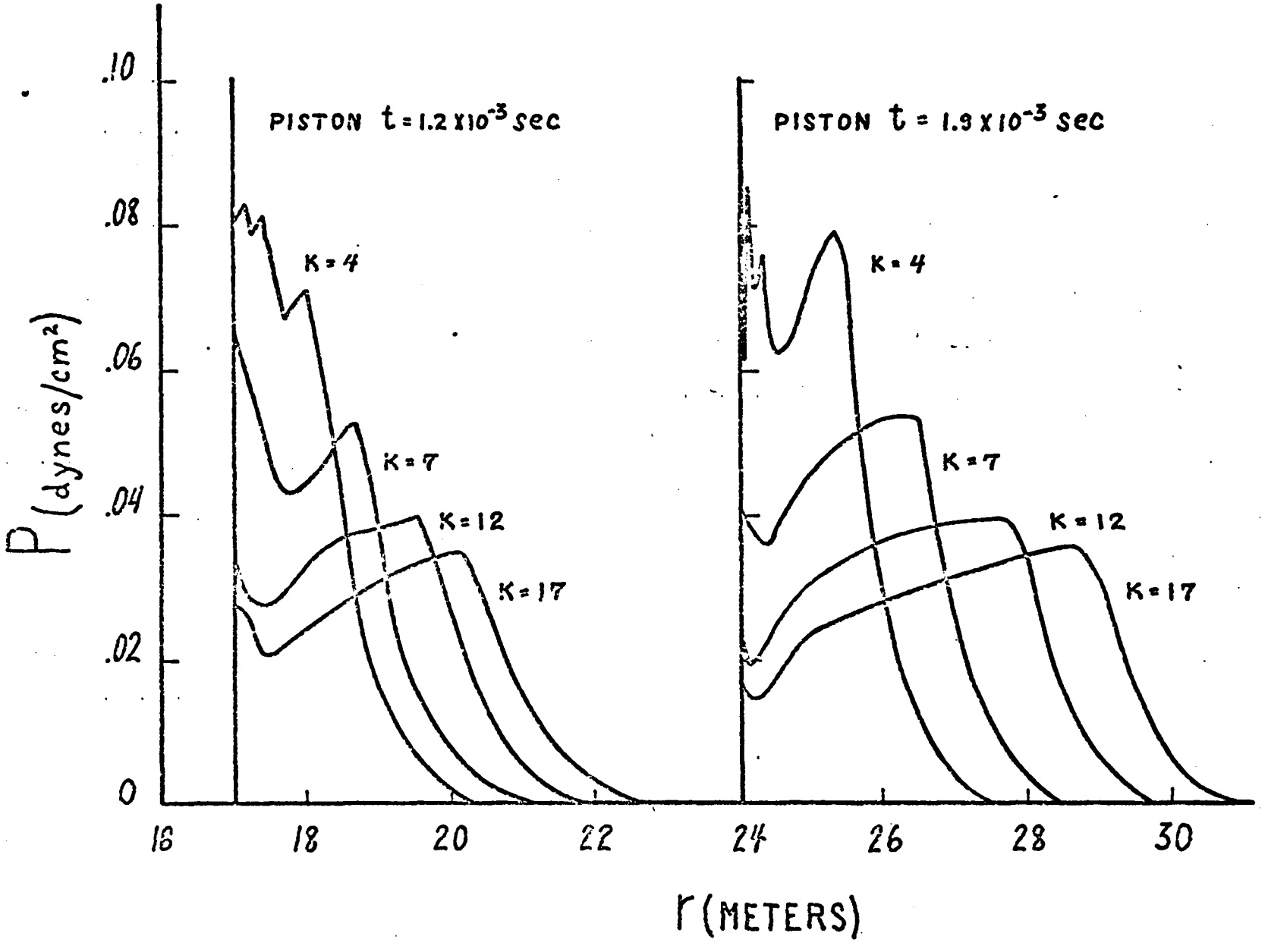

Fig. 4.9 Pressure vs. radius (B_o = 0.5 gauss, no rezoning) for spherical piston problem

Radial rezoning is only necessary in the region near the piston since Δr remains sufficiently large near the shock. The procedure followed is to seek out zones behind the shock smaller than a specified minimum for the particular problem and combine these as described. For the ambient data given by (2.7), a satisfactory minimum was found to be 10 to 20 percent of the initial Δr depending upon the ambient magnetic field, larger magnetic fields requiring larger minimum zone sizes. This rezoning is in general initiated at cycle 100, before the oscillation appears. The radial rezoning scheme may be easily modified to combine three or more radial neighbors into one large zone, but this was not found to be necessary.

Figure 4.10 shows the pressure for radial rezoning drawn alongside results for θ rezoning only, at the same time, $t = 1.7 \times 10^{-3}$ sec. The minimum allowable Δr was specified as 10 cm (10 percent of the initial Δr) and θ rezoning was executed every 50 cycles. Both sets of results showed almost no change in shock pressure from the results with no rezoning. By itself, θ rezoning does not eliminate the oscillation, but it does reduce its amplitude by about 50 percent. The application of radial rezoning eliminates the oscillation while leaving the solution unchanged.

A result of the use of rezoning, perhaps more important than the elimination of the oscillation, is the increase in efficiency of the calculation. For no rezoning, the time step needed for stability, given by

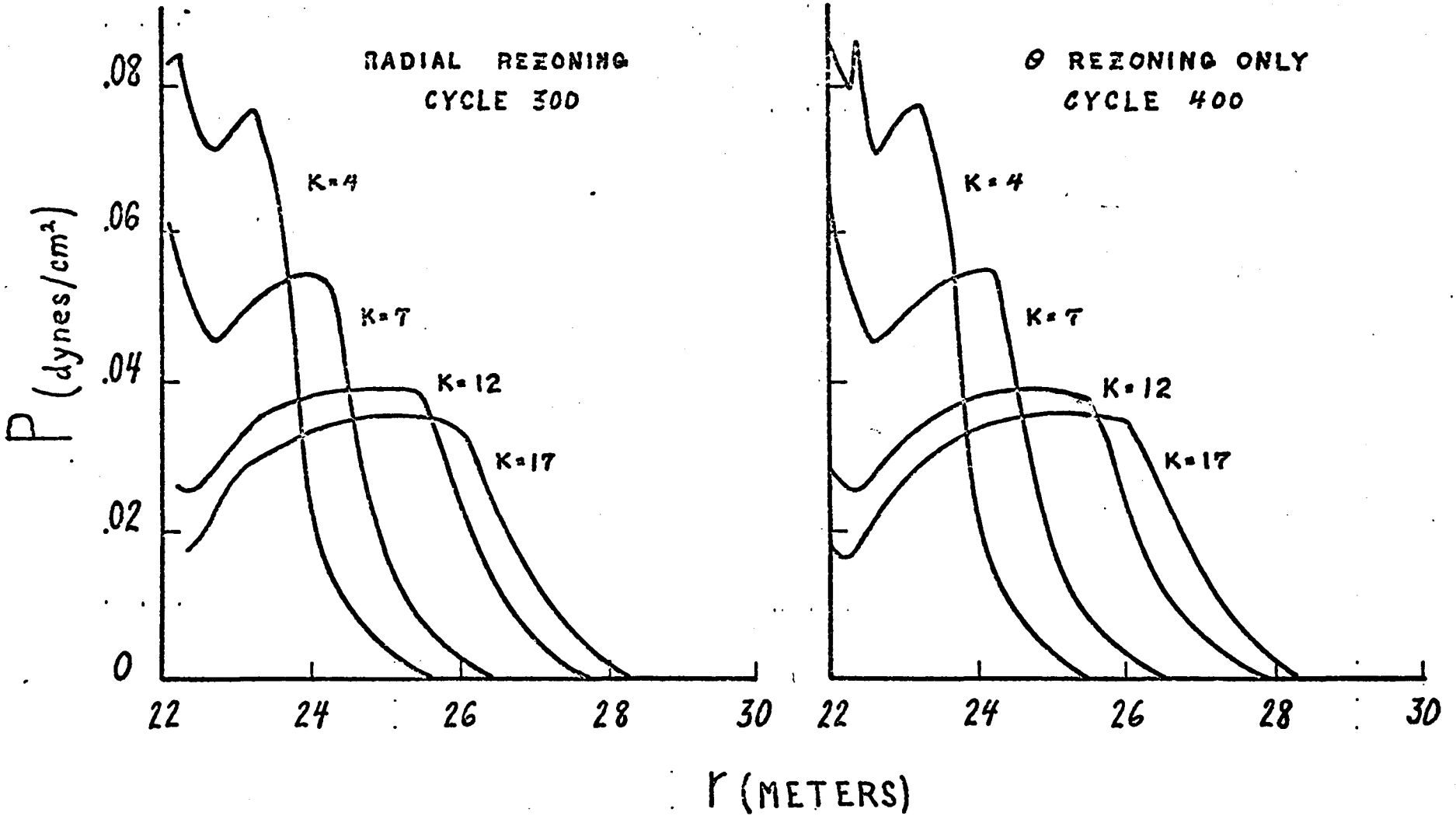

Fig. 4.10 Pressure vs. radius (B_o = 0.5 gauss, t = 1.70 x 10^{-3} sec) showing effect of radial rezoning

equations (2.66) and (2.68), decreases drastically as time increases, since Δr becomes smaller and smaller near the piston. Radial rezoning, by increasing Δr, maintains a larger time step. In Figure 4.10, the results at $t = 1.700 \times 10^{-3}$ sec. were obtained in 300 cycles using radial rezoning and 400 cycles without it, a large saving in computer time. Executing another 100 cycles without rezoning (an increase of more than 25 percent in computer time) is equivalent to increasing the time to only 1.735×10^{-3} sec. (an increase of about 2 percent). Contrast this with an increase of 100 cycles with radial rezoning (33 percent) which increases the time to 2.343×10^{-3} sec. (an increase of about 38 percent). Without rezoning, the program cannot give results for large time, but with rezoning, it can run indefinitely.

4.3 Spherical Piston Solutions

Solutions to the problem of a spherical piston expanding at a constant speed into a uniform magnetic field have already been discussed in Section 4.1 for the limiting cases of very small or very large magnetic field. In the range of magnetic fields where the ambient Alfven speed and the piston speed are of the same order of magnitude, the above solutions are invalid and the full nonlinear set of MHD equations, (2.16) - (2.23), must be solved. MHD CYCLONE was used to solve these equations for the given set of ambient conditions and for different magnitudes of uniform magnetic field. In this section, the results of the numerical calculations are presented, for a time, 2.0×10^{-3} sec., when the piston has expanded to five times its initial radius of 500 cm.

(a) The Main Shock Wave:

Figure 4.11 gives the mass density at the main shock, as a ratio to the ambient density, versus angle θ from the pole for different ambient magnetic fields. For small magnetic fields (B_o = 0.25 gauss), at the pole the shock density is approximately the gasdynamic strong shock value and decreases as θ increases. As the magnetic field is increased, density continually decreases and a change in the phenomena near the pole is noticed. For magnetic fields of 0.75 and 1.0 gauss, large shock densities occur near the pole, (these are shown dotted since it is difficult to determine the exact location of the shock), while for

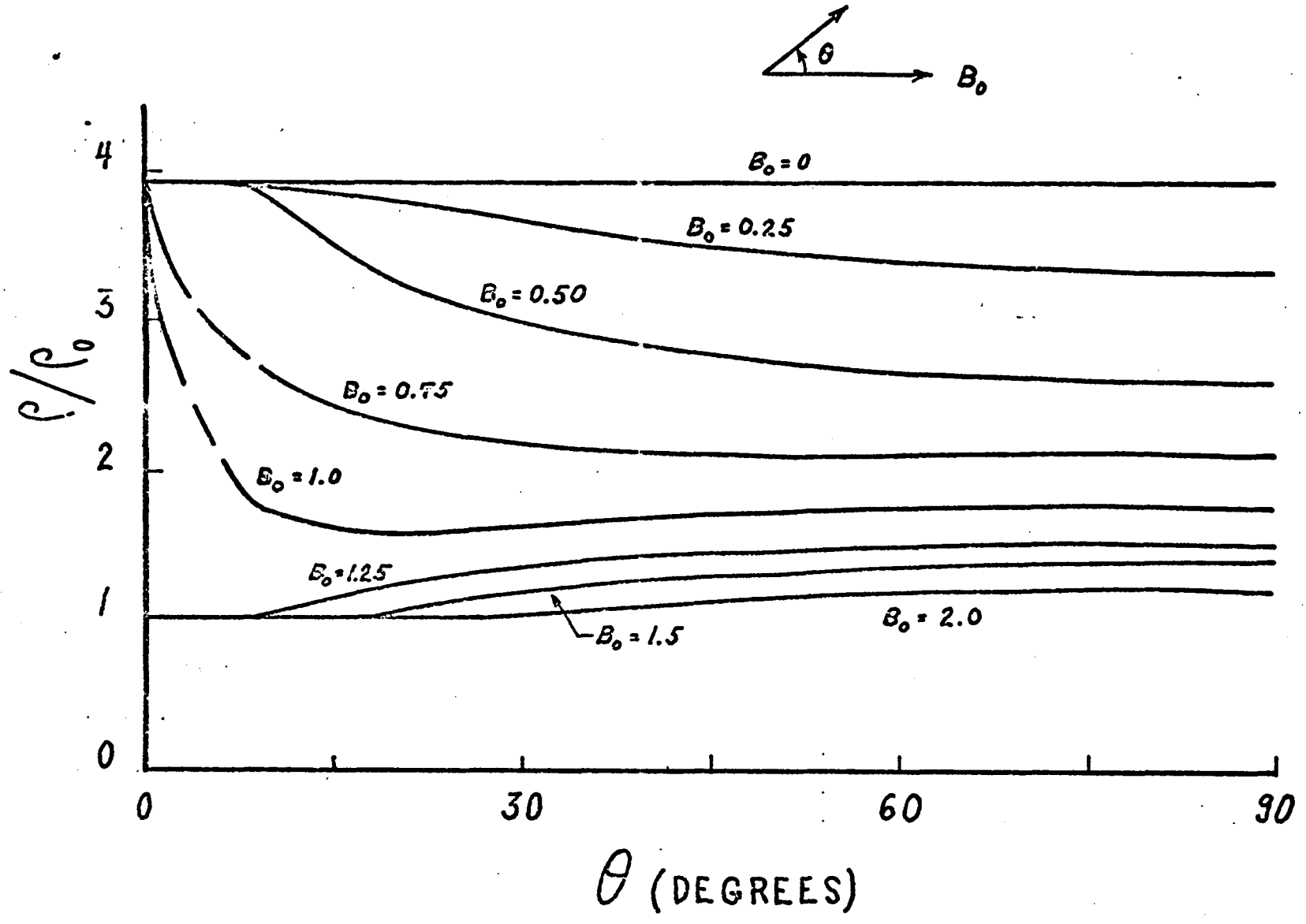

Fig. 4.11 Shock density vs. θ for spherical piston problem

larger fields, the jump in shock density near the pole is negligible. This change occurs approximately when the piston motion becomes subalfvenic, that is, when the Alfven speed of the undisturbed medium $b_o = B_o/(4\pi\rho_o)^{\frac{1}{2}}$, is greater than the piston speed v_{rp}.

Figure 4.12 shows the shock speed U, as a ratio to the piston speed, versus the uniform magnetic field for four different angles θ. For small magnetic fields, the shock speed at the equator is increased by the magnetic field from the gasdynamic value, due to the compression of magnetic field lines which results in a large magnetic pressure, $p_m = B_\theta{}^2/8\pi$, while the shock speed at the pole is decreased by the inward magnetic force due to the curvature of the field lines. These magnetic effects grow as the magnetic field is increased, resulting in an increasing elliptic shock wave until the piston becomes subalfvenic. A measure of the ellipticity of the shock may be obtained as the vertical distance between the curves for $\theta = 90^o$ and $\theta = 0^o$ in Figure 4.12. This distance is zero for no magnetic field and increases with B_o until it reaches a maximum value at the field at which the piston becomes subalfvenic. Then, the shock has negligible gasdynamic strength at the pole and propagates at the Alfven speed b_o. For larger fields, the ellipticity of the shock decreases until, for very large B_o, the shock is spherical and travels at the fast wave speed of the undisturbed medium which is basically b_o.

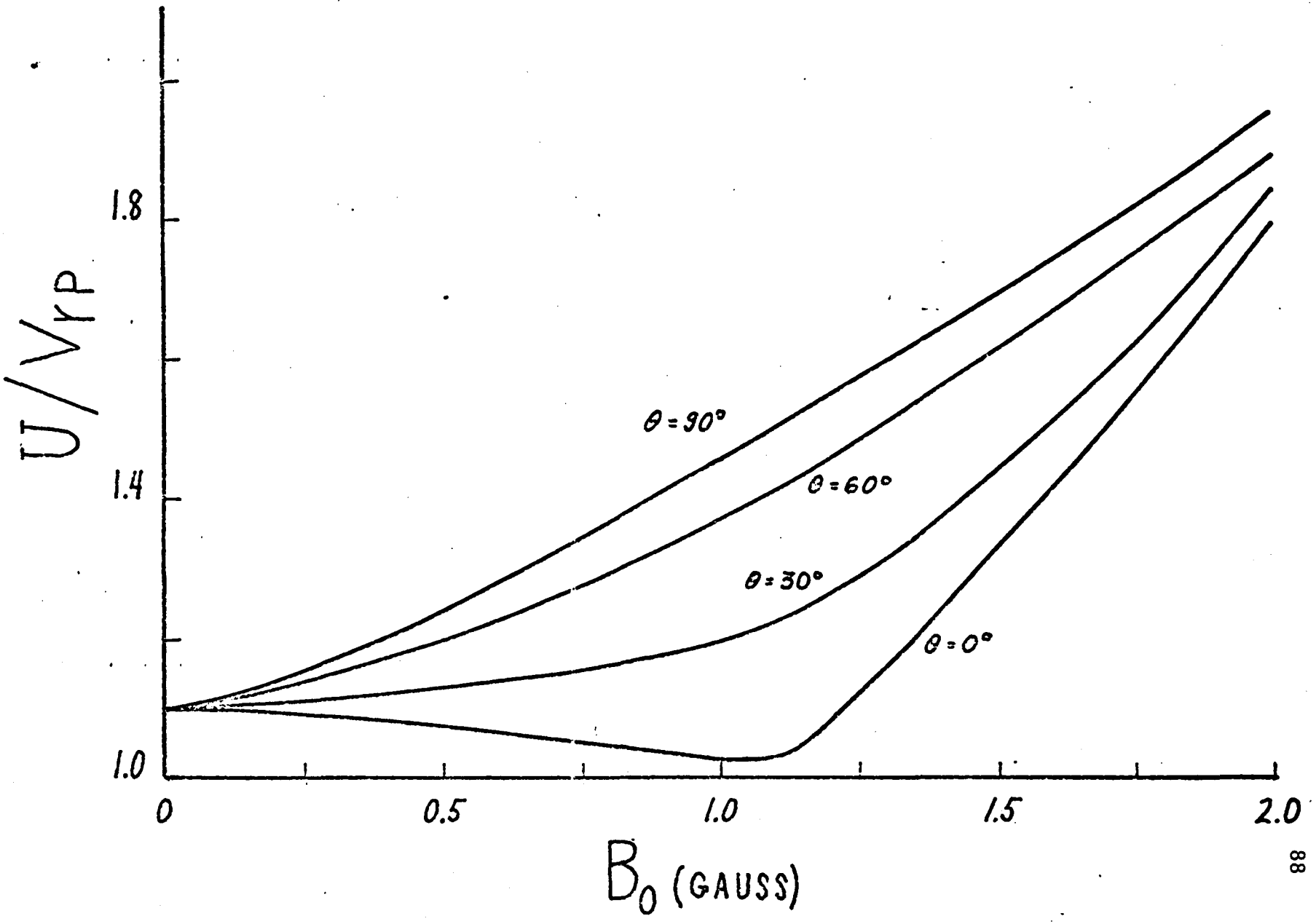

Fig. 4.12 Ratio of shock speed to piston speed vs. uniform magnetic field for spherical piston problem

An analogy with aircraft motion in gasdynamics is possible. For supersonic aircraft speed, the disturbance is confined in a Mach cone[30] near and behind the aircraft. For subsonic speeds, the disturbance propagates ahead of the aircraft at the wave speed of the medium which is the sound speed. In MHD, the situation is more complicated due to the different wave speeds which may exist. In the absence of a magnetic field, the piston is surrounded by a strong gasdynamic shock. For superalfvenic piston motion, the magnetic effects are coupled to these gasdynamic effects. When B_o is increased so that the piston becomes subalfvenic, the magnetic effects travel far ahead of the piston at the Alfven speed.

The change in phenomena described above can be understood with the aid of the Freidrichs diagram, Figure 1.1. For the superalfvenic piston motion (smaller magnetic fields), the sound speed behind the shock is greater than the Alfven speed. Therefore Figure 1.1a applies, the gasdynamic effects travel at the fast wave speed at the pole, and the main shock is basically gasdynamic. As θ increases, the magnetic field becomes more and more coupled to the gasdynamic effects resulting in a decrease in shock density. When the piston becomes subalfvenic, at the pole the Alfven speed behind the shock also becomes greater than the sound speed so that Figure 1.1b applies. The gasdynamic effects now travel at the slow wave speed and the fast shock is primarily magnetic, resulting in negligible gasdynamic shock

strength near the pole. As θ increases, gasdynamic effects become coupled to the fast shock, so that shock density increases slightly with θ.

At the main shock, the tangential magnetic field $B_{\theta s}$, increases in the region away from the pole, as magnetic field is increased and also as θ increases. Near the pole however, $B_{\theta s}$ increases with B_o until the magnetic field becomes greater than 1.0 gauss and then decreases continuously. A shock strength parameter, $f_m = B_{\theta s}/B_{\theta o}$, the ratio of the tangential magnetic field at the shock to the ambient value at that angle, is defined and shown in Figure 4.13. This parameter unlike $B_{\theta s}$ itself, shows a decrease as θ increases for all magnetic fields. Using this definition of shock strength, a reasonable correlation is obtained between shock strength and the shock speed given by Figure 4.12, i.e. shock speed varies inversely as shock strength. This result, that a strong shock travels slower than a weak shock, is in agreement with the planar fast shock results of Section 3.3. Note that, near the pole, f_m increases as B_o increases for subalfvenic piston motions, while f_m decreases for superalfvenic motions. In contrast, for subalfvenic motions, shock speed near the pole decreases as B_o increases, etc.

Figure 4.14 shows the variation in shock pressure with B_o and with θ. For large magnetic fields, the shock pressure is negligible compared to the magnetic pressure. Shock pressure, of course, varies in a similar way to the shock density. Figure 4.15 gives the radial velocity at the shock which decreases as magnetic field is increased.

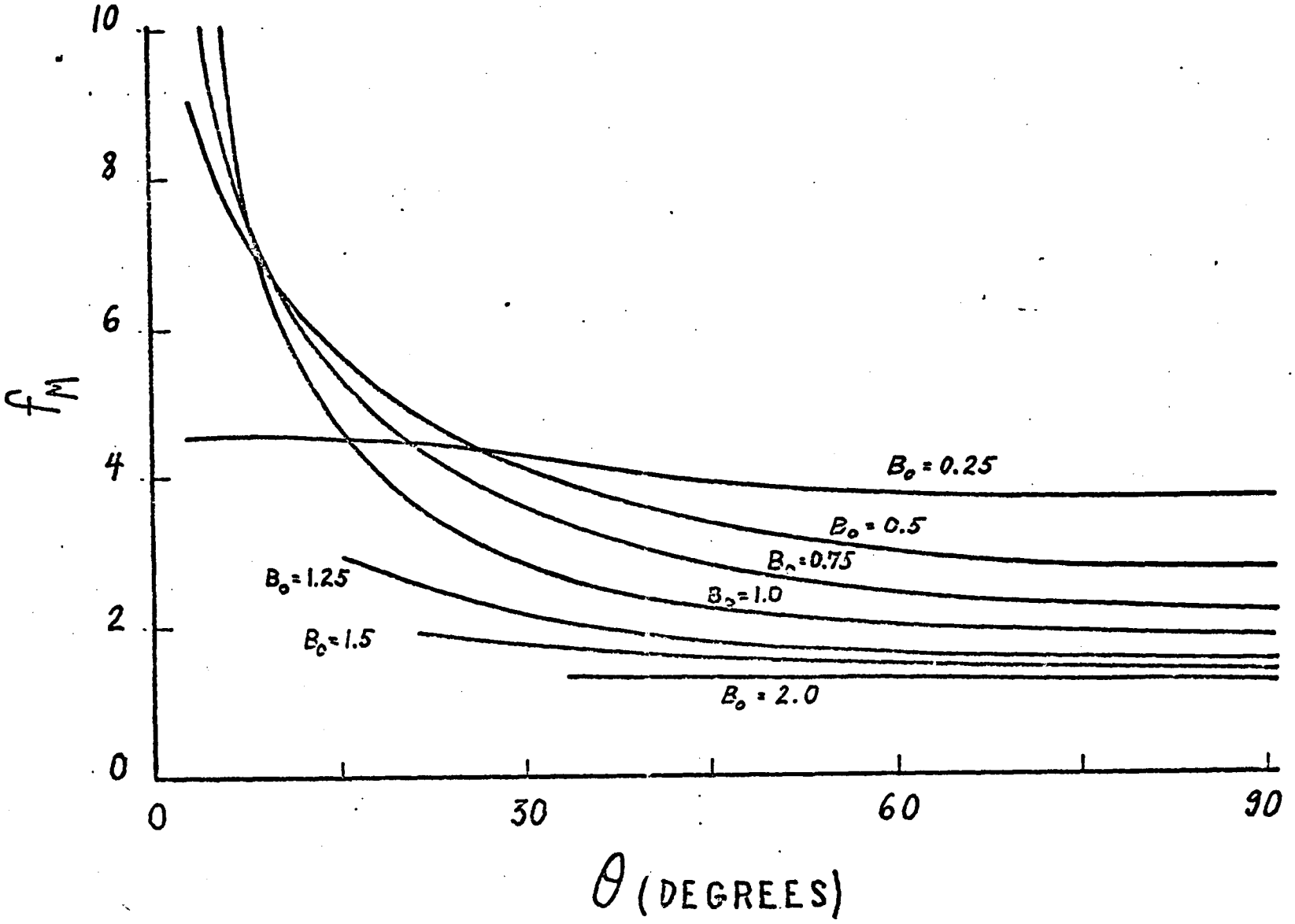

Fig. 4.13 Shock strength ($f_m = B_{\theta_s}/B_{\theta_o}$) vs. θ for spherical piston problem

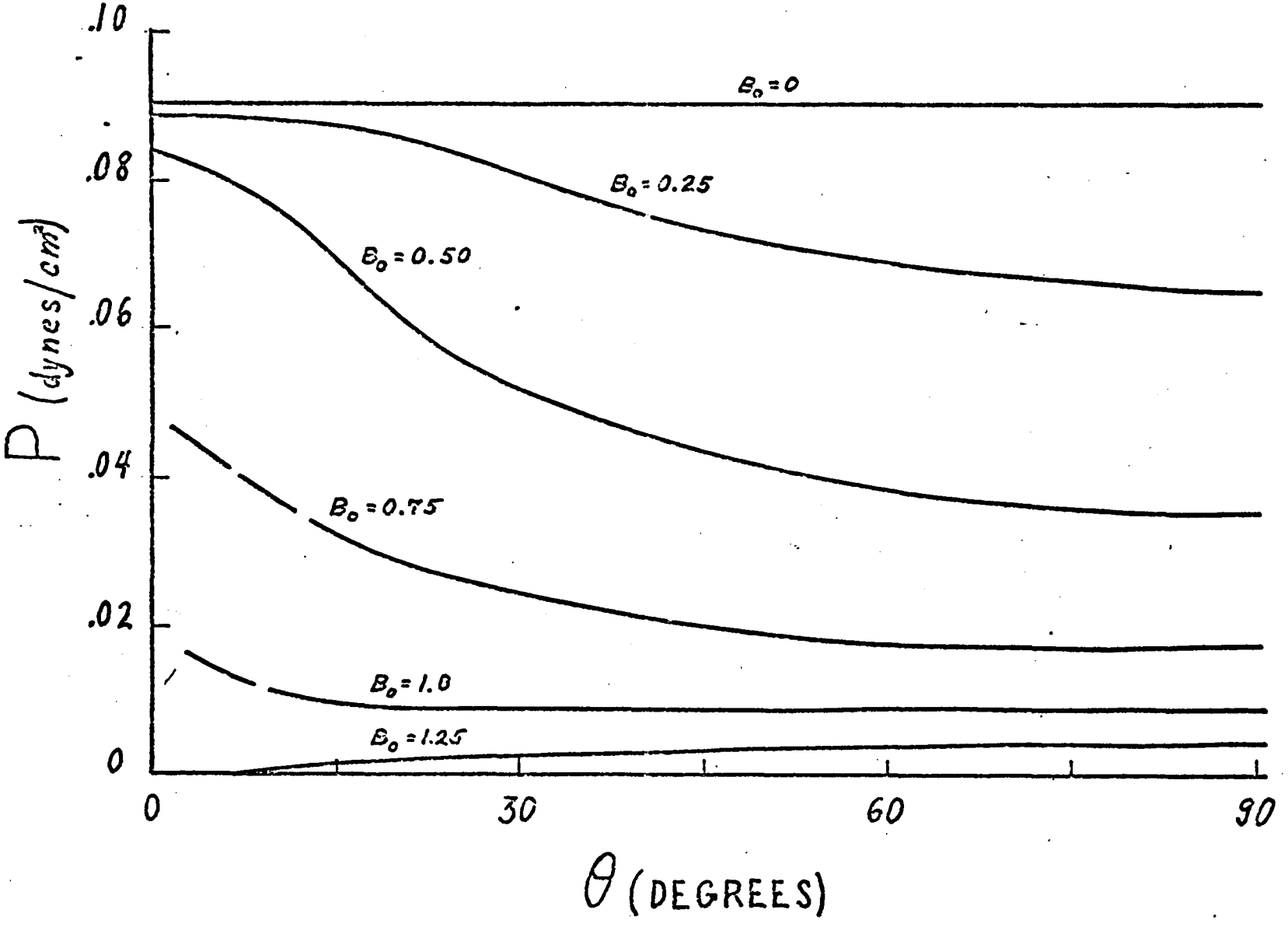

Fig. 4.14 Shock pressure vs. θ for spherical piston problem

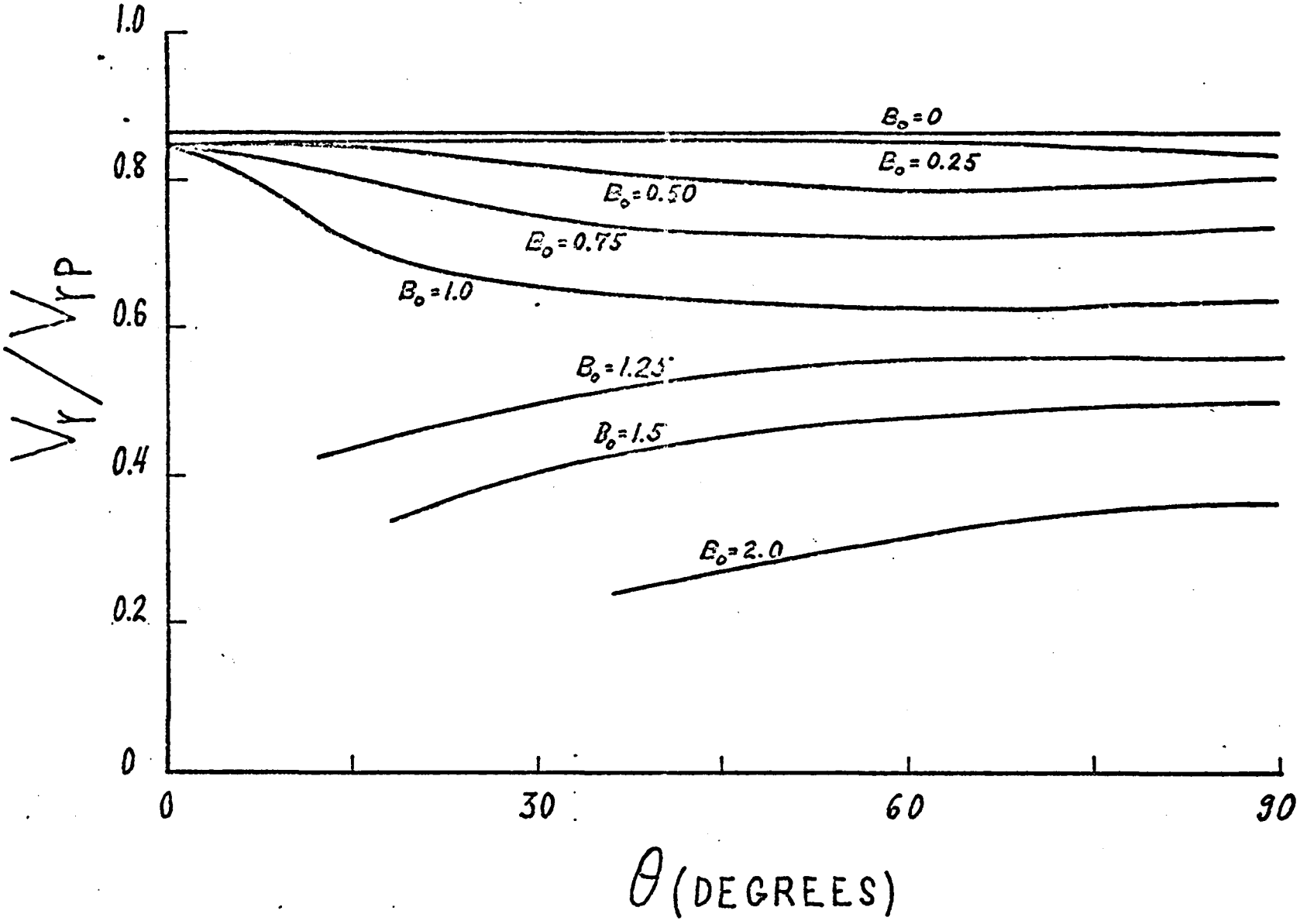

Fig. 4.15 Ratio of radial velocity at shock to piston speed vs. θ for spherical piston problem

The spherical shock results qualitatively compare very well with the planar results of Chapter 3 away from the pole. Near the pole, effects such as the slowing down of the shock are two-dimensional and cannot be predicted by the planar solution. Of course, the quantitative results differ greatly and planar calculations cannot give the correct picture between the shock and the piston.

(b) The Region Between the Main Shock and the Piston:

The solution in the region between the shock wave and the piston is very different from the solution in the same region for the planar piston problem presented in Section 3.3. For the planar piston problem, the governing MHD equations in slab symmetry are reducible; therefore the solution must be simple waves (or shocks formed by the steepening of simple compression waves) separated by regions of constant state. It was found that for the given ambient data a slow shock was present behind the main fast shock. This slow shock was necessary to satisfy the boundary conditions on the velocity at the piston, since there are restrictions on the behavior of simple waves. In spherical coordinates, the equations are not reducible so that simple waves do not exist. The slow spherical MHD wave necessary to satisfy the boundary conditions gives a boundary region of large density and pressure near the piston only for small θ and large B_o, but in general no slow shock is present.

Figure 4.16 shows the mass density between the piston ($r = 2500$ cm) and the elliptic shock for three different ambient magnetic

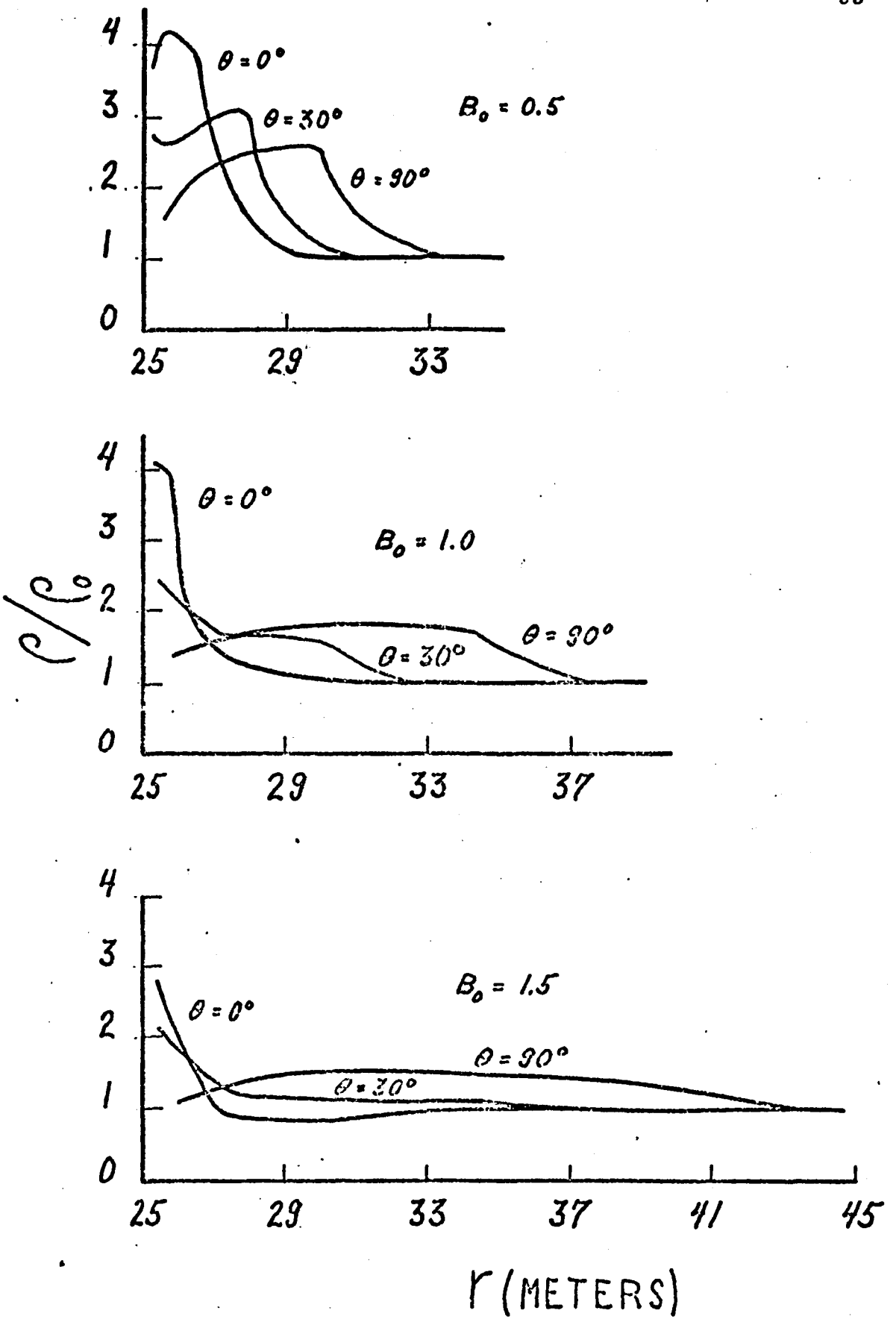

Fig. 4.16 Density vs. radius (t = 2.0 x 10^{-3} sec) for spherical piston problem

fields, giving the continual decrease in density near the equator as the shock is pushed faster by the stronger magnetic fields. Near the pole however, the entire picture changes with magnetic field. When the piston becomes subalfvenic (large B_o), the density jump at the shock becomes negligible since the Alfven speed behind the shock is now greater than the sound speed, so that the magnetic effects dominate in the fast shock. The large gasdynamic effects are now carried by a slow spherical wave confined closer and closer to the piston as magnetic field is increased. Note, in Figure 4.16, the flattening out of the curve for $B_o = 1.0$ gauss and $\theta = 0$ in front of this region of large density. At $B_o = 1.5$ gauss, a rarefaction wave is visible behind the shock which now has no visible density jump. At $B_o = 4.0$ gauss, Figure 4.6, the rarefaction wave is much stronger and extends up to $\theta = 40^o$. This rarefaction wave is not present until the piston becomes subalfvenic.

The rarefaction wave is the result of the large tangential motion of fluid toward the equator which is a purely magnetic effect due to the curvature of the magnetic field lines near the pole which are frozen into the fluid. Particles entering the shock are swept toward the equator preventing their accumulation near the pole. The tangential velocity v_θ increases behind the shock as in Figure 4.7 until it reaches a maximum near but not at the piston, Figure 4.17 is a plot of this maximum tangential velocity. It is seen that v_θ increases with magnetic field and that the maximum occurs at an angle θ from the pole of less than 20^o

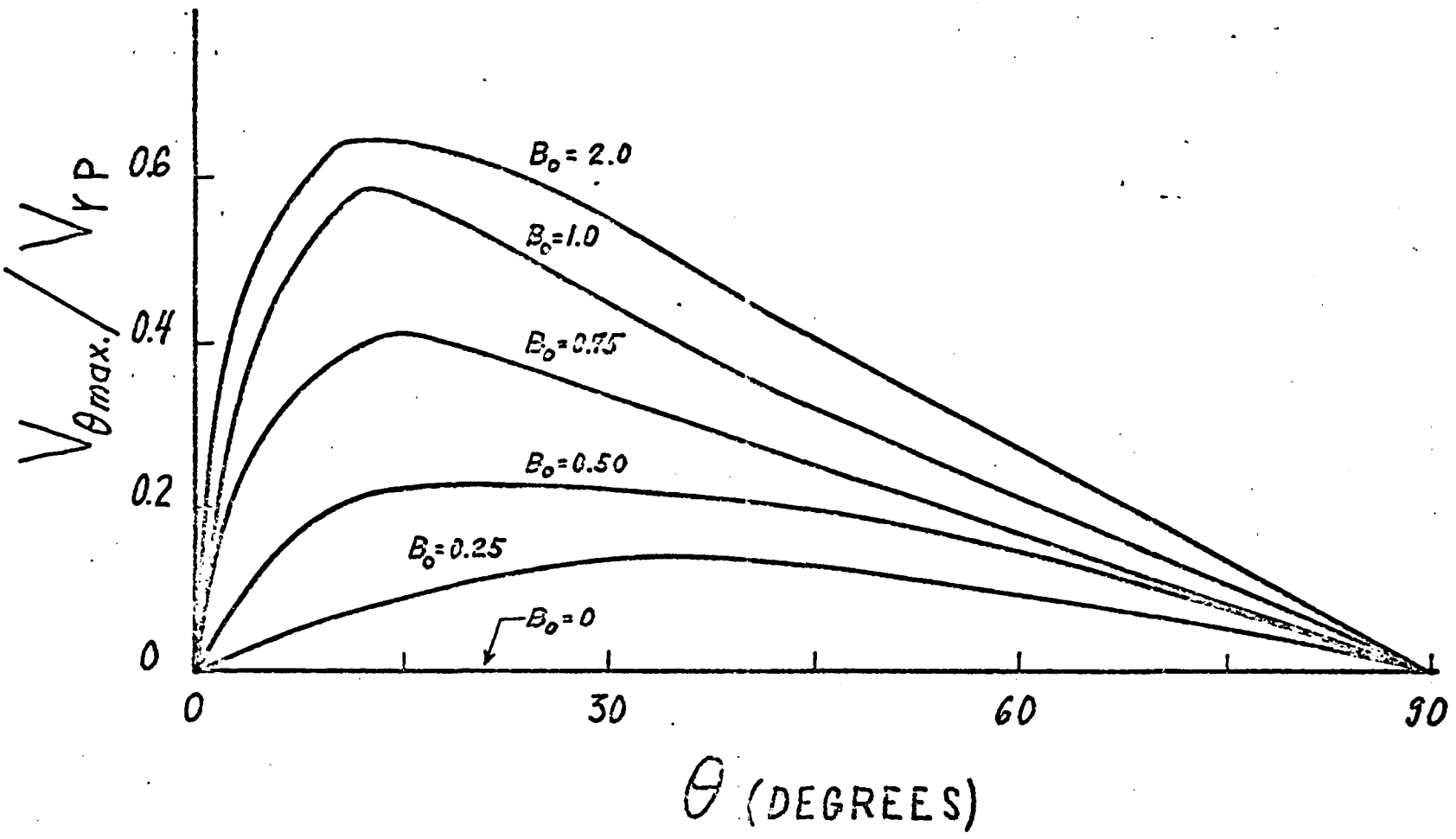

Fig. 4.17 Maximum tangential velocity vs. θ for spherical piston problem

for large magnetic fields.

Tangential magnetic field B_θ also increases behind the fast shock to a maximum near the piston as in Figure 4.4. This maximum value of B_θ varies both with θ and with B_o in the same manner as $B_{\theta s}$. Radial magnetic field decreases continually from its ambient value to zero at the piston (the boundary condition). Radial velocity increases from the shock value given by Figure 4.15 to its maximum value, the piston velocity v_{rp}. Pressure varies in the same way as density.

The solutions presented cover the complete range of magnetic fields where the asymtotic solutions are invalid. Therefore, the spherical piston problem may be considered solved.

4.4 Summary

In this chapter, solutions to the spherical piston problem were presented for the first time for the complete range of magnetic fields. The solutions showed good agreement with the known solutions for the asymtotic cases of very small magnetic field and very large magnetic field. Solutions to the full nonlinear problem were discussed in terms of a parameter f_m, the ratio of the tangential magnetic field at the shock to the ambient tangential field, which was taken to represent the strength of the MHD shock wave. It was found that the shock speed varied inversely as f_m for all magnetic fields.

A drastic change in shock properties were discovered at a critical magnetic field corresponding to when the piston speed became subalfvenic with respect to the ambient Alfven speed. At this field, a rarefaction wave was also discovered near the pole and attributed to the large tangential motion of fluid behind the shock wave.

It was shown that rezoning was necessary to eliminate errors in the numerical calculation, especially near the piston. More importantly, without rezoning the solution cannot be obtained for large time without the expenditure of an enormous amount of computer time, but with rezoning, these results may easily be obtained in a reasonable time.

The results of this chapter demonstrate that nonlinear two-dimensional unsteady MHD problems can be successfully studied using Lagrangian codes and modern high speed computers.

CHAPTER 5

MHD BLAST WAVES

The problem of the expansion of a sphere of gas initially having very high pressure and internal energy has been extensively studied, but the effects of a uniform magnetic field on this expansion have not as yet been determined. The most useful mathematical model in studying this problem is the blast wave model which assumes that the internal energy and pressure are uniformly distributed within the sphere or "fireball" which initially contains gas at the same density as the ambient atmosphere. Therefore, the initial model is two constant states separated by a discontinuity in internal energy and pressure at the radius of the fireball which is allowed to expand under the restriction that the total energy of the flow remains constant.

This initial discontinuity or interface gives rise to a shock wave propagating outward, a contact surface behind it, and a rarefaction wave propagating inward toward the origin. In addition, a second shock which travels inward is formed a short time later. The existing work for the gas-dynamic model was reviewed in Chapter 1.

In this chapter, a uniform magnetic field, both inside and outside the fireball, is added to the blast wave model and its influence on the flow investigated numerically using the method of artificial viscosity discussed in Chapter 2. This method utilizes Lagrangian coordinates

which are particularly useful here in locating the position of the fireball interface (a contact surface) at any time. The fireball is given an initial radius of 500 cm and a pressure and internal energy 10^4 times the ambient values given by (2.7). Studies are made for various magnetic fields, first using MHD WUNDY for planar one-dimensional blast waves, and second using MHD CYCLONE for spherical blast waves.

5.1 Planar MHD Blast Waves

The planar one-dimensional problem is investigated numerically using MHD WUNDY in order to determine the effects of a magnetic field upon blast waves, since solutions to this problem, either for spherical or for plane geometry, have not as yet been presented. Results are presented here for magnetic fields of 0.5 and 2.0 gauss oriented at angles θ with the x direction (the direction of propagation of the shock wave) of 0, 10, 30, 60 and 90 degrees. For $\theta = 0^{o}$, the magnetic field, which lies in the x direction, is uncoupled from the flow giving the gas-dynamic solution. First let us discuss the solutions for $\theta = 0^{o}$ and $\theta = 90^{o}$.

The pressure inside the fireball is initially very high, thus pushing the interface outward at a high speed, compressing the ambient gas ahead of it, thereby forming a shock wave. If a magnetic field is present, its tangential component B_y ahead of the interface is also increased since the field lines are frozen into the fluid for infinite electric conductivity. The outward motion of the interface results in a decrease in density and pressure (and therefore B_y) behind it, causing a rarefaction wave to propagate toward the origin. The resulting outward motion of the gas inside the fireball gives a low pressure and density at the origin and a large positive pressure gradient nearby. This pressure gradient stops the outward motion and produces a second shock propagating inward which readjusts the pressure and density inside the fireball.

The work of Chou and Huang[23] for gasdynamics, reviewed in Chapter 1, also gives this secondary shock. However they can only follow this shock until it implodes on the origin, while the results to be presented here follow this shock after it reflects at the origin.

Figure 5.1 gives the pressure distribution at different times for the gasdynamic case ($\theta = 0^{o}$) showing the decay of the main shock with time and the position, I, of the interface. At the time $t = 0.27 \times 10^{-3}$ sec., the pressure near the origin has decreased significantly and the second shock, smoothed out by the artificial viscosity, is propagating toward the origin. At $t = 0.42 \times 10^{-3}$ sec., the shock has been reflected at the origin and is beginning to propagate outward. The curves at later times show the second shock, visible as a bump on the pressure diagram, as it catches up to the main shock. Included in Figure 5.1 is a curve of the total pressure, gasdynamic plus magnetic pressure ($p_m = B_y^2/8\pi$), for 0.5 gauss and $\theta = 90^{o}$ at a time $t = 2.70 \times 10^{-3}$ sec. The additional magnetic pressure pushes the main shock out faster but slows down the interface slightly due to a positive gradient $\partial p_m/\partial x$ there. This results in a slight decrease in gas pressure p, though the total pressure ($p + p_m$) is of course larger. The secondary shock is present as in the gasdynamic results.

Figure 5.2 gives the gas density versus position at $t = 2.7 \times 10^{-3}$ sec., for gasdynamics ($\theta = 0^{o}$) and for magnetic fields of 0.5 and 2.0 gauss at $\theta = 90^{o}$. For both magnetic fields, the effect

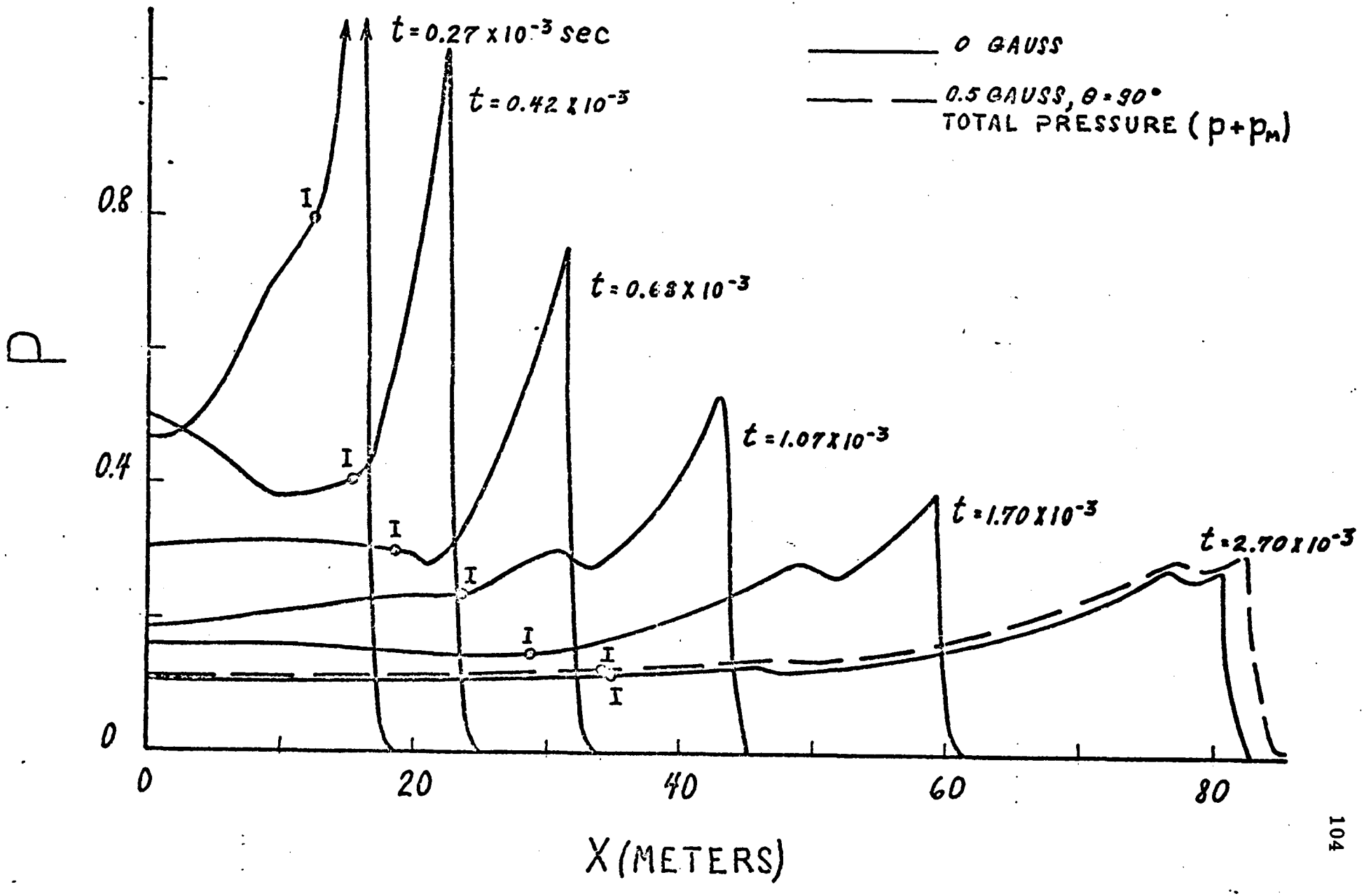

Fig. 5.1 Pressure vs. position at different times for planar blast waves

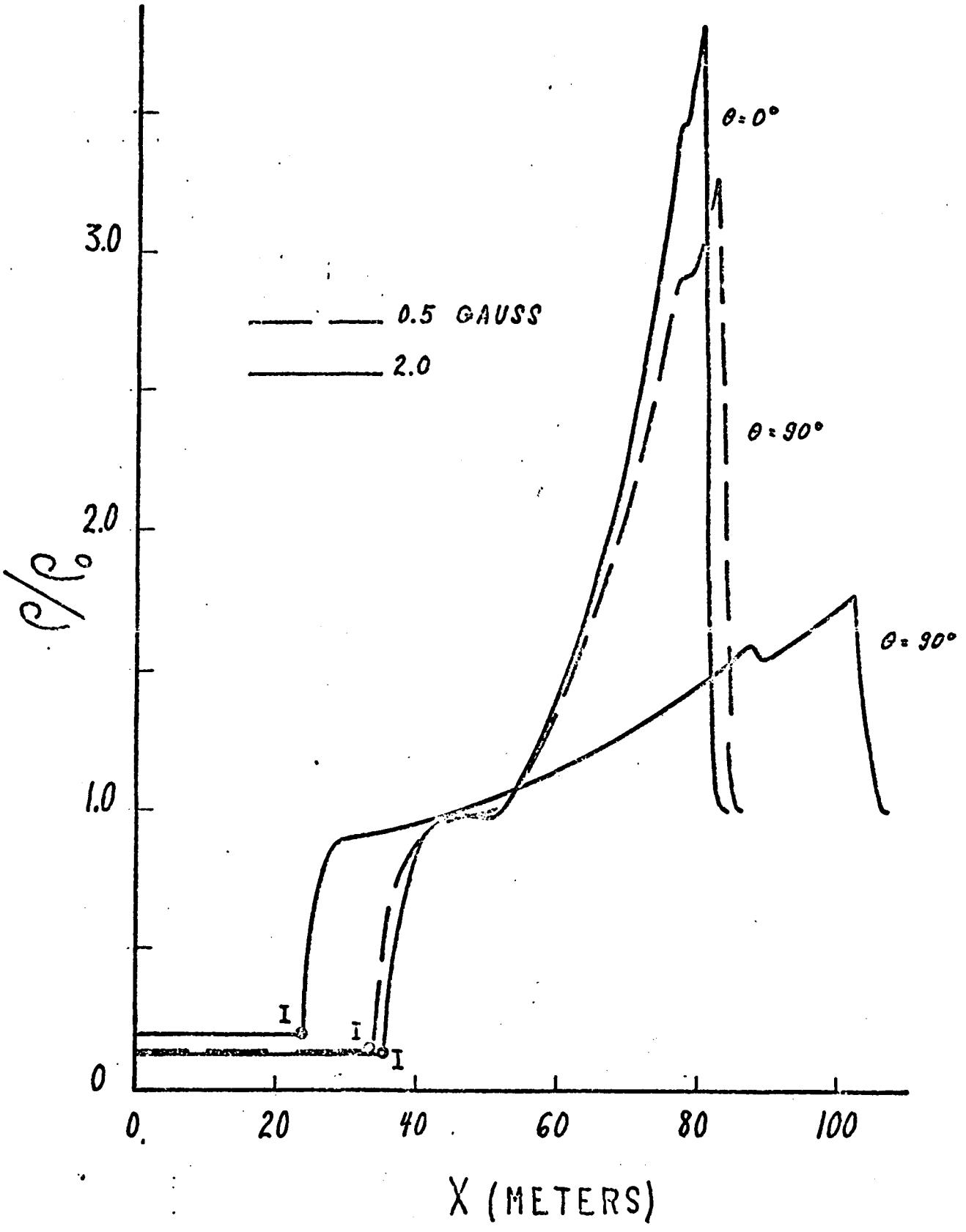

Fig. 5.2 Density vs. position ($t = 2.70 \times 10^{-3}$ sec) for planar blast waves

of the field is to make the shock propagate faster and to decrease its density, the larger field giving much larger charges. The interface, previously noted as the location of a contact surface (a surface of discontinuity in density), is visibly slowed down by the larger field. Inside the fireball, density becomes very small, the lowest value occurring for gasdynamics where the interface has propagated out the furthest. Velocity profiles show a continual increase in particle velocity v_x with distance from the origin, reaching a maximum at the main shock. Since electric conductivity is very great, tangential magnetic field profiles are identical to the density profiles. Thus, the magnetic field gives a magnetic pressure which tends to decrease the velocity of a particle as it falls behind the shock . All curves show the bump which represents the reflected secondary shock.

For $\theta = 90^{o}$, the Friedrichs diagram, Figure 1.1, gives a zero slow wave speed. The solution is more complicated when, initially, the magnetic field is not perpendicular to the direction of propagation of the shock, since both fast and slow magnetohydrodynamic wave speeds are present. As discussed, initially B_y is increased in front of the interface and decreased behind it, resulting in a positive gradient $\partial B_y/\partial x$ at the interface and negative gradients both ahead of and behind it. This change in the curvature of the magnetic field lines at the interface results in a discontinuity in tangential velocity v_y which is the most visible slow wave effect. From equation (2.25), it can be seen that v_y is proportional

to the magnetic field gradient, giving v_y negative both in front of and behind the interface and positive at the interface. This discontinuity propagates in both the positive and negative x directions at the slow wave speed.

Figure 5.3 shows the tangential magnetic field B_y and tangential velocity v_y versus distance from the origin x for initial magnetic fields of 0.5 and 2.0 gauss oriented at angles θ to the x axis. For $\theta = 90^o$, where the slow wave speed is zero, a discontinuity in B_y occurs at the interface (the contact surface) and v_y is zero. For 0.5 gauss and for $\theta = 30^o$, this discontinuity in B_y and the accompanying discontinuity in v_y have propagated outward from the interface, denoted by I, at the slow wave speed while an inward propagating disturbance has almost reached the origin. The gasdynamic effects of these waves (pressure and density jumps) are very weak. At the main shock, which is predominantly gasdynamic, particles are accelerated in the negative y direction by the negative gradient $\partial B_y/\partial x$, while behind the shock, these particles are given the opposite acceleration by the positive gradient, v_y eventually becoming positive.

For 2.0 gauss, the magnetic field effects are much greater resulting in large gasdynamic jumps at the slow wave which has steepened into a slow shock. This slow shock travels faster for $\theta = 30^o$ than for $\theta = 60^o$ (the slow wave speed decreases as θ increases in Figure 1.1) and is accompanied by large changes in B_y and v_y.

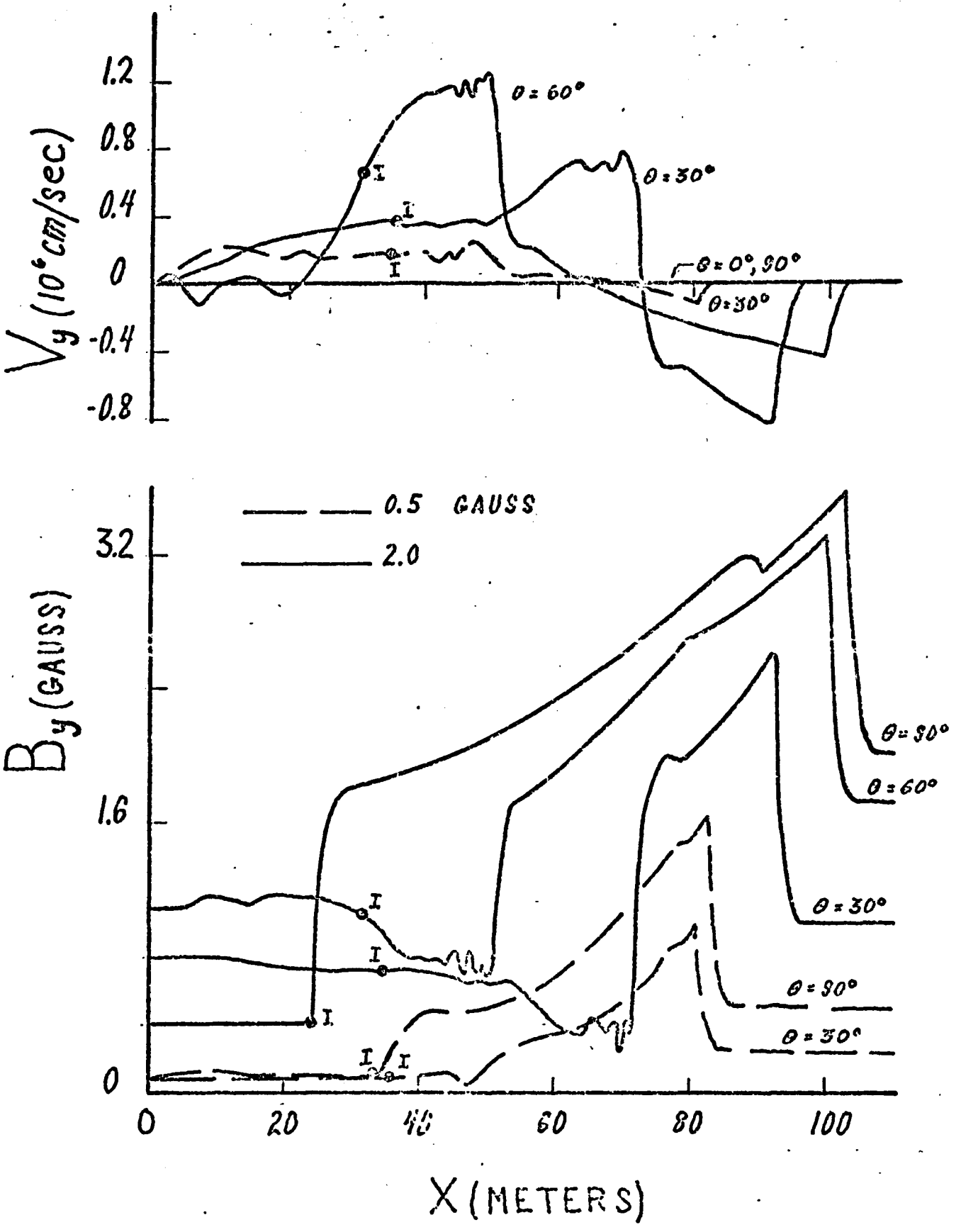

Fig. 5.3 Tangential magnetic field and velocity vs. position ($t = 2.70 \times 10^{-3}$ sec) for planar blast waves

Figure 5.4 gives the density profiles at $\theta = 30^{o}$ for this magnetic field for different times. At $t = 0.68 \times 10^{-3}$ sec., the second (slow), shock is already visible behind the main fast shock. This slow shock grows in strength as the fast shock decays with time. It is clear that as time increases, the gasdynamic shock effects are becoming more strongly associated with the slow shock. The slow shocks for larger θ are weaker but also increase in strength with time.

Figure 5.5 shows the total pressure (gasdynamic plus magnetic) versus position for 2.0 gauss and for $t = 2.70 \times 10^{-3}$ sec. For $\theta = 30^{o}$ and $\theta = 60^{o}$, the split into fast and slow shocks is clearly visible and coincides with the jumps in B_y and v_y in Figure 5.3. At the fast shock the jump in total pressure increases with θ resulting in greater shock speeds. At the slow shock, however, the jump is greatest at $\theta = 30^{o}$. The reflected secondary shock discussed for Figure 5.1, is still present but has been greatly reduced in strength for $\theta = 30^{o}$ and $\theta = 60^{o}$ due to passing through the slow shock. Profiles of particle velocity v_x also show the split into fast and slow shocks and the damping of the reflected shock.

It is obvious from the profiles that the blast wave solutions, unlike the piston solutions of Chapters 3 and 4, where the interface was maintained at a constant speed, vary with time. A study was made of the flow variables at the unsteady shock waves and the results at a given time compared with the shock solutions for the piston problem.

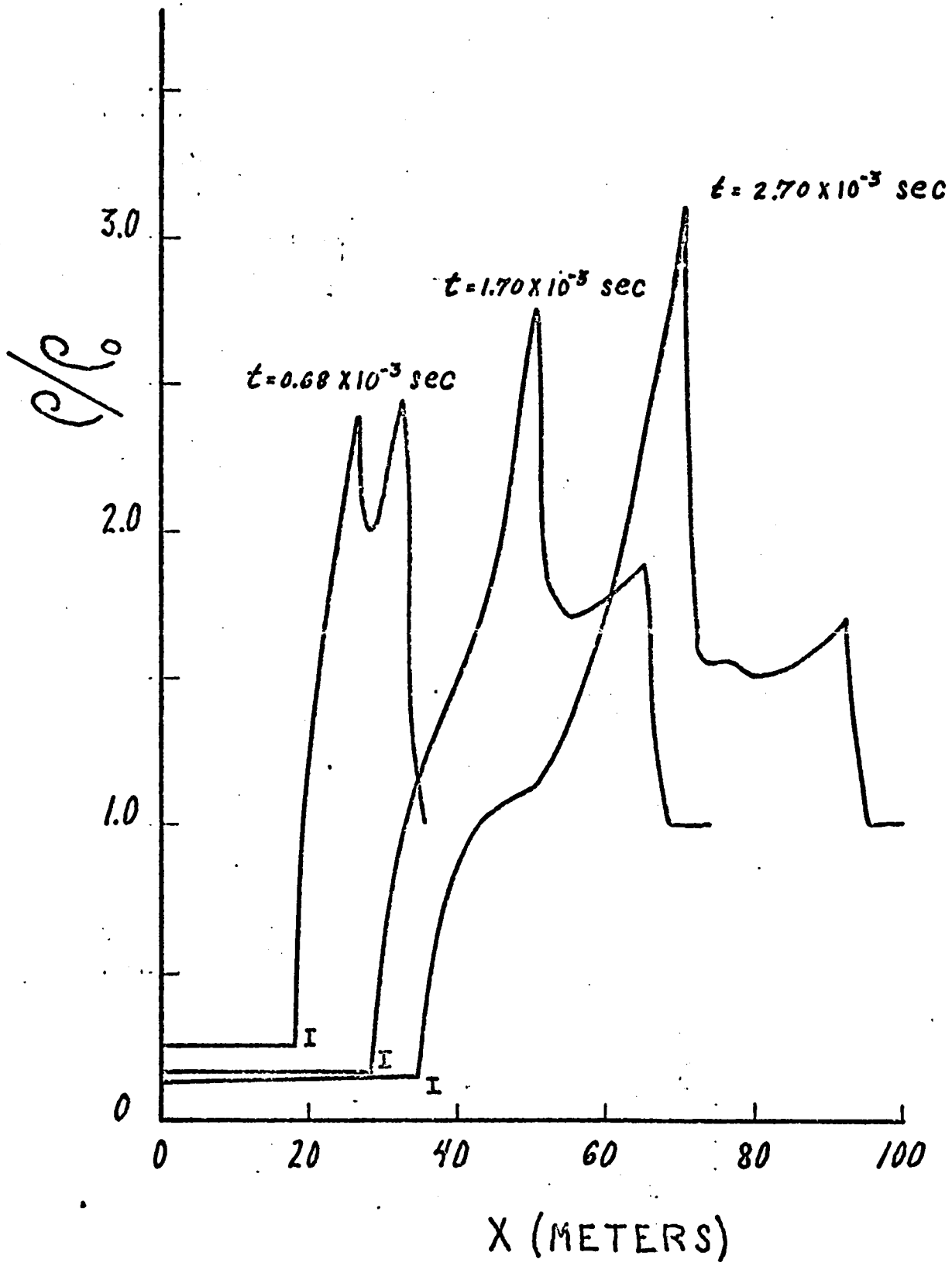

Fig. 5.4 Density vs. position (B_o = 2.0 gauss, θ = 30°) for planar blast waves

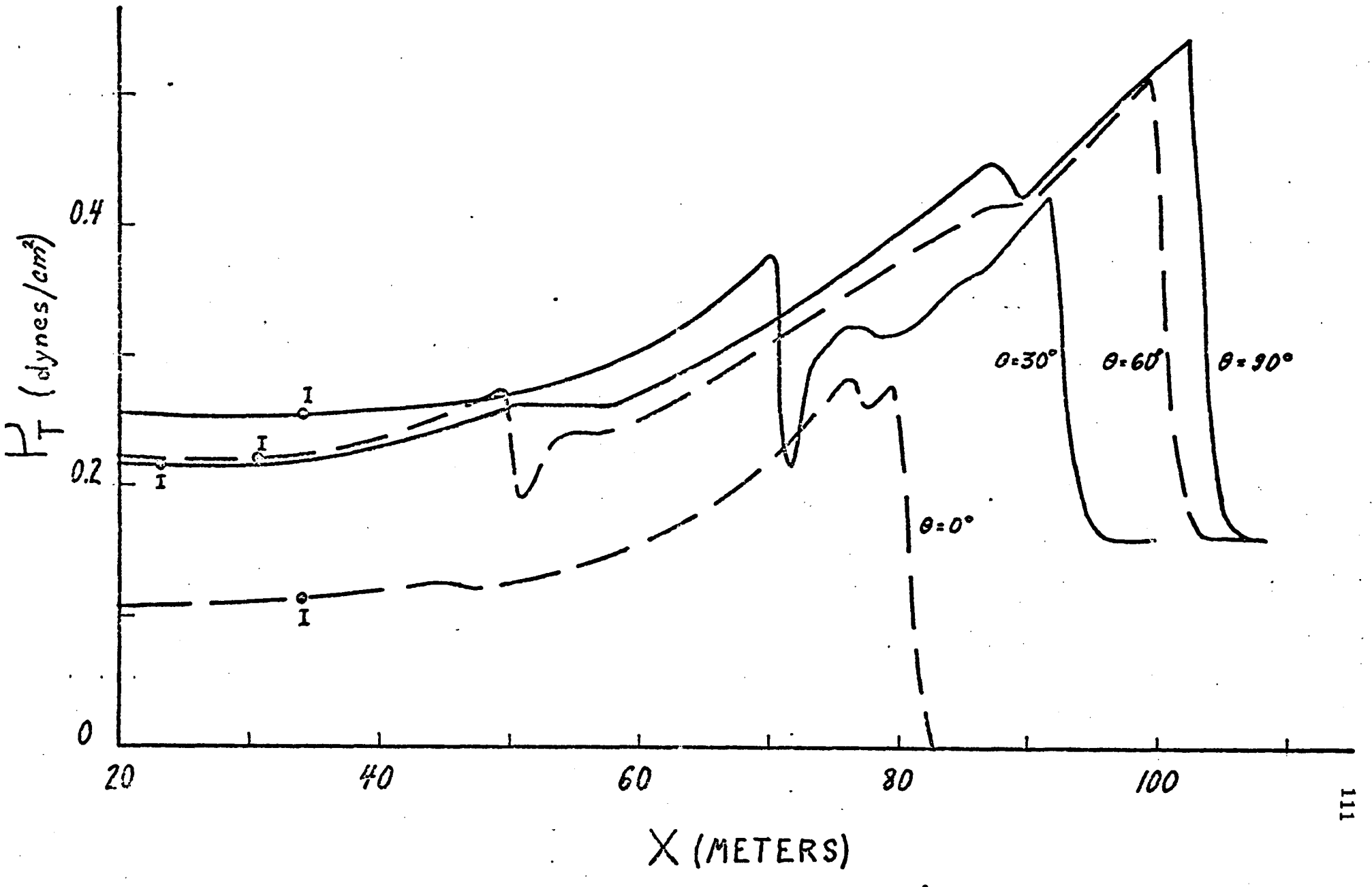

Fig. 5.5 Total pressure ($p+p_m$) vs. position (B_o = 2.0 gauss, t = 2.70 x 10^{-3} sec) for planar blast waves

Figure 5.6 gives the positions of the main fast shock, the slow shock (or slow wave), and the fireball interface as a function of time. Since the slopes of all curves decrease with time, the speeds of all shocks and of the interface decrease with time.

For 0.5 gauss, at a given time the interface speed is decreased slightly perpendicular to the field. However for 2.0 gauss, the interface at $\theta = 90^{o}$ is slowed down and almost stopped by the magnetic field, while for $\theta = 10^{o}$ the interface speed is slightly greater than for the gasdynamic case. These results imply that for the spherical blast wave problem the interface will not remain spherical but will become elliptic with major axis along the pole (the direction of the applied magnetic field), the eccentricity of the ellipse increasing both as time and as magnetic field strength increase.

The fast shock speed is increased slightly by the small magnetic field at $\theta = 90^{o}$ and a great deal by the larger magnetic field leading to the conclusion that the fast shock is also elliptic with its major axis along the equator and that it becomes more elliptic at larger times. For 0.5 gauss, the slow "shock" is really a slow wave characterized by large changes in v_y and B_y and negligible changes in pressure and density. For 2.0 gauss, it has been shown that a true slow shock exists with a speed that decreases as θ increases. Note that as θ approaches zero, the fast and slow shocks tend to coincide since the magnetic field is uncoupled from the flow. For $\theta = 90^{o}$, the slow shock is not present

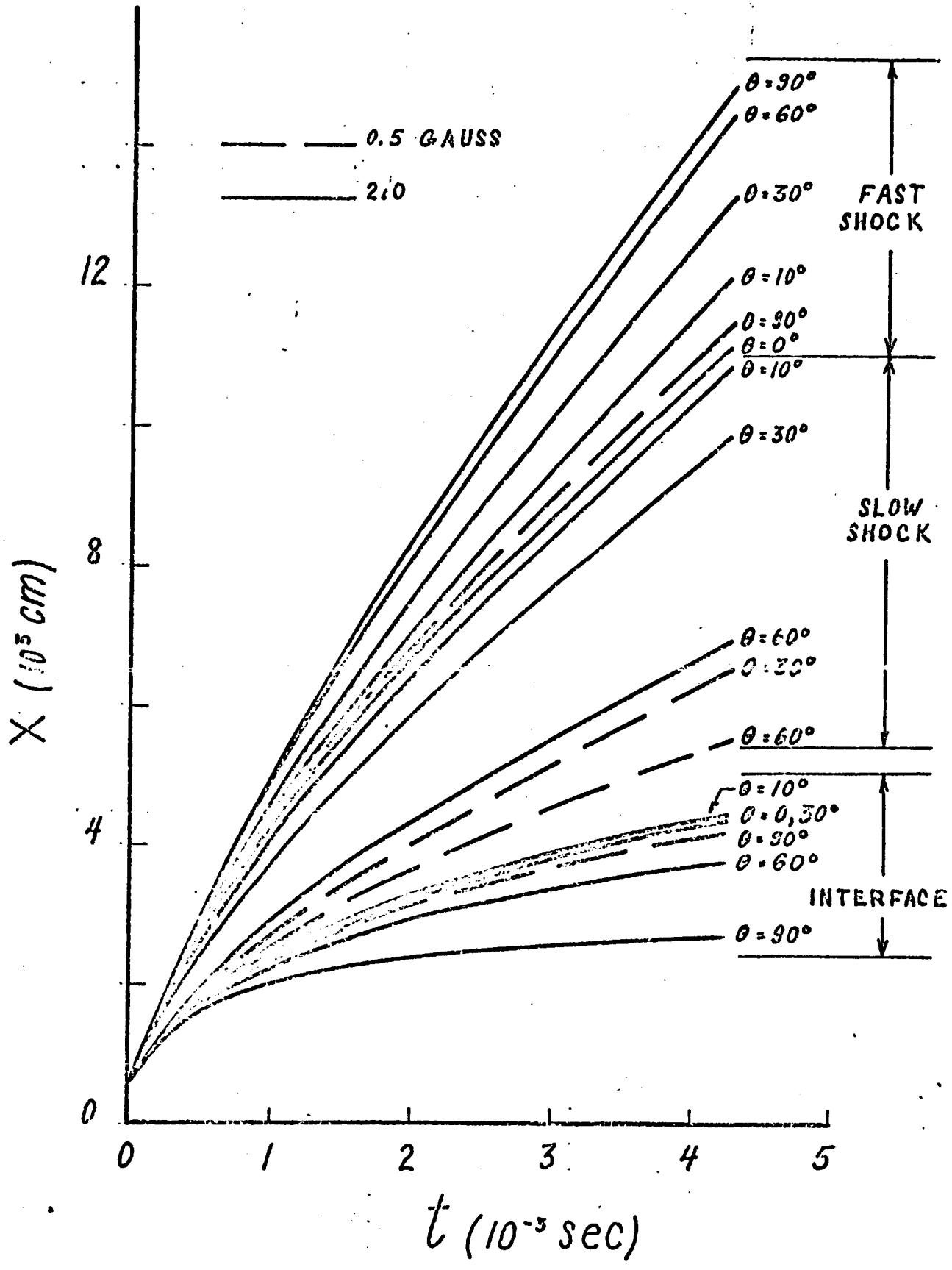

Fig. 5.6 Positions of shocks and interface vs. times for planar blast waves

since the slow wave speed is zero.

Figure 5.7 gives the ratio of the density at the shock to the density in front of it for both the fast and slow shocks. For the given initial data, it takes approximately 0.5×10^{-3} sec. to form the shock completely. The gasdynamic results ($\theta = 0^{o}$) show a slight increase in density with time as a significant number of particles entering the shock remain there. A magnetic field (a positive magnetic pressure gradient) increases the total pressure gradient behind the shock, pulling these particles out of the shock so that the shock density decreases with time, the rate of decrease becoming larger for larger magnetic fields.

For 0.5 gauss, at a given time the fast shock density decreases as θ increases. For 2.0 gauss, however, this is only true for small times. For larger times, this comparatively small density increases with θ. At the same time the slow shock density is becoming very large particularly at small θ. This result, also obtained for the planar piston problem, signifies that at small θ the fast shock is primarily magnetic with the slow shock carrying the bulk of the gasdynamic disturbance. The change in variation with θ as time increases also is observed for 2.0 gauss both for the axial particle velocity at the shock v_x given by Figure 5.8 and for shock pressure curves.

The change in phenomena may be explained with the use of the Friedrichs diagram, Figure 1.1. Initially, due to the large pressure inside the fireball, the sound speed behind the shock is much greater

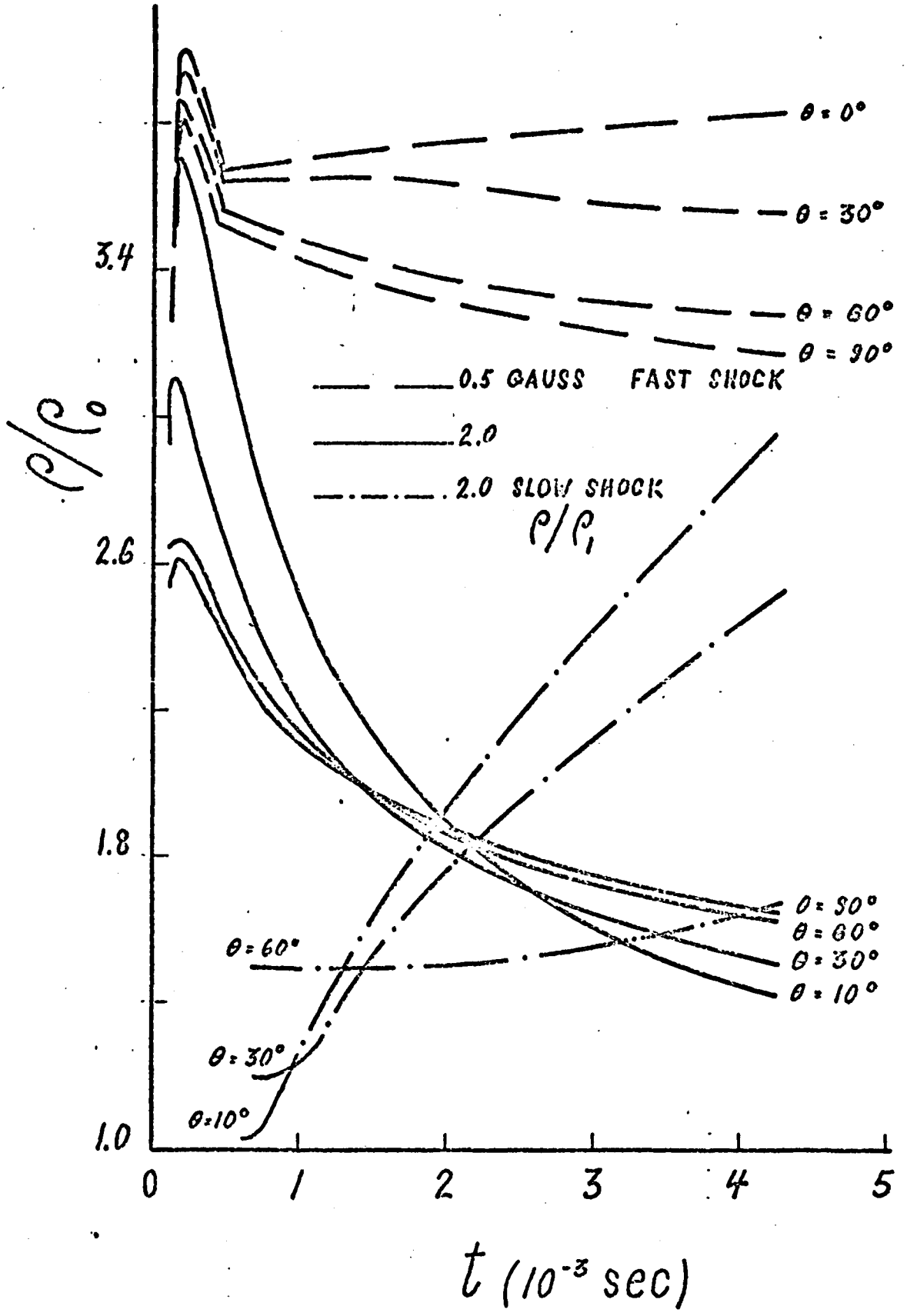

Fig. 5.7 Shock density vs. time for planar blast waves

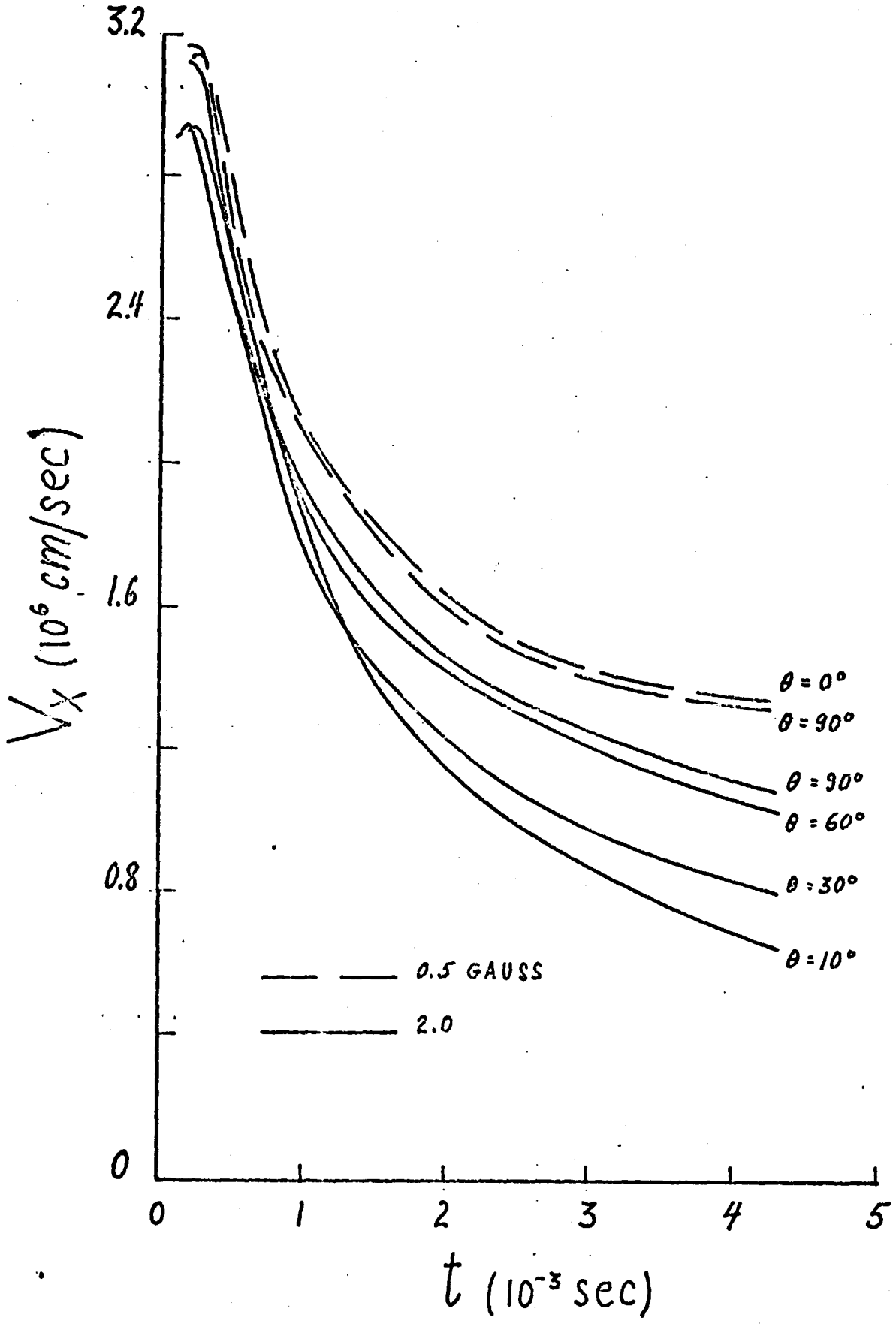

Fig. 5.8 Axial velocity at fast shock vs. time for planar blast waves

than the Alfven speed so that Figure 1.1a applies. For 0.5 gauss, this remains true for larger times. However, for 2.0 gauss, the pressure decay results in the sound speed becoming smaller than the Alfven speed so that Figure 1.1b now applies. Since for small θ , the magnetic part of the disturbance may be considered to be primarily carried by the wave corresponding to the Alfven speed (the slow wave for Figure 1.1a, the fast wave for Figure 1.1b) and the gasdynamic part by the sound wave, for larger times, the slow shock becomes primarily gasdynamic and the fast shock magnetic, thus accounting for the change in variation and for the very small density in the fast shock. Note that for 2.0 gauss and for large times, the curves of Figures 5.7 and 5.8 imply a solution for $\theta = 0$ different from the gasdynamic results (magnetic field uncoupled) in order to give a continuous variation with θ. A two-dimensional effect, not obtainable from the planar model, must be anticipated near the pole for the spherical model.

Continuing the comparison with the piston model, a shock strength parameter, $f_m = B_{y_1}/B_{y_o}$, may be defined and its variation with magnetic field and θ studied. As for the piston solutions, f_m decreases both as θ and as magnetic field increase. Again it is found that shock speed varies inversely as f_m and that shock density varies directly as f_m where the shock is primarily gasdynamic and inversely as f_m where the shock is magnetic.

Figure 5.9 gives the variation in tangential velocity at the fast and slow shocks with time. At the fast shock the magnitude of v_y is a good indication of the importance of the magnetic effects. v_y increases as magnetic field is increased and decreases as θ is increased. For the slow shock, the magnitude of v_y is not a good measure of the magnetic effects since v_y is not zero in front of this shock; the jump in v_y is a better indication. From Figure 5.3, for 2.0 gauss, this jump is greater for $\theta = 30^o$ than for $\theta = 60^o$. The magnitude of v_y at the slow shock remains almost constant, thus giving the impression that a mass motion, continuing even for large times, will be present in the spherical case involving motion of fluid in opposite directions at the fast and slow shocks.

The planar blast wave solution presented above is the first solution which shows the effect of a magnetic field on the problem. This solution was considered as approximating a given solid angle of the spherical expansion into a uniform magnetic field so that qualitative predictions about the spherical solution may be made. Since the spherical computations require an enormous amount of computer time to achieve results at large times, these qualitative predictions are most useful.

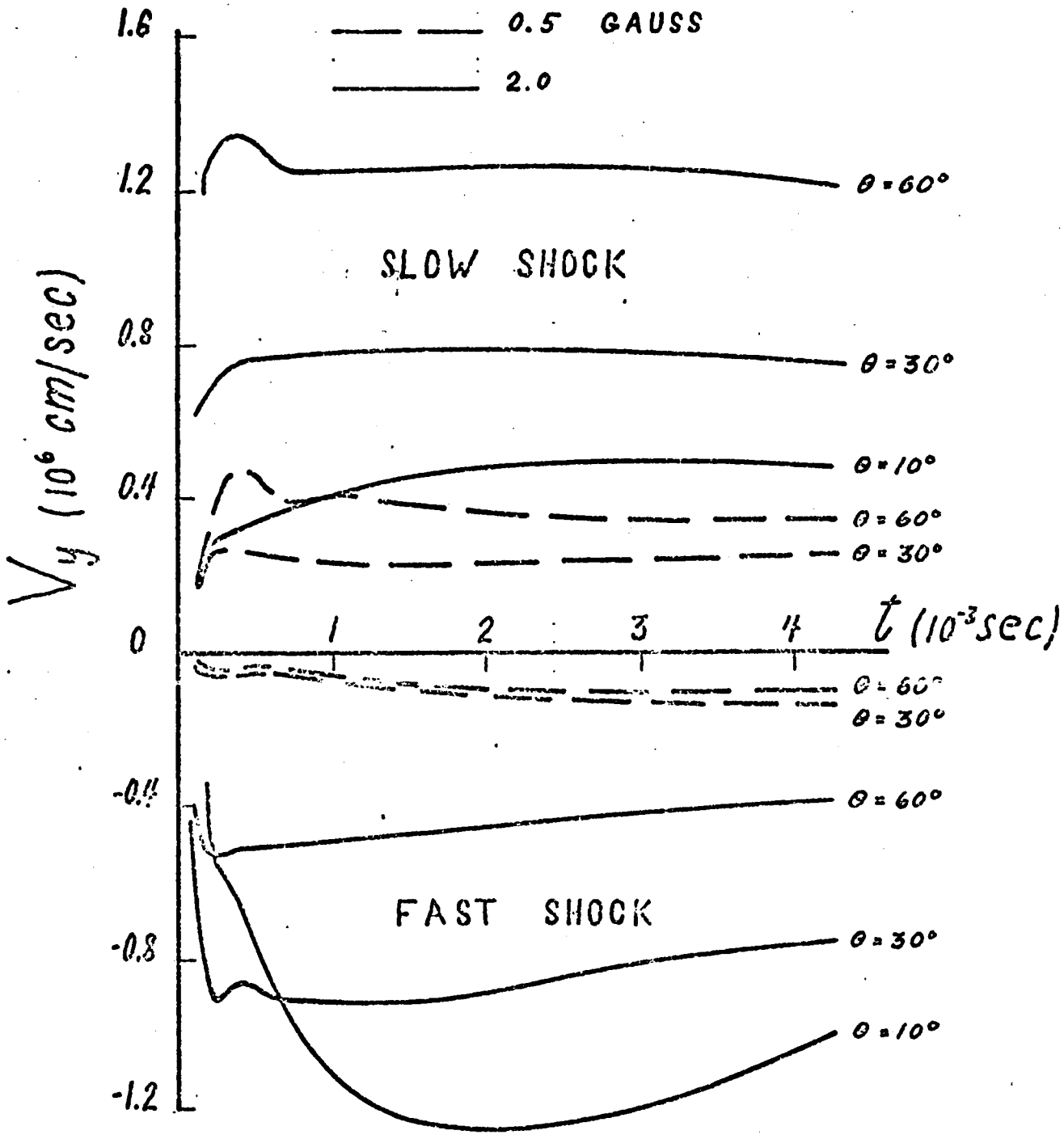

Fig. 5.9 Tangential velocity at shocks vs. time for planar blast waves

5.2 Spherical MHD Blast Waves

The expansion of a uniform highly heated sphere or fireball into the ambient MHD medium is studied using MHD CYCLONE for uniform magnetic fields of 0.5, 1.0 and 2.0 gauss alligned in the positive z direction ($\theta = 0$) as it was in Figure 4.2. In order to avoid numerical calculations directly at the center of the sphere, the fireball interface initially was located at a radius of 600 cm and a rigid stationary boundary placed at a radius of 100 cm, in this way approximating the expansion of a sphere of initial radius 500 cm. Numerical results were obtained for times up to approximately 1.0×10^{-3} sec. Because of the excessively long computer times involved, no attempt was made to obtain results at the larger times (4.25×10^{-3} sec.) presented for the planar blast wave model. Instead, the spherical and planar results are compared to give some qualitative idea of the spherical solution at large times.

For 0.5 gauss, the effects of the magnetic field on the spherical gasdynamic expansion are quite small; an increase in shock velocity, decrease in shock density and pressure, and a decrease in interface velocity, all near the equator. In addition, a very weak slow wave is present. Again, a secondary shock wave propagates inward, reflects at the center, and propagates outward as a bump on the profiles. The results for no magnetic field agree well with the solution of Chou and Huang[23], which applies only until the secondary shock implodes upon the origin.

The results for a magnetic field of 1.0 gauss show stronger slow wave effects. Figure 5.10 gives profiles of tangential magnetic field, B_θ, and tangential velocity, v_θ, at a time $t = 1.015 \times 10^{-3}$ sec.; as before, I denotes the position of the interface (contact surface). A discontinuity in B_θ is located at the contact surface for $\theta = 90^\circ$. For smaller θ, this discontinuity has propagated outward away from the interface at the slow wave speed. This is especially noticeable near the pole where the slow wave speed is large. Note that the peak negative value of v_θ coincides with the base of the discontinuity in B_θ. No jump in density or pressure is visible at the slow wave front.

At the main shock wave, v_θ increases as θ decreases, reaching a maximum at $\theta = 15^\circ$ and decreasing to zero at the pole. The large positive tangential velocity at the main shock and the equally as large negative v_θ behind it indicate a mass motion toward the equator confined to the region near the shock wave and a mass motion toward the pole over the rest of the disturbed region. The results agree very well with the planar blast wave results of Figure 5.3 for small magnetic fields, noting the difference in sign of the tangential velocity due to the difference in sign of the tangential magnetic field. As was true for the planar model, the secondary shock wave reflecting from the center of the sphere is greatly damped on passing through the slow wave. In fact, this secondary shock can only be seen clearly on a plot of radial velocity versus radial distance.

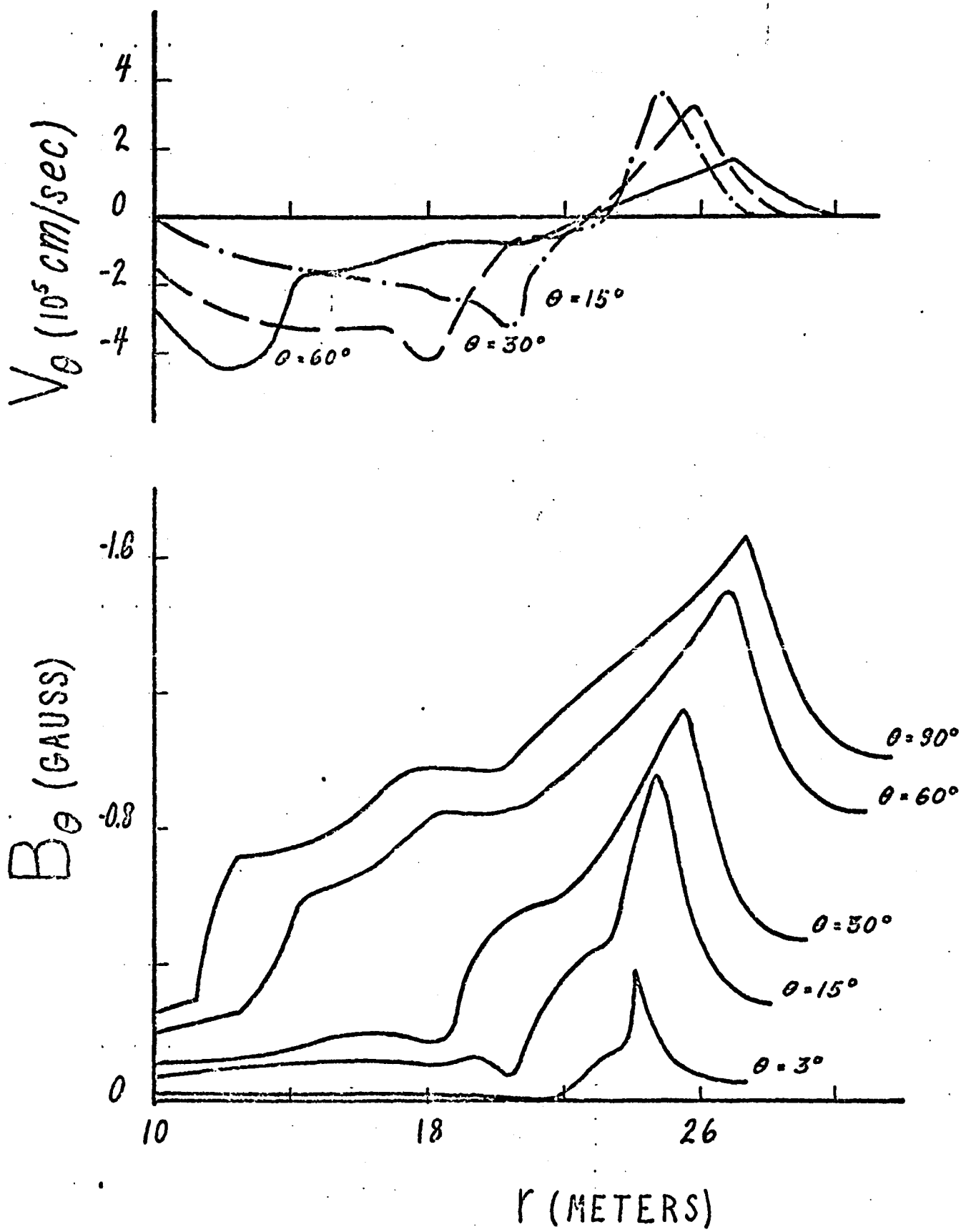

Fig. 5.10 Tangential magnetic field and velocity profiles ($B_o = 1.0$ gauss, $t = 1.015 \times 10^{-3}$ sec) for spherical blast waves

For 2.0 gauss, the large tangential motions are amplified. The magnetic field acts to sweep up particles near the pole and transport them toward the equator in such numbers that the density behind the main fast shock is reduced to less than the ambient density. Figure 5.11 shows density profiles at angles of 3, 15, and 30 degrees to the pole, at a time $t = 1.0 \times 10^{-3}$ sec. For $\theta = 3^{o}$, the fast shock has a negligible density jump and is almost entirely magnetic in character. Behind it, a rarefaction wave is barely visible. This rarefaction wave, also present near the pole for the spherical piston problem (Figures 4.6 and 4.12), becomes increasingly stronger for larger times; at $t = 1.624 \times 10^{-3}$ sec., the minimum density in this wave is 0.90×10^{-13} gms/cm^3.

Behind the rarefaction wave is a slow shock of large gasdynamic strength, with large discontinuities in tangential magnetic field and tangential velocity. This slow shock wave decreases in speed and in strength for larger θ until, for θ greater than 45^{o}, it has negligible gasdynamic strength. At the same time, the density and pressure jumps at the fast shock become larger as θ increases. The secondary reflected shock wave is no longer visible. While the split into two shocks is qualitatively predicted by the planar solution, the planar solution at the pole (a gasdynamic shock) is entirely different.

The shape of the fireball itself is of great interest and has been studied by Kruskal, Bernstein and Kulsrud[24] for the case when the fireball does not deviate strongly from a spherical shape. Figure 5.12 shows the

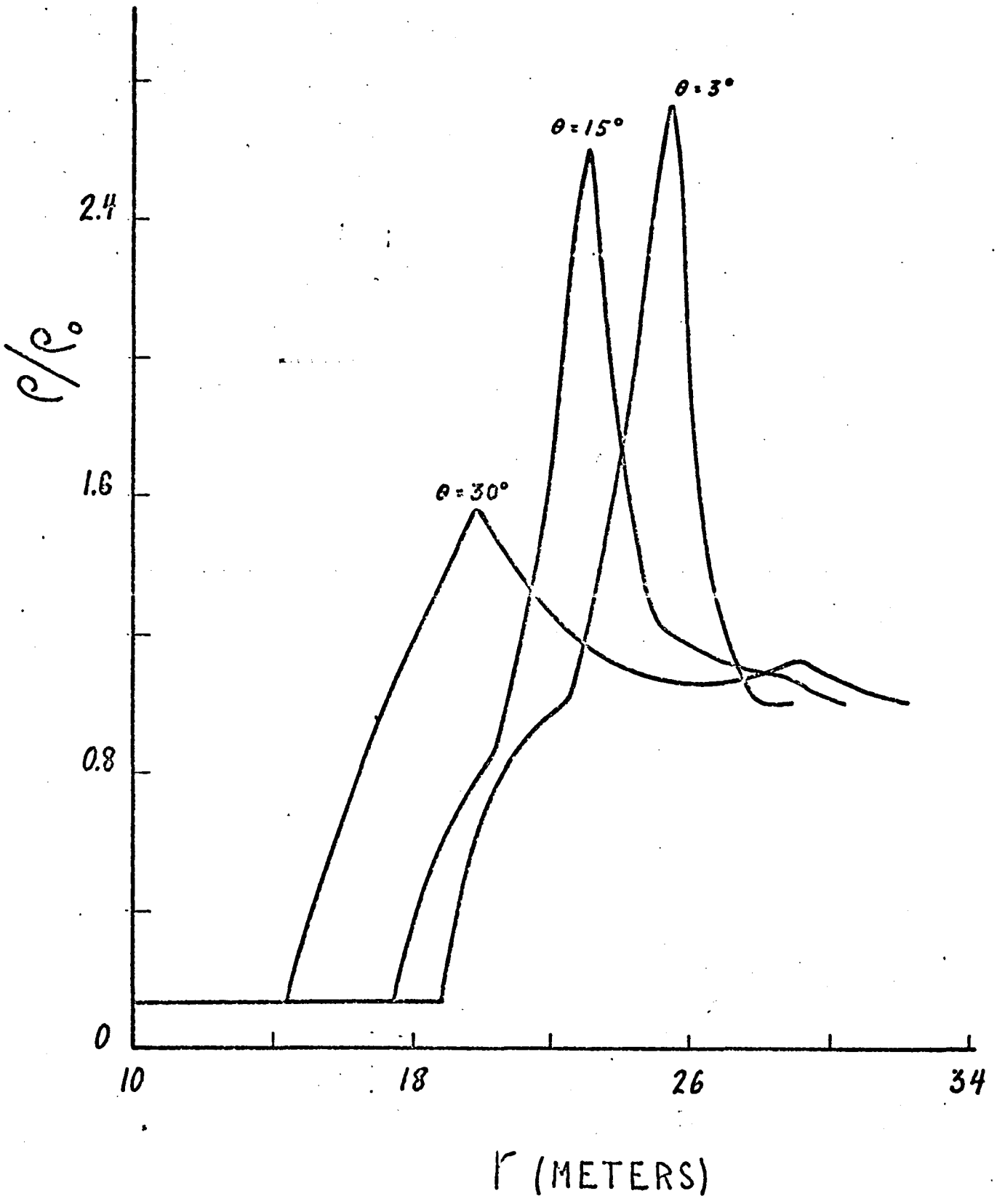

Fig. 5.11 Density vs. radius (B_o = 2.0 gauss, t = 1.0 x 10^{-3} sec) for spherical blast waves

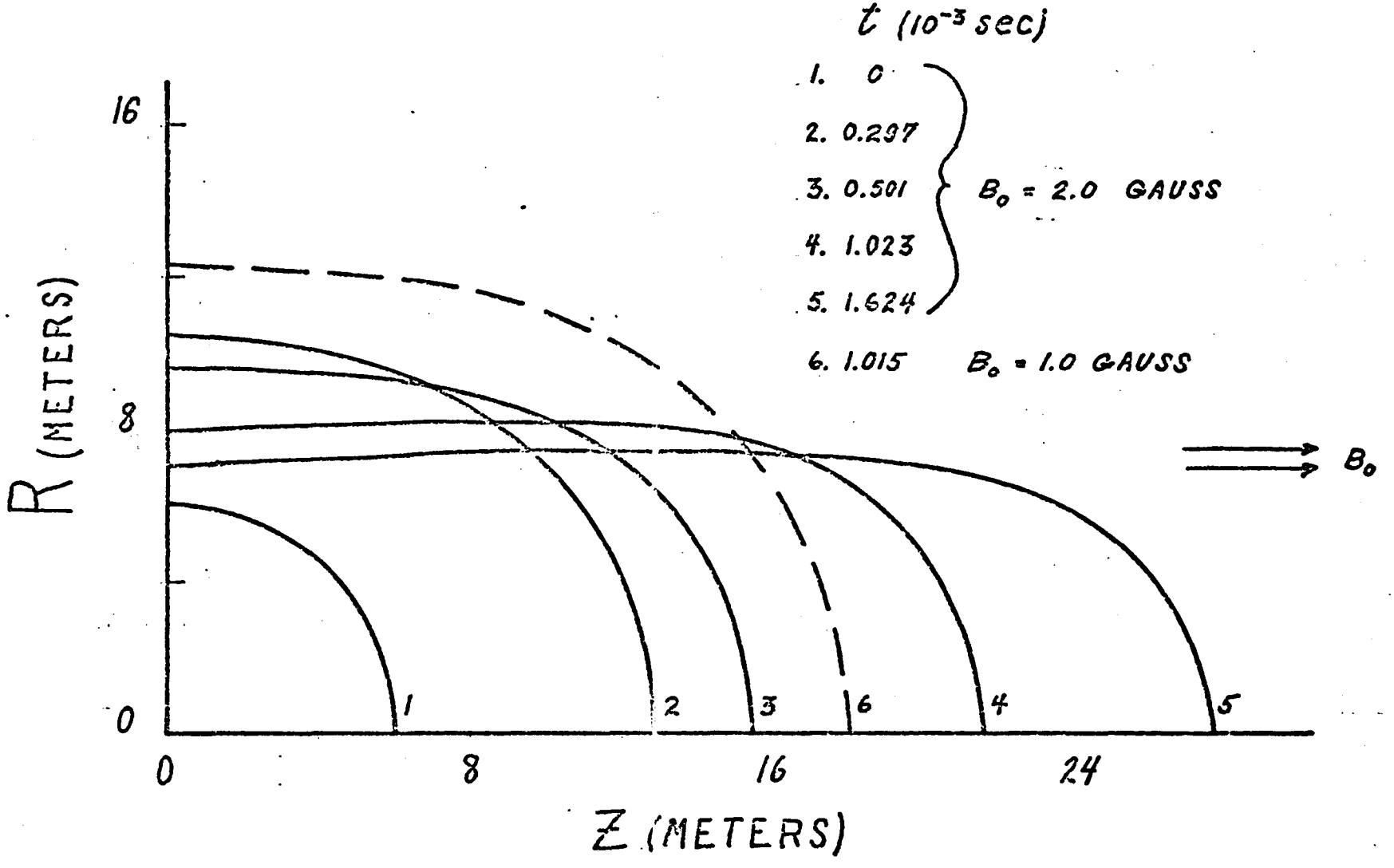

Fig. 5.12 Shape of fireball interface at different times for spherical blast waves

actual shape of the fireball interface at different times computed using MHD CYCLONE for a magnetic field of 2.0 gauss. The interface does deviate greatly from spherical and is an ellipse with major axis at the pole, its eccentricity increasing with time. Curves 4 and 6 show the fireball at approximately the same time for 2.0 gauss and 1.0 gauss respectively, and indicate the effect of the magnetic field upon the interface; that is, to slow down the interface at the equator and speed it up at the pole. The large mass motion toward the pole which occurs behind the slow shock results in an almost uniform density distribution inside the fireball in spite of its large eccentricity.

Figure 5.13 gives the radial interface position versus time for the range of magnetic fields. It is clear that for 1.0 gauss, the interface is slowed down and eventually stopped near the equator by the adverse magnetic pressure gradient, while for 2.0 gauss, the interface is seen to begin to collapse. For larger times, the interface position levels off to approximately 700 cm. as seen in Figure 5.12. Near the pole, the interface moves faster than it did for gasdynamics, the speed increasing with magnetic field. These general trends agree with the predictions of the planar blast solutions, Figure 5.6, but the planar results do not show the collapse of the fireball, which is a two-dimensional effect due to the mass motion away from the equator.

A study was made of the variables at the main shock wave similar to the studies made for the piston model and the planar blast model.

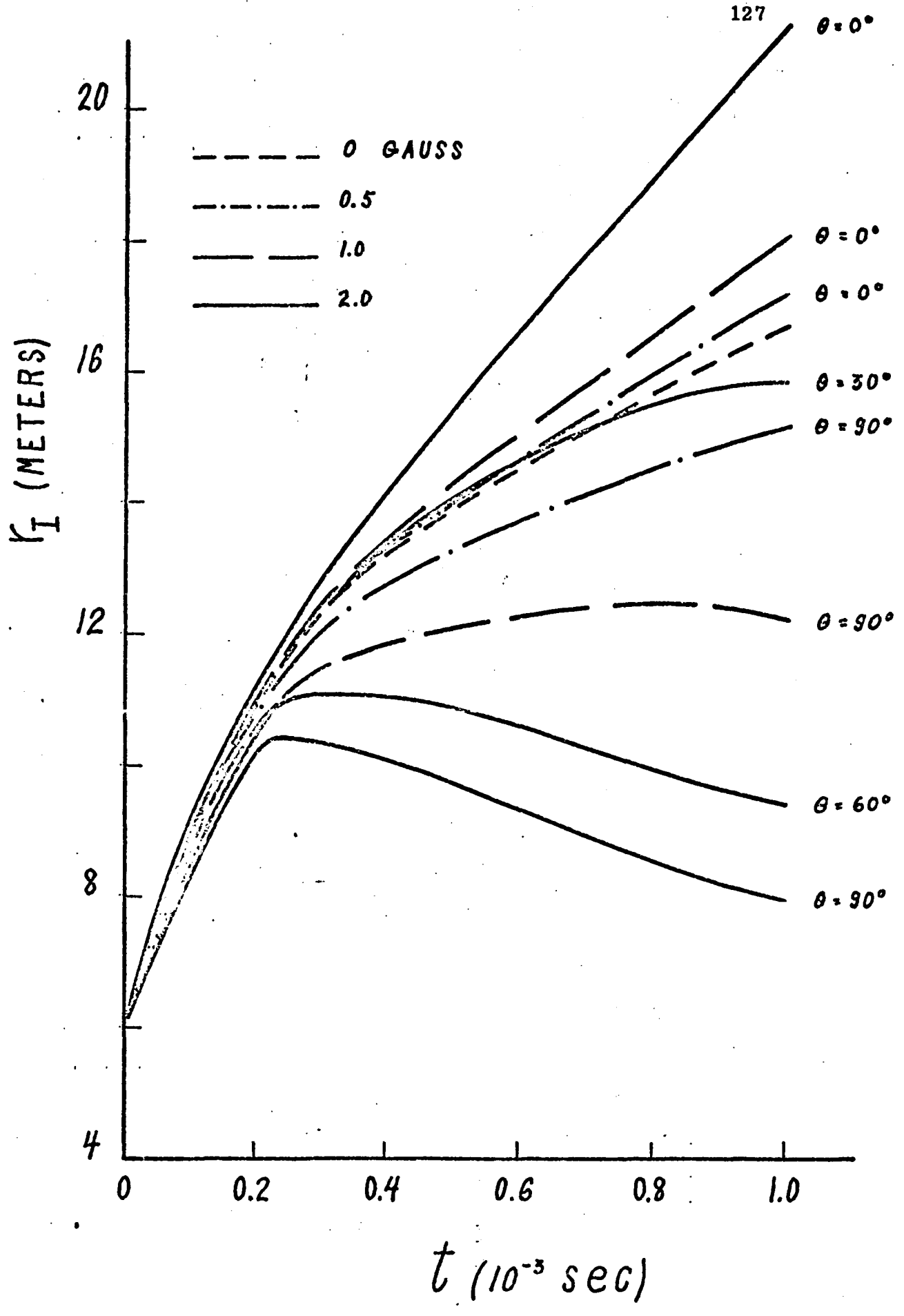

Fig. 5.13 Position of fireball interface vs. time for spherical blast waves

Figure 5.14 gives the radial position of the main shock versus time for the magnetic fields studied. For 0.5 gauss, not shown, the shock speed (the slope of the curve) at the equator increases from the gasdynamic value but shows a small decrease at the pole. For 1.0 gauss, the shock is far more elliptic and a greater reduction at the pole is visible. This reduction is due to the curvature of the magnetic field lines behind the shock causing an inward directed magnetic force which reduces the total force pushing out the shock. At the equator, shock speed increases with magnetic field due to the increased magnetic pressure.

For 2.0 gauss, gasdynamic jumps at the shock are negligible at the pole so that the shock propagates at the fast wave speed of the ambient medium which is the Alfven speed. For large times, the shock has propagated out further at the pole for this magnetic field than for the gasdynamic case. The spherical piston solution, in particular Figure 4.12, shows the same decrease in shock speed at the pole as magnetic field is increased until the gasdynamic strength becomes negligible, and the subsequent increase in shock speed.

The density at the main shock wave is presented in Figure 5.15 as a ratio to the ambient density. For both 0.5 and 1.0 gauss, at a given time, shock density increases toward the pole. This density variation is also present for 2.0 gauss, at small times. For the larger times shown, however, the relatively small shock density increases with θ. This change in variation with θ was also seen for the planar blast wave

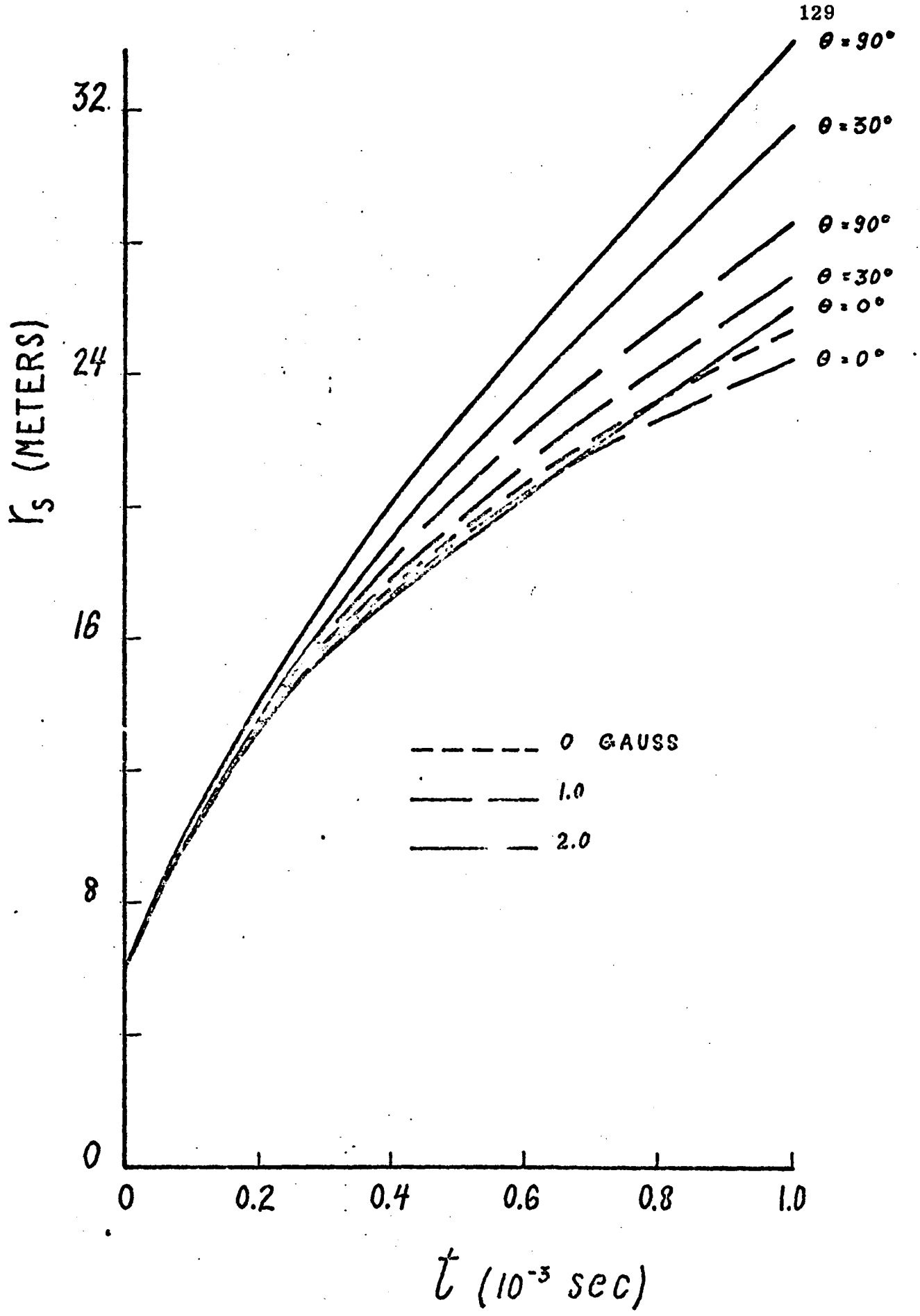

Fig. 5.14 Shock position vs. time for spherical blast waves

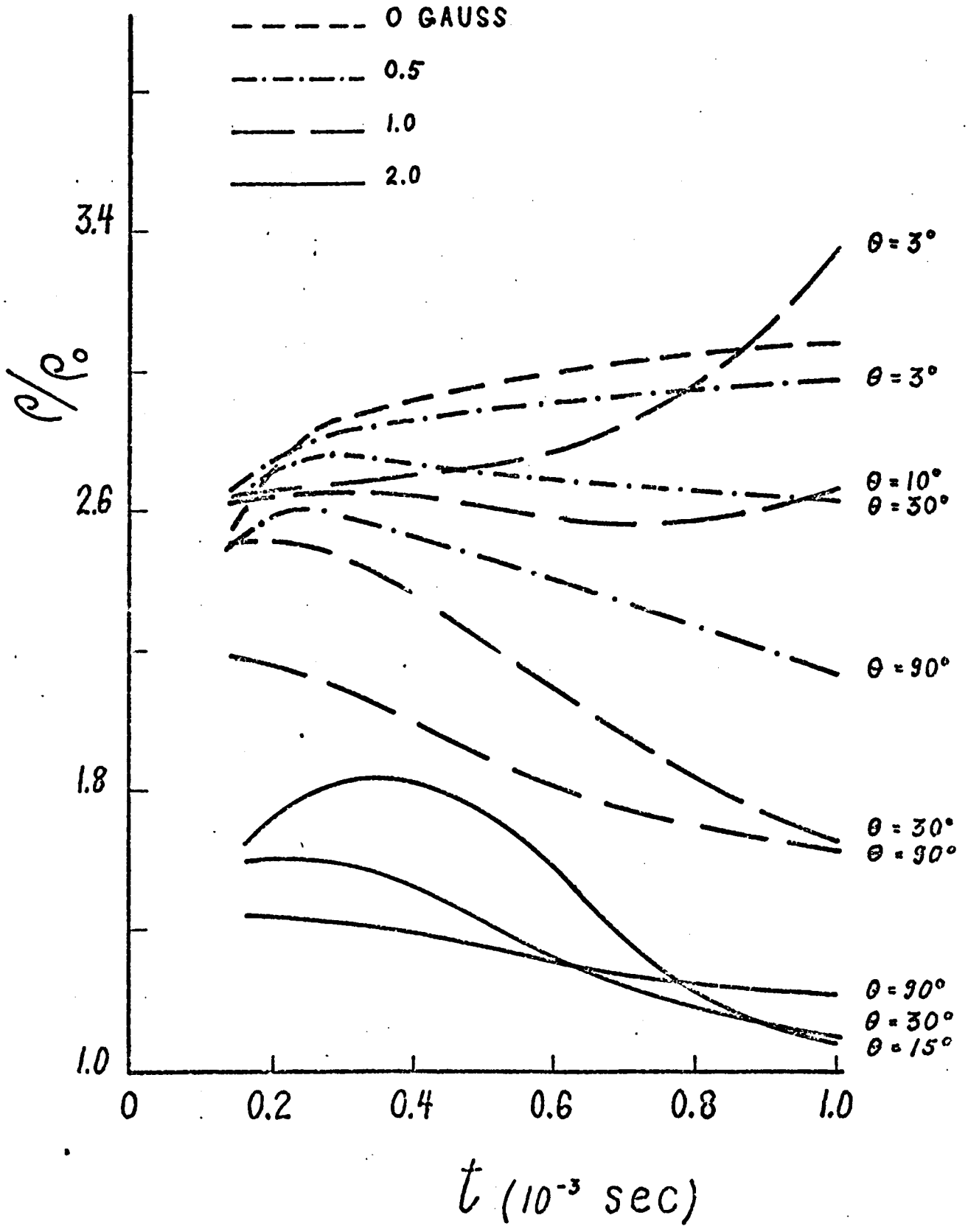

Fig. 5.15 Shock density vs. time for spherical blast waves

solution and for the piston solutions. It is due to the Alfven speed behind the shock becoming greater than the sound speed so that the strong gas-dynamic effects travel with the slow rather than the fast shock. In general, shock density decreases as magnetic field is increased due to the widening out of the disturbed region. Where the shock is slowed down ($\theta = 3^{o}$ for 1.0 gauss), the density increases greatly.

For purposes of comparison with the piston model, a shock strength parameter f_m, defined again as the ratio of the tangential magnetic field at the shock to the ambient value, is shown in Figure 5.16. As in the piston solution and the planar blast solution, it is found here that, for a given time, shock speed varies inversely as f_m, and that density varies directly as f_m where gasdynamic effects are large. This is true both for the variation with θ and for the variation with applied magnetic field. Gasdynamic pressure varies in the same manner as density and radial particle velocity at the shock shows this same pattern.

All the solutions discussed were for the expansion of a sphere with initial pressure and internal energy 10^4 times the ambient atmospheric values. Results were also obtained for a sphere an order of magnitude weaker for a uniform magnetic field of 0.5 gauss. A far weaker and slower shock wave propagates outward (shock and interface positions at 1.0×10^{-3} sec. are over 30 percent closer to the origin). The small magnetic field of 0.5 gauss has a very large effect on this weaker expansion. Since the sound speed is much smaller, the Alfven

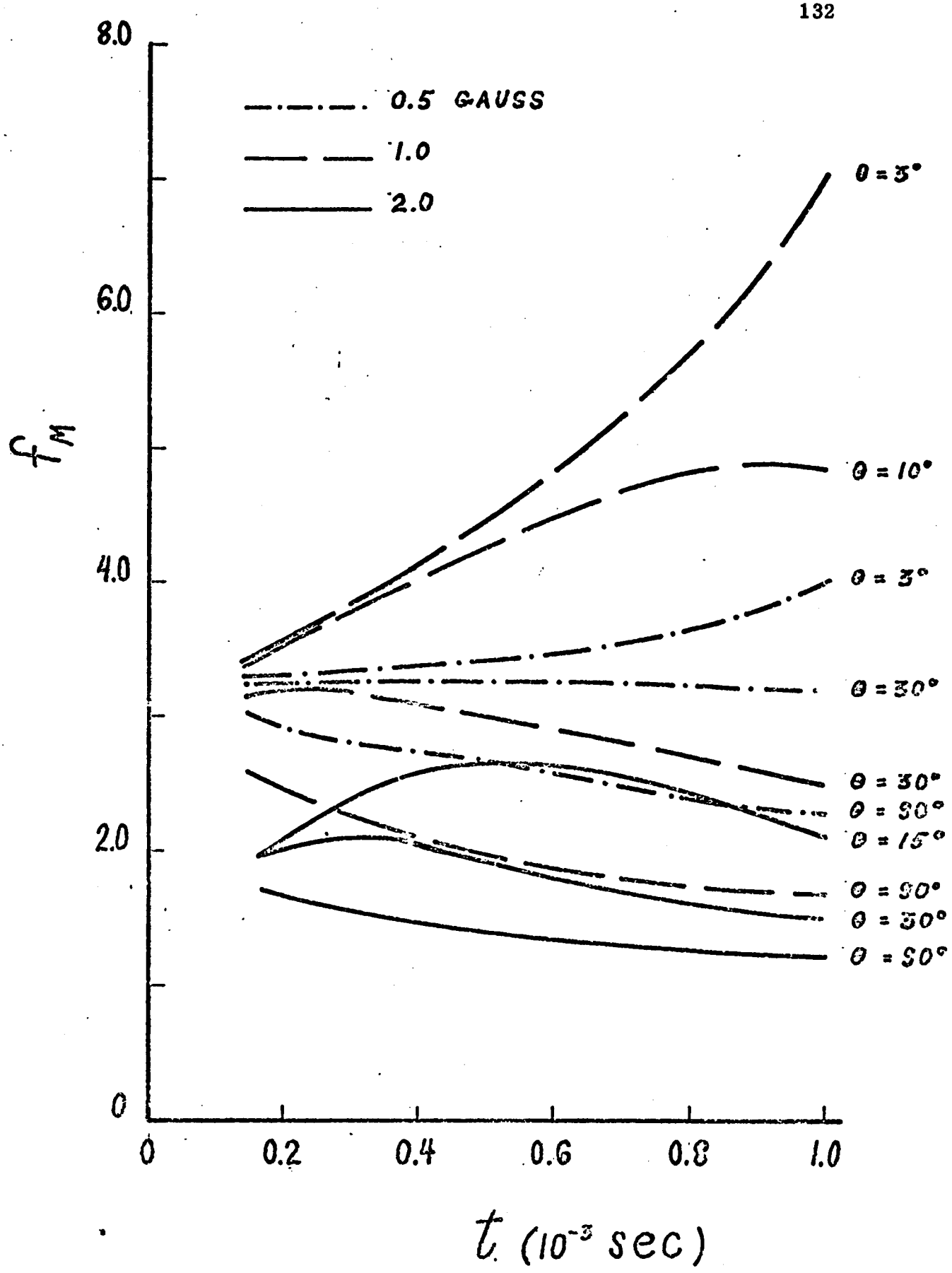

Fig. 5.16 Shock strength ($f_m = B_{\theta_s}/B_{\theta_o}$) vs. time for spherical blast waves

speed becomes larger than it, creating most of the phenomena visible only for larger fields for the stronger expansion. At the equator, the interface shows signs of collapse, while near the pole, two shocks are present as well as the rarefaction wave behind a front shock of negligible gasdynamic strength for $\theta = 3^{o}$.

In all computer runs, the total mass and energy of the system were conserved to within .01 percent. Since v_{θ} is very large and in fact changes sign, the rezoning in the θ direction is even more necessary here than for piston problems. This is especially true near the interface where, initially, a discontinuity develops.

5.3 Summary

In this chapter, solutions to the MHD blast wave problem including the effects of a magnetic field were obtained for the first time for both the planar and spherical cases. The planar solutions are useful in qualitatively predicting many of the phenomena encountered in the spherical problem. These are the elliptic main shock with major axis along the equator, the elliptic fireball interface with major axis at the pole, and the presence of an additional slow shock near the pole for large magnetic fields. Moreover, results may be obtained for planar blast waves at large times without the expenditure of enormous amounts of computer time; in fact the results are presented for planar blast waves at times a multiple of four the time for the spherical results.

A mass motion away from the pole behind the main shock and a reverse motion toward the pole behind the slow wave or shock are predicted by the planar solution. However, the results of these mass motions can be only seen using the spherical model. For large magnetic fields, the fireball interface near the equator begins to collapse, i.e., to travel back toward the origin. Additionally a rarefaction wave appears behind the main shock near the pole. Due to these opposite mass motions, the need for rezoning was even greater than for the spherical piston problem as the calculation could not have been carried out without it.

CHAPTER 6

DISCUSSIONS AND CONCLUSIONS

The primary result of this dissertation was the development of a computer code general enough to solve any three-dimensional axi-symmetric unsteady flow problem in a nondissipative MHD medium. This computer program was applied to the study of the expansion of a sphere of plasma into an MHD medium including a uniform magnetic field. Two mathematical models were studied; a rigid spherical piston expanding at a constant speed, and an initially high energy, high pressure sphere (fireball) allowed to expand gasdynamically (the blast wave model). The major emphasis was on determining the effects of a magnetic field upon the expansion. In this chapter, the numerical method is discussed. The results of the two mathematical models are compared, and the conclusions of the dissertation are summarized.

6.1 The Numerical Method

A numerical method developed to study nonlinear MHD problems in a nondissipative medium must provide some dissipative mechanism at shock waves to allow the fluid particles to gain entropy while crossing these discontinuities[3]; otherwise the calculations will be in error. The alternate procedure is to consider the shock wave to be a boundary in the flow and apply boundary conditions (the Rankine-Hugoniot shock conditions[26,27]) which relate flow variables on opposite sides of the discontinuity. The method of characteristics uses this approach to handle shock waves[2]. However, it is necessary to know in advance the number and position of the shock waves in order to apply this procedure. This information is generally not available, thus limiting the applicability of the method of characteristics.

Most numerical methods attempt to solve the differential equations in Eulerian coordinates. It is more advantageous to rewrite these equations in Lagrangian form since this both increases the accuracy of the difference scheme[3] and simplifies the calculation at any physical boundaries in the flow. Additionally, since Lagrangian coordinates follow the motion of each mass of fluid, the location of fluid boundaries, such as the interface of the fireball (a contact surface) is obtained quite easily at any time.

The use of Lagrangian coordinates, however, can result in considerable distortion of the finite difference scheme due to large mass

motions of the fluid. These distortions can cause large numerical errors which may swamp the calculation[8]. To avoid these errors, a rezoning scheme was introduced which continually restored the Lagrangian zones to a regular shape before distortions became significant. This rezoning scheme greatly increased the time step of the calculation so that results could be obtained at far larger times with the expenditure of less computer time.

The numerical method used here was an extension of the von Neumann-Richtmeyer method of artificial viscosity developed for gasdynamics. This method, which uses Lagrangian coordinates, introduces an artificial viscous stress term to the equation of motion, proportional to the square of velocity gradients, rather than the true viscous stress term which is proportional to the velocity gradient itself. The result is equivalent to using a large coefficient of viscosity for strong shocks (velocity gradients are large) and a small coefficient for weak shocks, thus obtaining a shock thickness of a few mesh widths, independent of the shock strength. Therefore, the equations may be solved without resorting to special handling of the shock waves. The shock thickness is controlled through a coefficient of artificial viscosity. Since the stress terms are quadratic in the rate of shear, these terms are almost negligible outside of the shock region, thus retaining the nondissipative character of the original equations.

To adapt this method to the MHD equations, it was found necessary to change the artificial stress term to include derivatives of the tangential velocity as well as the axial velocity. Otherwise large oscillations are present at the slow shock where tangential velocity gradients are large. Additionally the stability criteria were altered to account for both the presence of a magnetic field and the different form of the artificial viscosity. The most important addition of course was the rezoning scheme without which the calculation could not proceed.

Two different computer programs were developed, MHD WUNDY, specifically designed to solve one-dimensional problems in cartesian, cylindrical, or spherical geometries, and MHD CYCLONE, to solve three-dimensional axisymmetric problems for any specified geometry. To test out these programs, numerical solutions to planar one-dimensional piston problems were obtained and compared with theoretical solutions giving agreement to within one percent for both WUNDY and CYCLONE. In addition, spherical piston solutions for asymtotic cases were used to check out CYCLONE results. Results obtained for varying mesh sizes gave evidence of convergence and the solutions always appeared stable using the new stability criteria. Therefore it has been established that the numerical method works and that the new solutions obtained using this method are valid.

6.2 Piston Solutions

The piston model assumes a rigid piston, representing the interface between the plasma sphere and the initially ambient MHD medium, expanding at a constant speed into the ambient medium which may contain a uniform magnetic field. Since the piston is maintained at a constant speed, energy is continually added to the region ahead of it, thus giving a similarity solution, a solution which is identical for any time, except for an increase with time in the distance between the piston and the main shock wave propagating ahead of it at a greater constant speed. Solutions to this problem were obtained for both a planar and a spherical piston, specifically for the case when the speed of the piston is much greater than the speed of a sound wave in the ambient medium. For no magnetic field, this corresponds to a very strong shock wave where the pressure of the ambient gas is negligible in comparison to the pressure behind the shock.

The addition of a small uniform magnetic field noticeably weakened the shock wave, i.e. decreased density and pressure jumps, especially near the equator (the pole is the direction of the uniform magnetic field). It was noted that while the shock was sped up greatly at the equator due to a large magnetic pressure behind it, caused by the compression of field lines by the expanding piston, it was also slowed down at the pole due to an inward magnetic force caused by the curvature of field lines. As the uniform magnetic field was increased, the shock

was continually weakened and became more and more elliptic. Particles entering the shock were deflected away from the pole by the magnetic field and compressed continually as they approached the piston (the energy source). At the shock itself, density and pressure at the pole were approximately the same as for no magnetic field. These quantities were reduced wherever the shock was sped up, i.e. as angle θ from the pole was increased.

A sudden change in the above phenomena was observed when the uniform magnetic field was increased still further. The shock wave, which had a large density jump at the pole, now has negligible gas-dynamic strength there. The change occurs as the Alfven speed of the undisturbed medium is made greater than the constant piston speed (the piston becomes subalfvenic). At this critical magnetic field, the Alfven speed behind the shock wave was, for the first time, greater than the corresponding sound speed.

According to the Friedrichs diagram, Figure 1.1, at the pole the fast wave speed is either the sound speed (Figure 1.1a) or the Alfven speed (Figure 1.1b) depending upon the relative magnitudes of the sound and Alfven speeds. Since the gasdynamic effects may be considered to travel at the sound speed and the magnetic effects at the Alfven speed, the change in phenomena is due to the front shock becoming magnetic for the first time. Away from the pole, magnetic and gasdynamic effects are coupled for both cases. For superalfvenic pistons, this coupling results

in increasing magnetic effects as θ increases and therefore weaker density jumps, while for subalfvenic pistons, it results in increasing gasdynamic jumps as θ increases. For all magnetic fields, these jumps decrease as the uniform magnetic field is increased.

Since a shock of negligible gasdynamic strength travels at basically the Alfven speed of the undisturbed medium, the shock becomes less and less elliptic for the subalfvenic case, as magnetic field is increased. When the ambient Alfven speed is much greater than the piston speed, the shock is spherical. Behind the shock, a rarefaction wave is present near the pole for subalfvenic pistons. In this wave, the density becomes increasingly less than the ambient value as magnetic field is increased. This wave is due to the large mass motion of particles away from the pole caused by the magnetic forces. The rarefaction wave extends up to a boundary region of large pressure and density adjacent to the piston which denotes the front of a slow wave.

The spherical results were compared with numerical solutions to the planar one-dimensional piston problem. The planar solution correctly predicted the large mass motion away from the pole and the change in variation of shock density, etc., with angle from the pole as the piston becomes subalfvenic. In general however, the planar solution did not predict the spherical results well. In slab symmetry, the MHD equations are reducible thus giving a piston solution which consists of constant states separated by simple centered rarefaction waves or the

shock waves formed by the steepening of compressive simple waves. In spherical symmetry, the MHD equations are not reducible; therefore the solution between the shock and the piston is quite different from the planar solution. In particular, the planar solution predicts both a fast and slow shock, while the spherical solution gives only a fast shock.

The results presented were for a very strong gasdynamic shock wave (a very rarified medium). If the ambient medium is more dense, corresponding to the atmosphere at a lower altitude, the same magnetic field would have a much weaker effect since the material pressure would be greater. However, the basic results, giving the effects of a magnetic field on the piston problem, still apply qualitatively.

6.3 Blast Waves, Comparison with Piston Solutions

The blast wave model assumes a high pressure, high energy sphere of plasma (fireball) initially at the same density as the ambient MHD medium outside. The high energy and pressure are uniformly distributed inside the fireball giving a discontinuity in these variables at the interface of the sphere. Since the fireball is pushed out by the pressure discontinuity, compressing the plasma in front of it, a shock wave propagates ahead of the interface. The interface itself is a contact surface (plasma behind it is expanding, ahead is compressed). As the energy and pressure inside the fireball decay with time, the interface and eventually the shock wave are slowed down. The solution is therefore unsteady in time.

The piston model assigned a constant speed to the fireball interface thus adding an unending supply of energy to the region ahead of it, while for the blast wave, the energy added to this region decreases with time. Therefore the blast wave model is a more realistic approximation to physical problems such as supernova expansions or explosions in the atmosphere. This gain is however offset by the added mathematical difficulty of obtaining solutions to the unsteady problem.

A major difference between the piston and blast wave solutions, evident even for gasdynamics, is in the gradients of density, pressure, and radial velocity ahead of the interface. The maintaining of the constant piston velocity resulted in a large compression ahead of it and therefore

negative gradients in the above variables. For the blast wave, the reduction in speed of the interface allows the plasma ahead of it to expand with time, giving positive gradients in these variables behind the shock.

The addition of a magnetic field accentuates the differences between the two solutions. For the piston model, the fireball is constrained to remain spherical. For the blast wave model however, the spherical fireball was distorted into an elliptical shape by the magnetic field. Near the equator, the compression of magnetic field lines gave a large positive gradient of magnetic pressure similar to the density gradient (field lines are frozen into the fluid), which slowed down the fireball. For large magnetic fields (2.0 gauss for the given data), the interface motion was completely stopped and reversed near the equator by this magnetic field.

There were still some major points of agreement between the two solutions, primarily at the main (fast) shock wave. Both showed an elliptic main shock with major axis at the pole. At a given time, the blast wave solution showed qualitatively the same variation in shock quantities (density, pressure, and radial velocity) with angle θ from the pole. For small magnetic fields, these quantities decreased as θ increased while for large magnetic fields (at large times) they increased as θ increased. The change in variation was due to the Alfven speed becoming greater than the sound speed behind the shock and therefore the fast shock becoming primarily magnetic rather than gasdynamic in character.

At the pole, where the sound and Alfven effects are essentially uncoupled according to the Friedrichs diagram, the shock had negligible gasdynamic strength for large magnetic fields at large times. At small times, the large pressure inside the fireball maintains the sound speed greater than the Alfven speed so that the effects are similar to the small magnetic field results. It is evident that the effect of a magnetic field on the fast shock is basically independent of how the shock was formed and depends upon the ratio of the two small amplitude wave speeds alone.

Both models showed a large tangential motion behind the shock away from the pole. For large magnetic fields, this motion results in a rarefaction wave (a decrease in density) near the pole. An important difference between the two solutions involves the presence of a slow wave. For the piston model, the tangential velocity was always positive (directed away from the pole) and, due to the large speed of the piston, the slow wave was confined near its surface. For the blast wave, however, the presence of a contact surface at the interface resulted in a discontinuity in tangential velocity there. As the interface slowed down, this discontinuity propagated outward away from it at the slow wave speed giving a large negative tangential velocity and therefore a large tangential motion toward the pole. For large magnetic fields, where the fast shock was magnetic, the slow wave steepened into a slow shock having large gasdynamic strength near the pole. Planar blast wave solutions predicted this slow shock and the two tangential motions, away from the

pole behind the fast shock, and toward the pole behind the slow shock.

The significant differences between the two solutions imply that the piston model is only useful in the early stages of an explosion and only for small magnetic fields, but is more useful in the supernova problem[11] where the interface speed remains almost constant.

6.4 Summary

The conclusions of this dissertation are summarized as follows:

(1) Numerical solutions may be obtained to nonlinear three-dimensional axisymmetric unsteady nondissipative MHD problems using the existing computer technology at a reasonable cost in computer time.

(2) The von Neumann-Richtmeyer method of artificial viscosity may be applied to MHD problems only if great care is taken in restoring the Lagrangian zones to a regular shape in order to eliminate the distortions caused by the physical motion of the plasma.

(3) The effects of a magnetic field on the blast wave model are in general quite different from those on the piston model since the spherical fireball is slowed down and deformed into an elliptic shape.

APPENDIX

A. Solutions of the Planar MHD Shock Equations

For a nondissipative fluid, shock waves are described as discontinuities in the flow. Across these discontinuities, the generalized Rankine-Hugoniot shock equations apply. For a perfect gas, these equations are written as follows (c.g.s. gauss units) for a shock propagating in the x direction:

Conservation of mass

$$\rho_1 u_{x_1} = \rho_o u_{x_o} \tag{A1}$$

Conservation of normal momentum

$$\rho_1 u_{x_1}^2 + p_1 + \frac{B_{y_1}^2}{8\pi} = \rho_o u_{x_o}^2 + p_o + \frac{B_{y_o}^2}{8\pi} \tag{A2}$$

Conservation of tangential momentum

$$\rho_1 u_{x_1} u_{y_1} - \frac{B_x B_{y_1}}{4\pi} = \rho_o u_{x_o} u_{y_o} - \frac{B_x B_{y_o}}{4\pi} \tag{A3}$$

Conservation of energy

$$\rho u_{x_1}\left(\frac{u_{x_1}^2}{2} + \frac{\gamma}{\gamma-1}\frac{p_1}{\rho_1}\right) + u_{x_1}\frac{B_{y_1}^2}{4\pi} - \frac{B_x B_{y_1} u_{y_1}}{4\pi} = \rho_o u_{x_o}\left(\frac{u_{x_o}^2}{2} + \frac{\gamma}{\gamma-1}\frac{p_o}{\rho_o}\right)$$

$$+ u_{x_o}\frac{B_{y_o}^2}{4\pi} - \frac{B_x B_{y_o} u_{y_o}}{4\pi} \tag{A4}$$

Continuity of tangential electric field

$$u_{x_1} B_{y_1} - u_{y_1} B_x = u_{x_o} B_{y_o} - u_{y_o} B_x \qquad \text{(A5)}$$

where $\vec{u} = \vec{v} - U$ is the velocity relative to the shock, U is the shock speed and the subscripts o and 1 denote quantities in front and behind the shock respectively, (mass flows across the shock from the front to the back). Assuming that quantities ahead of the shock are known, this set of 5 equations contains 6 unknowns, ρ_1, p_1, u_{x_1}, u_{y_1}, B_{y_1}, and U, so that the solution must be in terms of an arbitrary parameter.

Bazer and Ericson have obtained solutions to these equations by algebraic manipulation in terms of the arbitrary parameter g, representing the jump in tangential magnetic field across the shock, positive for fast shocks and negative for slow shocks given by:

$$g = \frac{[B_y]}{|B_o|} \qquad \text{(A6)}$$

where $[Q] = Q_1 - Q_o$ represents the jump in a quantity across the shock.

The solution is presented here for the fast shock in a slightly different form. The slow shock solution is obtained by replacing g_f by g_s:

$$\frac{[\rho]}{\rho_o} = g_f \left[\frac{-\frac{\gamma}{2} g_f \sin\bar{\theta} - (1-s_o) \pm (\bar{r}(g_f))^{\frac{1}{2}}}{2 s_o \sin\bar{\theta} - (\gamma-1) g_f} \right] \tag{A7}$$

$$\frac{[p]}{p_o} = \frac{\gamma g_f}{s_o} \left[-\frac{g_f}{2} + \frac{\left(\frac{[\rho]}{\rho_o g_f} - \sin\bar{\theta}\right)}{\left(1 - \frac{[\rho]}{\rho_o g_f} \sin\bar{\theta}\right)} \right] \tag{A8}$$

$$\frac{u_{x_o}}{b_{x_o}} = \left(\frac{\rho_1}{\rho_o}\right)^{\frac{1}{2}} \left[1 - \frac{[\rho]}{\rho_o g_f} \sin\bar{\theta}\right]^{-\frac{1}{2}} \tag{A9}$$

$$u_{x_1} = u_{x_o} \frac{\rho_o}{\rho_1} \tag{A10}$$

$$\frac{[u_y]}{b_{x_o}} = \left(\frac{\rho_1}{\rho_o}\right)^{-\frac{1}{2}} \frac{g_f}{\cos\bar{\theta}} \left[1 - \frac{[\rho]}{\rho_o g_f} \sin\bar{\theta}\right]^{\frac{1}{2}} \tag{A11}$$

where

$$r(g_f) = g_f^2 \left[\frac{\gamma^2}{4} \sin^2\bar{\theta} - (\gamma-1)\right] + g_f \sin\bar{\theta}(2-\gamma)(1+s_o) + 4 s_o \sin^2\bar{\theta} + (1-s_o)^2 \tag{A12}$$

$$s_o = a_o^2 / b_o^2 \tag{A13}$$

and $\bar{\theta}$ is the angle the magnetic field ahead of the shock makes with the x axis.

B. The Shock Relations for the Gasdynamic Piston Problem

A piston propagates in the x direction into an ambient gasdynamic medium at a constant speed v_{xp} generating a shock propagating at a constant shock speed U. The region between the shock and the piston is a region of constant state with velocity v_{xp}, denoted by subscript 1. In the region ahead of the shock denoted by subscript o, p_o and ρ_o are known and the fluid velocity is zero, so that, relative to the shock, the velocity is the shock speed. The shock equations, (A1) - (A5), reduce to the following:

$$\rho_o U = \rho_1 (U - v_{xp}) \tag{B1}$$

$$\rho_o U^2 = \rho_1 (U - v_{xp})^2 + p_1 \tag{B2}$$

$$\frac{U^2}{2} + \frac{a_o^2}{\gamma - 1} = \frac{(U - v_{xp})^2}{2} + \frac{\gamma}{\gamma - 1} \frac{p_1}{\rho_1} \tag{B3}$$

where $a_o = (\gamma p_o / \rho_o)^{\frac{1}{2}}$ is the ambient sound speed.

These three equations are combined, eliminating all unknowns except for U, by solving (B2) for p_1 and substituting the result into (B3), eliminating ρ_1 by use of (B1), giving the resulting quadratic equation in U.

$$U^2 - v_{xp} \left(\frac{\gamma + 1}{2} \right) U - a_o^2 = 0 \tag{B4}$$

The only physical root of this equation is

$$\frac{U}{v_{xp}} = \frac{\gamma+1}{4} + \left[\left(\frac{\gamma+1}{4}\right)^2 + \frac{a_o^2}{v_{xp}^2}\right]^{\frac{1}{2}} \tag{B5}$$

Substituting (B5) into (B1) and (B2) gives the rest of the solution:

$$\frac{p_1}{p_o} = 1 + \frac{\gamma U}{a_o}\,\frac{v_{xp}}{a_o} \tag{B6}$$

$$\frac{\rho_1}{\rho_o} = \frac{U}{U - v_{xp}} \tag{B7}$$

These gasdynamic piston solutions (B5) - (B7), unlike the solutions of Appendix A, do not involve any arbitrary parameter. The solutions in the limiting case of a very strong shock ($v_{xp} \gg a_o$) are

$$\frac{U}{v_{xp}} \to \frac{\gamma+1}{2} \tag{B8}$$

$$\frac{p_1}{p_o} \to \infty \tag{B9}$$

$$\frac{\rho_1}{\rho_o} \to \frac{\gamma+1}{\gamma-1} \tag{B10}$$

The shock speed ratio given by (B8) approaches a minimum value, the pressure jump is infinite, while the density jump approaches a maximum finite value depending only upon γ, the ratio of the specific heats.

C. The Shock Relations for the MHD Piston Problem

A magnetic field at an arbitrary angle to the flow is added to the model of Appendix B. For sufficiently large values of $s_o = a_o^2/b_o^2$, the solution can be represented as a fast MHD shock followed by a large region of constant state in which the velocity is the piston velocity, followed by a very weak MHD wave near the piston necessary to satisfy the boundary condition, $v_{yp} = 0$. This type of solution has been generated by the computer for values of s_o as low as 0.6. The shock equations (A1) - (A5) reduce to the following system of 5 equations for 5 unknowns.

$$\rho_o U = \rho_1 (U - v_{xp}) \tag{C1}$$

$$\rho_o U^2 + p_o + \frac{B_{y_o}^2}{8\pi} = \rho_1 (U - v_{xp})^2 + p_1 + \frac{B_{y_1}^2}{8\pi} \tag{C2}$$

$$\rho_o U u_{y_1} = -\frac{B_x}{4\pi} (B_{y_1} - B_{y_o}) \tag{C3}$$

$$\frac{U^2}{2} + \frac{a_o^2}{\gamma-1} + \frac{B_{y_o}^2}{4\pi\rho_o} = \frac{(U - v_{xp})^2}{2} + \frac{u_{y_1}^2}{2} + \frac{\gamma}{\gamma-1}\frac{p_1}{\rho_1} + \frac{B_{y_o}}{4\pi\rho_o} B_{y_1} \tag{C4}$$

$$U B_{y_o} = (U - v_{xp}) B_{y_1} + u_{y_1} B_x \tag{C5}$$

A solution similar to Appendix B was attempted, resulting in a complicated higher order equation in U, (a cubic for $B_x = 0$). Rather

than attempting to solve this equation, a shock parameter $f = \rho_1/\rho_o$ is defined and all other unknowns are determined as functions of f. Equation (C1) can be solved immediately for the shock speed giving

$$\frac{U}{v_{xp}} = \frac{f}{f-1} \tag{C6}$$

Equations (C3) and (C5) can now be combined to eliminate u_{y_1}. Using (C6), the solution for B_{y_1} is obtained.

$$\frac{B_{y_1}}{B_{y_o}} = 1 + \frac{(f-1)}{1 + \frac{(f-1)^2}{f}\frac{b_{y_o}^2}{v_{xp}^2}} \tag{C7}$$

Substituting (C7) into (C3) and solving for u_{y_1} gives the following:

$$\frac{u_{y_1}}{b_{x_o}} = -\frac{b_{y_o}}{v_{xp}}\frac{(f-1)}{f}\left(\frac{B_{y_1}}{B_{y_o}} - 1\right) \tag{C8}$$

The pressure ratio is obtained from either (C2) or (C4), giving respectively

$$\frac{p_1}{p_o} = 1 + \frac{\gamma}{a_o^2}\left[v_{xp}^2\frac{f}{f-1} - b_{y_o}^2\left(\left(\frac{B_{y_1}}{B_{y_o}}\right)^2 - 1\right)\right. \tag{C9}$$

$$p_1/p_o = f\left\{1 + \frac{\gamma-1}{a_o^2}\left[\frac{v_{xp}^2}{2}\frac{f+1}{f-1} - b_{y_o}^2\left(\frac{B_{y_1}}{B_{y_o}} - 1\right) - \frac{u_{y_1}^2}{2}\right]\right\} \tag{C10}$$

Since the shock equations (C1) - (C5) are consistent, and one of the unknowns, ρ_1, was used as a parameter, the pressure ratios given by (C9) and (C10) will be identical only for the correct value of ρ_1. The complete solution is obtained from (C6) - (C10) most simply by iteration, starting from a value of f given by the strong shock relation (B10), and decreasing f until (C9) and (C10) give the same result. If we already have a solution, for example from a computer program, the results can be checked by using the value of f given by the computer to solve (C6) - (C10), noting that (C9) and (C10) must give the same result.

For the special case of a perpendicular shock ($B_x = 0$), the shock speed is still given by equation (C6), (C7) reduces simply to $B_{y_1}/B_{y_o} = f$, and (C8) gives $u_{y_1} = 0$. Equations (C9) and (C10) reduce to the following:

$$\frac{p_1}{p_o} = 1 + \frac{\gamma}{a_o^2}\left[v_{xp}^2 \frac{f}{f-1} - \frac{b_{y_o}^2}{2}(f^2-1)\right] \qquad (C11)$$

$$\frac{p_1}{p_o} = \left\{1 + \frac{\gamma-1}{a_o^2}\left[\frac{v_{xp}^2}{2}\frac{f+1}{f-1} - b_{y_o}^2 (f-1)\right]\right\} \qquad (C12)$$

Equations (C11) and (C12) may be combined giving a cubic equation in f which can be solved directly for ρ_1, thus eliminating any iteration. For B = 0, the two equations combine into a quadratic in f, reducing to the solution of Appendix B.

REFERENCES

1 J. von Neumann and R. D. Richtmeyer, J. Appl. Phys. 21, 232 (1950).

2 L. Fox, Numerical Solution of Ordinary and Partial Differential Equations (Addison-Wesley, Reading, Mass., 1962).

3 R. D. Richtmeyer and K. W. Morton, Difference Methods in Initial-Value Problems (Interscience Publishers, New York 2nd Ed., 1967).

4 T. Orlow, D. Piacesi, and H. M. Sternberg, Naval Weapons Lab. Rept. NAVWEPS 7265 (1960).

5 D. Lehto and M. Lutzky, Naval Ordnance Lab. Tech. Rept. NOLTR 62-168 (1965).

6 N. C. Jen, M. Lutzky, and D. Piacesi, Naval Ordnance Lab. Tech. Rept. NOLTR 67-193 (1968).

7 K. O. Friedrichs, Los Alamos Rept. LAMS 2105 (1954).

8 B. Alder, S. Fernbach, and M. Rotenberg, Methods in Computational Physics, Advances in Research and Applications, Vol. 3, Fundamental Methods in Hydrodynamics (Academic Press, New York, 1964).

9 L. C. Higbie and M. N. Plooster, J. Comp. Phys. 3, 154 (1968).

10 G. I. Taylor, Proc. R. Soc. London A 186, 273 (1946).

11 R. M. Kulsrud, I. B. Bernstein, M. Kruskal, J. Fanucci, and N. Ness, Astrophys. J. 142, 491 (1965).

12 I. B. Bernstein and R. M. Kulsrud, Astrophys. J. 142, 479 (1965).

13 J. Bazer, Astrophys. J. 128, 686 (1958).

14 A. I. Akhiezer, G. Ya. Liubarski, and R. V. Polovin, Sov. Phys. JETP 8, 507 (1959).

15 A. I. Akhiezer and R. V. Polovin, Sov. Phys. JETP 11, 383 (1960).

16 V. V. Gogosov and A. A. Barmin, Sov. Phys. Doklady 134, 1041 (1960).

17 A. Jeffrey and T. Taniuti, Non-Linear Wave Propagation (Academic Press, New York, 1964).

18 C. K. Chu and R. Taussig, Phys. Fluids 10, 249 (1967).

19 C. K. Chu and R. A. Gross, Columbia Univ. Rept. No.41 (1968).

20 G. I. Taylor, Proc. R. Soc. London A 201, 159 (1950).

21 S. I. Sedov, Similarity and Dimensional Methods in Mechanics (Academic Press, New York, 1959).

22 H. L. Brode, J. Appl. Phys. 26, 766 (1955).

23 P. C. Chou and S.L. Huang, J. Appl. Phys. 40, 752 (1969).

24 M. D. Kruskal, I. B. Bernstein, and R. M. Kulsrud, Astrophys. J. 142, 369 (1965).

25 A. Jeffrey, Magnetohydrodynamics (Interscience Publishers, New York, 1966).

26 W. Rankine, Phil. Trans. A 160, 277 (1860).

27 H. Hugoniot, J. Ec. Polyt. Paris 57, 3, 58, 1 (1887).

28 F. De Hoffman and E. Teller, Phys. Rev. 80, 692 (1950).

29 J. Bazer and W. P. Ericson, Astrophys. J. 129, 758 (1959).

30 R. Courant and K. O. Friedrichs, Supersonic Flow and Shock Waves (Interscience Publishers, New York, 1948).

31 G. W. Sutton and A. Sherman, Engineering Magnetohydrodynamics (McGraw-Hill, New York, 1965).

32 Shih I. Pai, Magnetogasdynamics and Plasma Dynamics (Prentice-Hall, New York, 1962).

33 E. Johnson, Environment Handbook.

34 L. Spitzer, Physics of Fully Ionized Gases (Wiley and Sons, New York, 1965).

35 R. Courant and D. Hilbert, Methods of Mathematical Physics Vol. II (Interscience Publishers, New York, 1962).

36 B. Becker, Z. Physik 21, 321 (1922).

VITA

Norton Rimer was born in New York City on December 15, 1943.

Mr. Rimer attended elementary school in the Bronx and graduated from W. H. Taft High School in June 1959. He entered The City College in September, 1959. At City College, Mr. Rimer majored in civil engineering and was a member of ASCE. In January of 1964, he received the degree of Bachelor of Engineering (Civil).

In February, 1964, Mr. Rimer entered the Graduate School of Engineering of the City University of New York as a full-time student. He received the degree of Master of Engineering (Civil) in June, 1965. Mr. Rimer passed his Language Exam in Russian on May 11, 1966, his First Exam on September 19, 1966, and Second Exam on May 2, 1968. He was admitted to the Ph.D. Candidacy on September 1, 1968. Since 1968, he has remained at The City College, working as a research assistant and/or Lecturer in the Department of Civil Engineering where he completed his dissertation in early 1972.